# Enhanced Strength and Frictional Properties of Copper-Graphene-Copper Nanolaminates

Shruti Rastogi

Submitted in partial fulfillment of the
requirements for the degree of
Doctor of Philosophy
under the Executive Committee
of the Graduate School of Arts and Sciences

COLUMBIA UNIVERSITY

2021

# Abstract

Enhanced Strength and Frictional Properties of Copper-Graphene-Copper Nanolaminates

Shruti Rastogi

Understanding the deformation mechanism in nanocomposites is critical to realizing a host of next-generation technologies like stretchable electronics, three-dimensional multifunctional surfaces, and nanoscale machines. Graphene's unparalleled mechanical strength and stability – owing to its two-dimensional geometry, high intrinsic strength, and Young's modulus – have opened up new opportunities to engineer composites of higher strength-to-weight ratios for various practical applications. The ability of graphene (Gr) to act as a strength enhancer depends on the interface interactions and the composite's microstructure. Here we demonstrate a microstructure design of Cu-Gr-Cu nanolaminate that enhances the composite's load-bearing capacity, improves the composite's strength, and reduces its coefficient of friction.

The mechanical and frictional properties of Cu-Gr-Cu nanolaminate were probed using the nanoindenter. A series of nanoindentations performed on Cu-Gr-Cu nanolaminate exhibit an effective yield strength of 322.8 MPa and effective flow strength of 0.5 GPa. Scratch tests performed on the free surface of the Cu-Gr-Cu nanolaminate show a considerable decrease in the coefficient of friction from 0.3 to 0.2. The cantilever bending test performed on Cu-Gr-Cu nanolaminate showed an increase in flow strength and strain hardening compared to Cu-Cu.

The enhancement in the mechanical and friction properties of Cu-Gr-Cu nanolaminate suggests a build-up of dislocations at the Cu-Graphene interface. FEA simulations of the nanoindentation on Cu-Gr-Cu nanolaminate confirm the effectiveness of graphene as a barrier to plastic deformation.

The pile-up of dislocations at the Cu-Graphene interface implies large plastic strain gradients near the interface. We developed a strain gradient plasticity computational model of the beam bending experimental system based upon Gudmundson's higher-order theory and implemented it as a user element in ABAQUS. A set of material parameters is identified that reproduce the experimental force vs. displacement results for both the Cu-Cu and the Cu-Gr-Cu nanolaminate. The only difference in the simulations is that zero plastic strain boundary conditions are enforced at the Cu-Gr interfaces in the Cu-Gr-Cu nanolaminate. The results give insight into the design of metal-graphene composites and the structure of strain gradient plasticity theories.

# Table of Contents

# List of Figures

# List of Tables

## Acknowledgements

My scientific journey, like that of many others, was filled with trials and tribulations along with moments of ecstasy and an immense sense of scientific achievement. This rollercoaster ride would not have been half as exciting as it was if it was not for Columbia University and the extraordinary minds that I had the opportunity to work with.

First and foremost, I want to express my deepest gratitude to my advisor, Prof. Jeffrey Kysar. I consider myself extremely privileged to have been mentored by him. He gave me the scientific freedom to pursue exciting and challenging problems and encouraged my growth as a researcher. Jeff taught me to see progress in success and in failure, and his words "Shruti, this is great progress" will always remain with me. He is the epitome of humility, kindness, and inclusivity.

The work presented here is the result of collaboration with several people. I thank Prof. Katayun Barmak and Dr. Amir Zangiabadi for their help and advice on the transmission electron microscopy study. I would also like to thank Prof. Christian Niordson and Prof. Emilio Martinez-Paneda for a fruitful collaboration on strain gradient plasticity. I will always be grateful to have crossed paths with them. I am also thankful to the Imaging and Nanofabrication facilities staff at CUNY Advanced Science Research Center for their support.

I was blessed to be surrounded by many supportive colleagues and friends. I was fortunate to share my graduate school path with Richard Li. I worked with Rich to develop the fabrication methodology for Cu-Gr-Cu nanolaminates and found his calm demeanor and ability to remain unfazed even when the chips were down reassuring. I thank Dr. Christopher DiMarco

for generously sharing his time and expertise on CVD graphene growth and showing me the ropes when I first joined the lab. Chris is an excellent researcher and an even better friend. Over my six years at the Kysar lab, I had the privilege to work with and learn from several brilliant postdocs and graduate students, in many of whom I have found friends for life. I want to thank Dr. Christopher DiMarco, Richard Li, Dr. Hirobumi Watanabe, Dr. Dimitrios Fafalis, Dr. Miguel Arriaga, Dr. Thomas Rousseau, Aykut Aksit, Wenbin Wang, Chaoqun Zhou and Abby Herschman.

During my time at Columbia, I discovered my passion for teaching and want to thank Prof. Jeffrey Kysar, Prof. James Hone, Prof. Karen Kasza, and Prof. Richard Longman for allowing me to teach the curious, bright, and diligent students of Columbia University. I want to give a special shoutout to Prof. James Hone, whose enthusiasm to teach mechanics was infectious.

I would also like to thank the members of my committee, Prof. James Hone, Prof. Christen Myers, Prof. Emilio Martinez-Paneda, and Prof. Irving Herman, for their time and contributions.

Finally, I want to express my gratitude to my family. This work would not have been possible without my family's unwavering faith in my ability, even when I doubted it myself. My parents always encouraged my curiosity and scientific temperament even as a kid. They backed my ambitions and inspired me to dream big. Their unflinching, unconditional support, and love has made this dissertation a reality. I thank my 6 feet 3-inch tall baby brother, Ashwin, for being a level-headed voice of reason. His wise words and coding skills have been invaluable to me. Finally, I would like to thank my husband, Vikas, for always bringing in humor and making me laugh even when I was most stressed.

# Dedication

To my Thatha and Avva (grandparents), S.K Sadasivam and Sarada Sadasivam

# Chapter 1: Introduction and Background

Since its discovery in 2004, graphene – a single atomic layer material – has been touted as one of the most promising two-dimensional materials. Graphene consists of a single layer of carbon atoms covalently bonded in a hexagonal lattice. Its exceptional electrical [1], optical [2], thermal [3], and mechanical properties [4–6] make it perfect for many applications ranging from next-generation transistors to transparent electrodes [1], flexible electronics [7], membranes for nanopore DNA sequencing [8], and nanomechanical systems. However, it is crucial not to lose sight of its most beautiful property: *Graphene is a 2D material*. It is impossible to make a stable crystal that is thinner than graphene. This wonderful property allows us to push the boundaries of the well-established field of nanomechanics to their ultimate limit by fabricating novel composites with graphene. Understanding the mechanical behavior of graphene and graphene-composites is critical to realizing these next-generation technologies.

Nanolaminate structures are present in abundance in nature. For example, pearlite is a nanolaminate formed by the decomposition of austenite by eutectoid reaction into a lamellar arrangement of ferrite ($\alpha - Fe$) and cementite ($Fe_3C$). The lamellar morphology of the two constituent phases, ferrite, and cementite, is evident from Fig. 1.1. The black deposit is cementite, while the gray deposit is ferrite. Ferrite is a ductile material and is relatively weak while cementite is a hard, brittle material (generally classified as a ceramic). At small plastic strains, the dislocation motion leads to plasticity in the ferrite. The dislocations pile up at the boundaries between ferrite and cementite thus increasing the strength of pearlite at small plastic strains. However, at large plastic deformation, cracks can initiate in cementite leading to catastrophic failure of pearlite. Pearlite's lamellar microstructure serves as motivation for us to synthesize Cu/Gr nanolaminate composites. Graphene/copper lamellar composites may serve to block the dislocations without the cracking

that occurs in cemintite of pearlite.

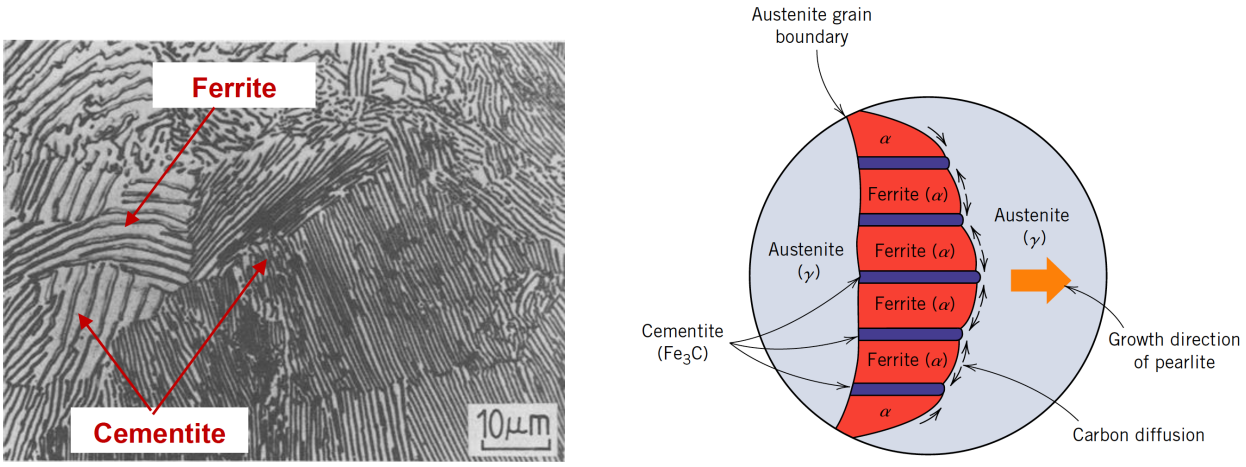


(a) (b)

Figure 1.1: (a) Photomicrograph of a eutectoid steel showing the pearlite microstructure consisting of alternating layers of $\alpha$-ferrite (the light phase) and $Fe_3C$ (thin layers most of which appear dark). Adapted from Kapito et al. [9]. (b) Schematic representation of the formation of pearlite from austenite. Adapted from Callister Jr. and Rethwisch [10]

Graphene, though brittle, has high strength and modulus and can thus withstand large plastic deformation. Another shortcoming of pearlite is that we can not control the lamellar thickness of each layer. However, the advancements in metallurgy and material science have now allowed us to control the layer thickness deposited while synthesizing a laminate structure.

The objective of this thesis is twofold. The first objective is to understand the mechanical behavior of graphene and Cu/Gr nanolaminates. The second objective is to synthesize these graphene composites such that they are industrially scalable.

## 1.1 Background

### 1.1.1 Brief Review of Graphene's Mechanical Strength

Lee et al. [4] probed the mechanical properties of exfoliated graphene by suspending them as circular membranes and subjecting them to a point load via nanoindentation. They found that graphene's strength approached its theoretically predicted strength [11]. Wei et al. [12] introduced a more comprehensive $5^{th}$ order nonlinear anisotropic constitutive relationship based on

first-principle calculations through density functional theory and validated it against the experiments through a multiscale model [5]. The analysis showed that graphene is the strongest material characterized – 100X stronger than steel. It exhibits the highest-known intrinsic strength in excess of 100 GPa and a Young's Modulus of 1 TPa [4], thus providing us with an opportunity to engineer metal/graphene composites with strengths that do not naturally occur.

Mechanically exfoliated graphene is limited in its lateral dimensions (100 µm). Hence, if we wished to utilize the graphene in real-world applications, it became imperative to find industrially scalable methods of synthesizing graphene while maintaining its mechanical properties.

Large-area graphene sheets grown via chemical vapor deposition (CVD) is a step towards achieving this goal. Graphene produced via CVD is polycrystalline and thus possess grain boundaries. Theoretical studies have argued that these grain boundaries can be nearly as strong as the pristine lattice, with the strength varying with tilt angle and arrangement of defects [13]. Lee et al. [6] probed the mechanical properties of suspended CVD graphene membranes using nanoindentation and showed that the elastic stiffness of graphene is identical to that of pristine graphene. In addition, the maximum strength given by the average breaking force of the polycrystalline graphene is only 5% smaller than the intrinsic strength. Indentation tests directly on the grain boundaries result in grain boundary strength that is only 10% smaller than the intrinsic strength of graphene.

Defects are an inevitable consequence of increased scale, so it is vital to understand the effects of the defects on the mechanical strength of graphene. The effect of point defects on the mechanical properties of graphene is studied by oxidation of membranes using a weak oxygen plasma [14]. It was found that the two-dimensional elastic modulus of graphene was maintained even at a high density of $sp^3$-type defects. Moreover, the breaking strength of defective graphene was only 14% smaller than its pristine counterpart in the $sp^3$-defect regime. However, a significant drop in the mechanical properties of graphene was reported in the vacancy-defect regime.

In this work, we incorporate CVD-grown graphene (as a strength enhancer) into a nanolaminate structure with alternate layers of copper and graphene sheets. To this end, it is crucial to

understand the mechanical behavior and the deformation mechanism of nanolaminate structures. The following section provides an overview of the mechanics of nanolaminates.

### 1.1.2 Mechanical Behavior of Metallic Nanolaminates

Scientists constantly endeavor to enhance the properties of materials. Altering the microstructure of a material holds the key to designing a composite with enhanced mechanical properties. This bottom-up approach allows us to design a material that provides the desired functionality for various applications. Recently, nanolaminates — a group of composite materials made up of alternating nanometer-scale layers of two different metals, metal-ceramics or non-metals — have been the object of considerable research as they allow us to engineer materials with enhanced strength [15–17].

In metallurgy and material science, it is common to refine the grain size of metals to the tens of micrometer range to increase the yield strength of the material. In nanostructured metallic multilayers, physical vapor deposition (PVD) allows the synthesis of structures with a layer thickness in the range of a few to ten nanometers, thus making interlamellar spacing the relevant microstructural length scale and allowing engineers the opportunity to synthesize materials with enhanced strength. For instance, a nanolaminate [18, 19] such as [111]Cu-[110]Nb with an interlamellar thickness of few nanometers has its flow strength approach 2.4 GPa which is a factor of 2 to 3 of the intrinsic strength of Cu. In contrast, the constituent pure metals in the bulk form may have yield strengths in the range of a few tens of MPa. Furthermore, the strength of these nanoscale multilayers is usually a factor of two to three higher than the rule-of-mixtures estimate using the strengths of the monolithic constituent layers [15, 20]. The strength of the above metal nanolayered composite system has been enhanced due to the introduction of high-density interfaces that block dislocation motion.

J. S. Koehler was the first to demonstrate that preparing a specimen with alternate layers of material with high and low elastic constants — each layer having a thickness of a few  nm — restricts dislocation motion since a Frank-Read dislocation source can not operate inside the layer,

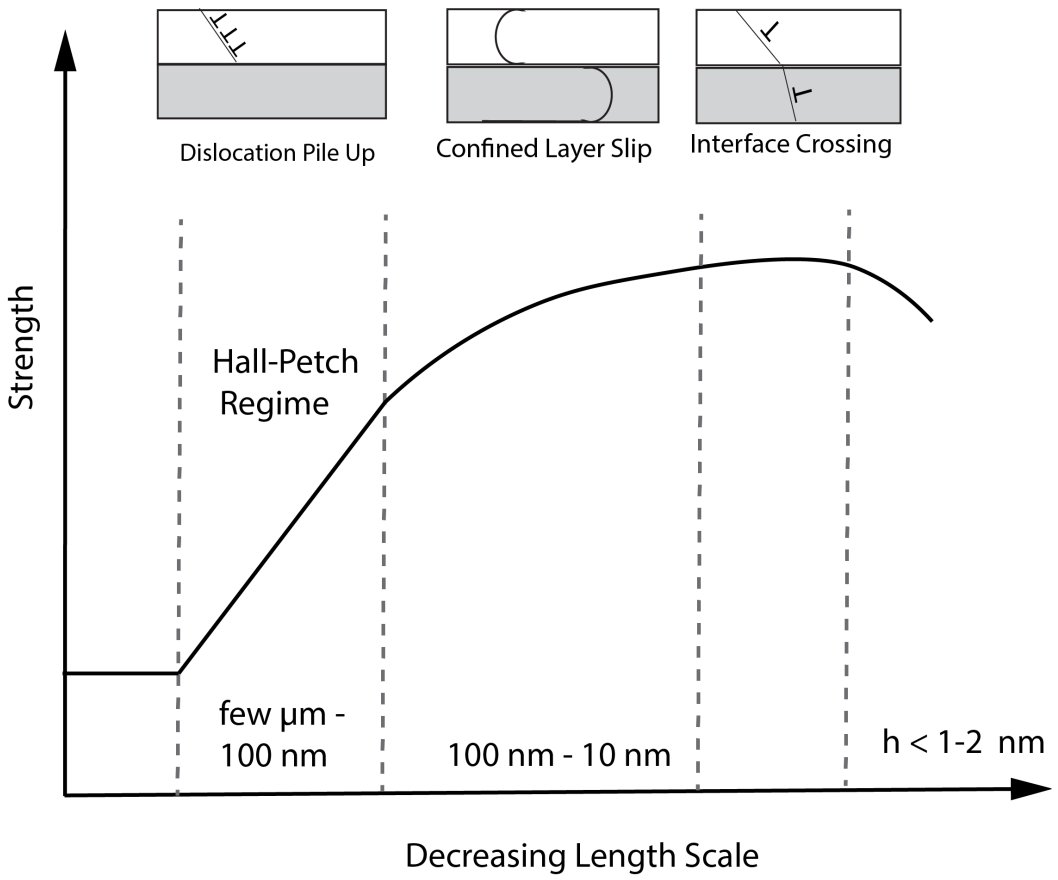


Figure 1.2: Evolution of strength of nanolaminates with decreasing layer thickness.

making the material stronger [21]. The failure strength, $\sigma_f$, of metallic multilayers evolves as a function of layer thickness, $h$ (Fig 1.2). The strength of the metallic multilayer increases in accordance to the Hall-Petch relation ($\sigma_f \propto h^{-0.5}$) for $h$ values between a few microns and 100 nm. The strength continues to increase with decreasing layer thickness until $h = 10$ nm according to the relation: $\sigma_f \propto h^{-a}$, where $a \neq 0.5$. A saturation in strength is then observed when the layer thickness is a couple to a few nanometers. Finally, the strength decreases with decreasing layer thickness, typically for $h$ below a couple of nanometers [22].

The schematic shown in Fig. 1.3 explains the strengthening mechanism of nanolaminates in the Hall-Petch regime. The dislocations formed due to material deformation move within material A and pile up at the interface until the applied stress plus the stress concentration due to the pile-up exceed the barrier strength and transmits slip across the boundary (Fig. 1.3(a)). At smaller layer thicknesses (Fig. 1.3(b)), the number of dislocations in the pile-up is small. Hence, the resulting

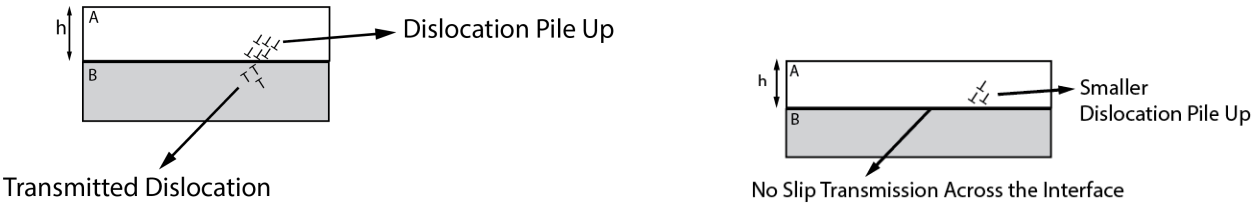


(a) (b)

Figure 1.3: Schematic explaining the strengthening mechanism of nanolaminates in the Hall-Petch regime. As the layer thickness reduces, larger stress needs to be applied for slip transmission across the interface.

stress concentration is small, and larger applied stress will be required for slip transmission across boundaries. This continuum model applies to sub-micrometer length scales.

As the layer thickness in metallic nanolaminate is decreased below a few tens of nanometers, dislocation pile-ups cannot form in nanoscale multilayers, and the deformation behavior involves nucleation and motion of single *hairpin* dislocation loops that deposit misfit-type dislocations at the interface and transfer the load to the other, elastically deforming layer. Yield occurs when the slip is eventually transmitted across the interface interpreted as *confined layer slip*. The peak strength reached when the layer thickness is a couple of nanometers is interpreted as the stress needed to transmit a single glide dislocation across the interface (*interface crossing*). When the layer thickness is below the typical dislocation core dimensions of 1 nm, the stress required to cross the interface for single dislocation transmission drops significantly, thus decreasing the strength of the nanolaminate.

Hence, interfaces in these nanolaminates play a pivotal role in providing increased resistance against dislocation propagation across the interface, thus enhancing the nanolaminate's strength. For example, Cu films of a few hundred nanometer thickness having $TiN/Si_3N_4$ as interfaces (passivated layer) show a notable increase in work hardening rate and a strong Bauschinger effect as compared to unpassivated Cu films [23]. Here, dislocations get pinned at the interface leading to them being blocked from exiting the Cu film. Similarly, when nanopillars of alternating lamellar Cu-Gr composites and Ni-Gr composites were loaded in compression [24], the graphene interface served as a barrier to dislocation-formed slip steps, thus enabling ultra-high strengths of 1.5 GPa

to 4 GPa for Cu-Gr and Ni-Gr composites, respectively. On the other hand, slip step formation at interfaces was observed in metal-only multilayers. In another study, the same graphene interface that blocked dislocations to increase the strength of the lamellar Cu-Gr composite was shown to have a pronounced effect on blocking and deflecting the fatigue cracks generated within the Cu layer, resulting in a 5-6 times increase in fatigue resistance when compared to a conventional copper thin film [25].

### 1.1.3 Smaller is Stronger

The fact that metals at micron-scale exhibit a strong size effect has been well known since the discovery of the Hall-Petch effect, which states that the yield strength of pure metals increases with diminishing grain size. Since the 1990s, various experiments revealed that metals, when subjected to simple overall deformation such as bending and torsion, exhibit micron-scale size effects. Fleck et al. [26] showed that thin crystalline copper wires gain increased plastic resistance when subjected to torsion. Fig. 1.4(a) represents the torsional response of copper wires of diameter (2a) in the range 12 μm to 170 μm [26]. An increase in torsional resistance is observed with decreasing diameter of the copper wire. However, according to conventional plasticity, the plots of normalized torque $Q/a^3$ vs. $Ka$ should lie on the same curve, and the torsional response should be independent of the size of the diameter.

Size-effects in metals are also observed in complex deformation states such as indentation. Stelmashenko et al. [27] and Ma and Clarke [28] used self-similar indenters, such as Berkovich and Vickers indenters, to quantify the size effects observed at the micron-scale. They performed a series of indentations on tungsten and silver and reported that the metal's hardness increased with decreasing indenter diagonals Fig. 1.4(c). In a length scale-independent material, hardness measurements with self-similar indenters should yield size-independent measurements, as there is only one independent length scale characterizing the deformation state, such as the indent depth or indenter diagonal.

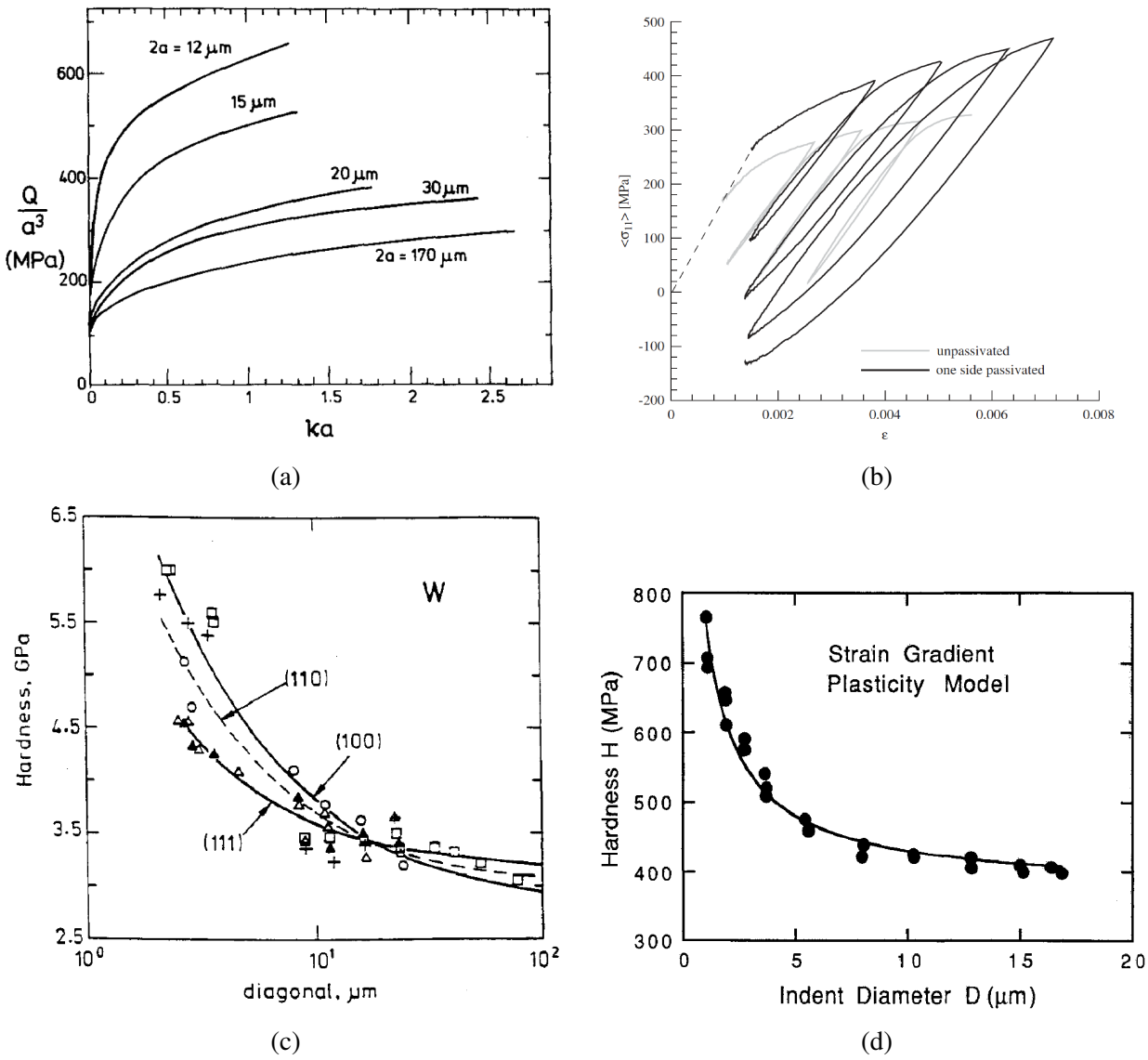


Figure 1.4: Smaller is stronger effect seen in metal at micron-scale. (a) Torsional resistance of thin copper wires increases with decreasing wire thickness (Adapted from Fleck et al.,1994). (b) Thin film bulge test of one side passivated shows an increase in strength and strain hardening compared to unpassivated film (Adapted from Nicola et al.,2006). Size effect is seen in nanoindentation of (c) W (Adapted from Stelmashenko et al.,1993), and (d) of Ag (Adapted from Ma and Clarke,1995).

A common theme emerges in all the above examples: the smaller the characteristic length stronger is the mechanical response. Hence, to interpret the size effect seen in metal, a length scale needs to be included in the conventional plasticity theory. Phenomenological theories postulate that the yield stress depends both upon strain and strain gradient, and the size effects are associated with large plastic strain gradients [29]. Plastic strain gradients are inversely proportional to the characteristic length. The presence of large plastic strain gradients requires the storage of geometrically necessary dislocations (GNDs) [30].

Xiang and Vlassak [31] quantified a size-effect due to plastic strain gradients induced by applying an ultra-thin passivation layer blocking dislocations on one side of a thin copper film deformed homogeneously in a plane strain bulge test. The passivated film displayed an increase in strength and strain hardening when compared to the unpassivated film (Fig. 1.4(b)). Similarly, the Hall–Petch effect can be interpreted in the context of large plastic strain gradients. Since grain boundaries act as obstacles to dislocation movement, dislocations pile up, thus leaving a plastic strain gradient near grain boundaries. Hence, decreasing the grain size implies larger plastic strain gradients at a given overall plastic strain.

## 1.2 Thesis Outline

It is impressive to note that the inclusion of a single atomic layer of graphene can enhance the strength and fatigue resistance of the composite (section. 1.1.2). In this thesis, we seek to further our understanding of the role graphene plays in enhancing the load-bearing capacity, frictional behavior, and strength of the synthesized Cu-Gr-Cu nanolaminate. By choosing a nanolaminate structure, we allow for uniform and controlled placement of graphene within the metal matrix resulting in higher reinforcement contribution. Moreover, we wish to demonstrate an industrially scalable and transfer free Cu-Gr nanolaminate material design, comprising of alternate layers of Cu and chemical vapor deposition (CVD) graphene.

To accomplish this, we can define three primary research areas:

- **Increased Hardness of Cu-Gr-Cu nanolaminate:** A series of nanoindentations performed

on Cu-Gr-Cu nanolaminate evaluate the load-bearing capacity of the composite.

- **Improved Frictional Properties of Cu-Gr-Cu nanolaminate:** Scratch tests performed on the free surface of Cu-Gr-Cu nanolaminate probe the frictional properties of the composite.
- **Enhanced Strength of Cu-Gr-Cu nanolaminate:** Cantilever beams of the Cu-Gr-Cu nanolaminate are fabricated using Focused-ion-Beam (FIB). Bending tests performed on the fabricated cantilever beams evaluate the enhancement in strength due to a single atomic layer of graphene.

Finite Element Analysis (FEA) simulations of nanoindentation, scratch test, and cantilever beam bending are performed to gain further insight into graphene's role during deformation.

This thesis is organized as follows: In chapter 2, we summarize the fabrication of Cu-Gr-Cu nanolaminate. Since grain size plays a vital role in evaluating the mechanical properties, the microstructure of the composite is characterized using Electron Backscatter Diffraction (EBSD) and Transmission Electron Microscopy (TEM) orientation mapping technique. Chapters 3, 4, and 5 elucidate the three research areas defined above. Nanoindentation, scratch test, and beam bending of Cu-Gr-Cu nanolaminate demonstrate graphene's effectiveness in blocking dislocations at the Cu-Gr interface and enhancing the strength and frictional behavior of the composite. Finite Element Analysis supports the findings in each of the above experiments.

The pile-up of dislocations that occurs at the Cu-Gr interface leaves large plastic strain gradients near the interface. A strain gradient plasticity computational (SGP) model of the beam bending experimental system was employed in chapter 5. The computational model is based on Gudmundson's higher-order theory implemented as a user element in ABAQUS. The SGP simulations reiterate graphene's ability to block dislocation motion and enhance the strength of the beam. Finally, in Chapter 6, we summarize the significant contributions and discuss the future work.

# Chapter 2: Synthesis of Cu-Gr-Cu nanolaminate

With its exceptional mechanical property and 2D nature, graphene can be an outstanding reinforcement in metal matrix composites (MMC). In recent years, graphene reinforced metal matrix composites (GRMMCs) have exhibited excellent thermal and mechanical properties, making them suitable for a wide range of applications in catalysis, electronics, energy storage, sensing, and biotechnology [32–34]. The current synthesis process of GRMMCs involves graphene/graphene-oxide being incorporated into the metal matrix via various mechanical and chemical methods like liquid metallurgy, powder metallurgy, ultrasonic dispersion, and electrodeposition [35]. However, the current graphene-metal composites have several limitations : (1) non-uniform dispersion of graphene in the metal matrix, (2) agglomeration of graphene/graphene oxide platelets, (3) weak interface adhesion between graphene and the metal matrix, (4) lower reinforcement strength of graphene derivatives (graphene oxide or reduced graphene oxide) compared to exfoliated graphene. The above challenges stem from GRMMCs' fabrication process and the use of graphene derivatives (graphene oxide or reduced graphene oxide) as strength enhancers.

In this work, we choose a nanolaminate microstructure with alternate layers of Cu film and graphene (Cu-Gr-Cu). The nanolaminate structure ensures the uniform and controlled distribution of graphene. In addition, there is an excellent (and tailorable) adhesion between graphene and the metal matrix. Graphene grown via chemical vapor deposition are polycrystalline in nature. Lee et al. [6] probed the mechanical properties of suspended CVD graphene membranes using nanoindentation and showed that the elastic stiffness of graphene is identical to that of pristine graphene. Furthermore, its strength is only slightly reduced despite the existence of grain boundaries, thus providing higher reinforcement strength compared to various graphene derivatives. Moreover, graphene grown on Cu substrates via chemical vapor deposition (CVD) takes us a step closer to an

industrially scalable synthesis.

## 2.1 Fabrication of Cu-Gr-Cu nanolaminate

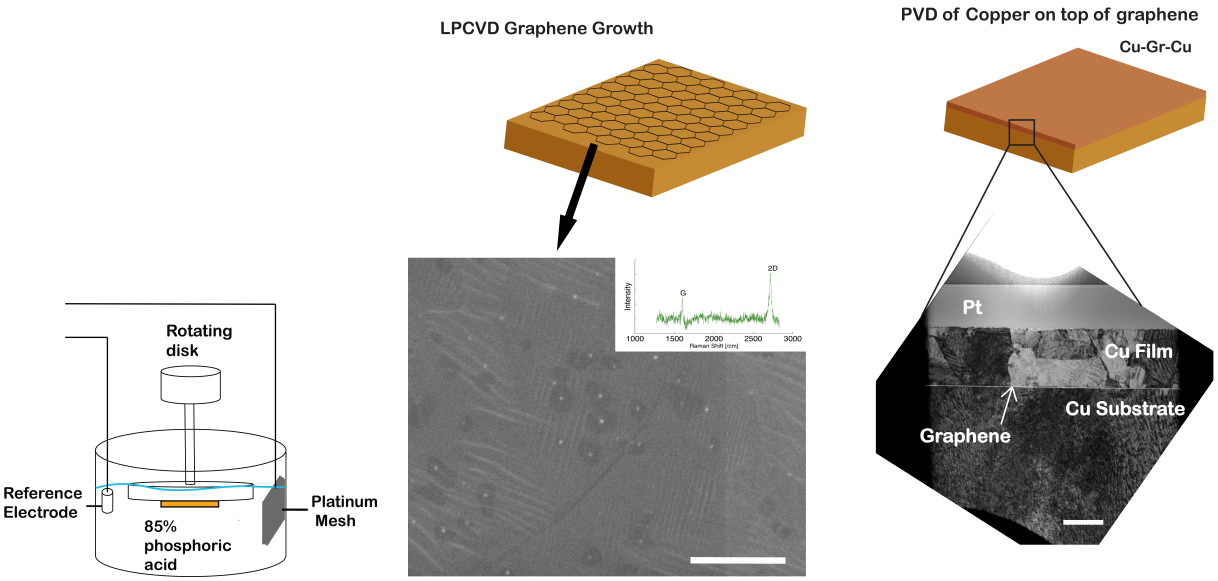


Figure 2.1: Schematic of Cu-Gr-Cu nanolaminate synthesis, (a) electropolishing of Cu substrate, (b) SEM image of graphene on Cu substrate. Scale bar 3 µm. Inset shows Raman spectra of graphene, (c) cross-sectional TEM image of Cu-Gr-Cu nanolaminate. Scale bar 500 nm.

A high purity, 1 mm thick, polycrystalline copper substrate (Alfa Aesar, 99.9999%) is electropolished using Rotating Disk Electrode (RDE) polishing to remove surface contamination and reduce the root mean square surface roughness to less than 2 nm. Electropolishing helps to reduce graphene nucleation density during growth. A platinum mesh (Alfa Aesar), used as a cathode, is dipped into an 85% (by volume) phosphoric acid electrolyte at ambient temperature, shown schematically in Fig. 2.1(a). The copper substrate mounted on a rotating disk, which acts as an anode along with a Gamry Calomel reference (Ag/AgCl) electrode, is dipped into the electrolyte. The disk is rotated at 700 rpm while varying the voltage from 0 mV to 2000 mV to obtain a current at which the voltage remains constant. This current and rotating speed is used to electropolish the copper substrate to remove upto 110 µm of material thickness and reduce the surface roughness to less than 2 nm.

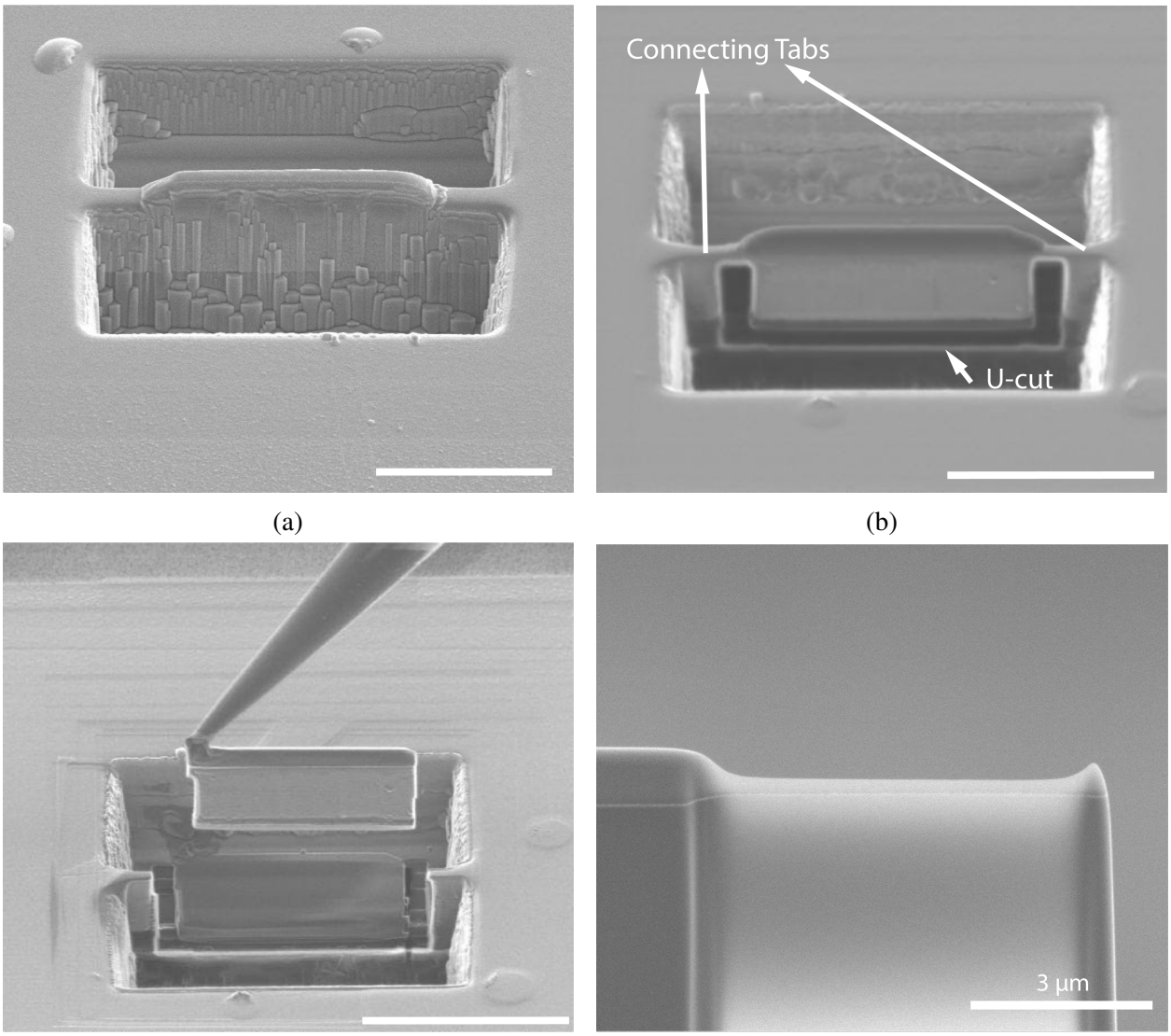


(a) (b)

(c) (d)

Figure 2.2: Lift-Out TEM cross-sectional sample fabrication steps, (a) milling two trenches on either side of Pt deposit, (b) milling a U-cut, (c) lift-out of the TEM cross-sectional sample, (d) final electron transparent TEM cross-sectional sample attached to a TEM grid. Scale for (a), (b) and (c) is 10 µm.

A continuous single atomic layer of graphene is then grown on the substrate via chemical vapor deposition (CVD) at 1000 °C for 30 min using methane as the precursor gas. The electropolished copper substrate is first annealed at 1000 °C for 2 hrs in a gas mixture of $H_2$ (5 sccm) and Ar (50 sccm) at 1 Torr. During graphene growth, methane and hydrogen flow at 5 sccm and 10 sccm, respectively, while maintaining a pressure of 0.3 Torr. Fig. 2.1(b) shows a scanning electron mi-

croscope (SEM) image of the graphene film. Raman spectroscopy (inset of Fig. 2.1(b)) confirms that the resulting graphene is mostly a single atomic layer with an excellent G/2D ratio of 1/3 [12, 36].

Next, a high-purity Cu film of thickness 700 nm is deposited via physical vapor deposition (PVD) at room temperature atop the graphene to synthesize a Cu-Gr-Cu nanolaminate. Fig. 2.1(c) presents a cross-sectional bright-field transmission electron microscopy (TEM) image taken at the Cu/Gr/Cu interface. In the TEM image, the Cu substrate is an individual grain, so effectively is a single crystal for the length scale shown here, the straight line at the interface of the Cu film, and the Cu substrate denotes a single atomically-thin layer of graphene. The Cu film deposited atop the graphene is polycrystalline.

The TEM cross-sectional sample is fabricated using the "Lift-Out" technique. First, a micrometer thick platinum film was deposited on the Cu film while fabricating the TEM sample using Focused-Ion Beam (FIB) to protect the Cu film from damage due to ion bombardment during the milling and thinning process of TEM sample preparation. The protective platinum layer was deposited using an ion current of 0.28 nA and with the energy of 30 kV. Next, two trenches were milled on either side of the Pt deposit using a large ion current of 15 nA. In order to ensure the sides of the cross-sectional sample were smooth and parallel to each other, the ion current was changed to 1 nA to mill both sides of the cross-sectional sample until the sample thickness was 500 nm. The stage was then titled to 0°, and a "**U**" was milled out, leaving a small connection tab on either side of the sample (see Fig. 2.2). Next, an Omniprobe (Lift-Out) needle was brought close to the top right corner of the Pt deposit. The tip of the Omniprobe was spot welded using Pt to the cross-sectional sample using a low ion current of 30 pA. The connecting tabs were milled away, and the Omniprobe was withdrawn to "Lift-Out" the cross-sectional sample. The cross-sectional sample was then attached to TEM grids. The final step of the fabrication process involved thinning the cross-sectional sample such that the sample becomes electron transparent. The ion beam accelerating voltage and the current were progressively reduced as the sample got thinner to reduce the ion beam induced sample damage (e.g., sample amorphization, gallium implantation).

For comparison, a control — Cu-Cu nanolaminate — sample (not shown) was fabricated according to the procedure described above; however, methane did not flow through the furnace during the graphene growth stage, ensuring that both nanolaminate structures were subjected to the same thermal cycle. Optical and SEM images of the Cu substrate after annealing confirmed no change in surface roughness due to annealing. Another alteration while fabricating the control sample was to deposit the Cu film at 200 °C on the Cu substrate to ensure similarity in the grain size distribution of the Cu film in both Cu-Gr-Cu and Cu-Cu nanolaminate structure.

## 2.2 Microstructural Characterization

Grain size and grain orientation play a fundamental role in determining the mechanical behavior of a polycrystalline material. The grain size of the PVD Cu film was measured using Electron Backscatter Diffraction on a Zeiss Sigma VP Scanning Electron Microscope (SEM) at 20 kV with a working distance of 13.5 mm. TexSEM Laboratories Orientation Imaging (TSL OIM$^{TM}$; EDAX, Mahwah, NJ, USA) software was used to analyze the data. Fig. 2.3(a) and Fig. 2.3(b) show the measured grain size and orientation of Cu-Cu nanolaminate and Cu-Gr-Cu nanolaminate, respectively. The grain size distribution shown in Fig. 2.3(c) and Fig. 2.3(d) indicates that the mean grain size of the Cu film is 300 nm for both Cu-Cu and Cu-Gr-Cu nanolaminate structures.

As seen in Fig. 2.3(c) and (d), the grain size distribution of the Cu film in Cu-Cu nanolaminate is slightly broader than the grain size distribution of the Cu film in Cu-Gr-Cu nanolaminate. Kurzydeowski and Bucki [37] investigated the effect of grain size distribution on hardness. They measured the Brinell hardness on grains sizes ranging from 19 µm to 64 µm and found that the differences in the distribution function resulted in a systematic deviation from the Hall-Petch equation. For a mean grain size of 38 µm and a coefficient of variation of 0.78,, the Brinell hardness was reported to be 10.2% lower than the predicted hardness from the Hall-Petch equation. Specimens characterized by a higher diversity of grain sizes exhibited lower hardness than predicted by the Hall-Petch relation. Similarly, Berbenni et al. [38] showed that the overall yield stress depended not only on the mean grain size but also on the dispersion of the distribution. For a mean grain size

of 4 µm, they reported a decrease in yield stress by 19.2%.

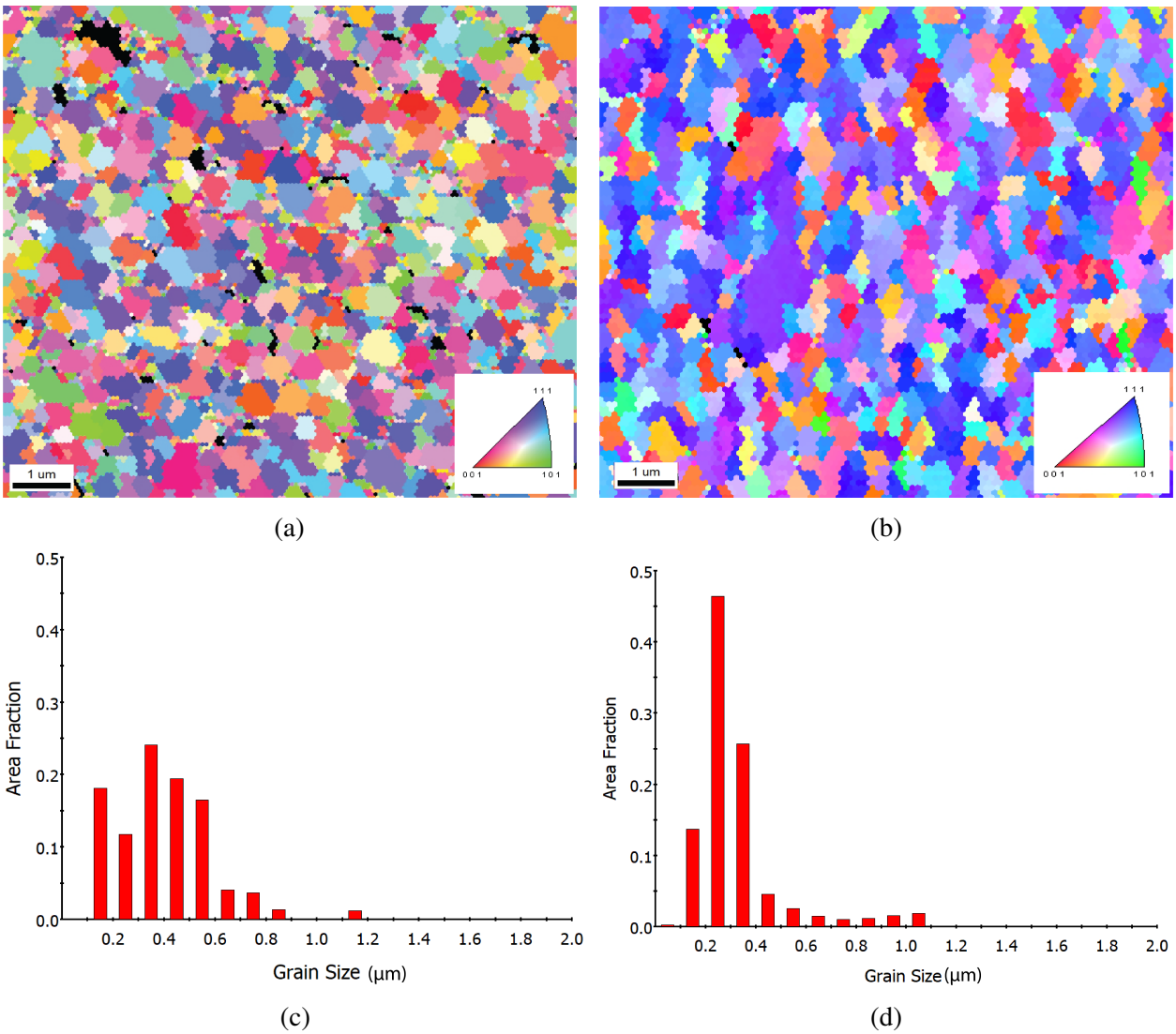


Figure 2.3: EBSD mapping (a) Inverse Pole Figure (IPF) map for Cu-Cu, (b) IPF map for Cu-Gr-Cu, (c) grain size distribution for Cu-Cu, (d) grain size distribution for Cu-Gr-Cu.

In this study, we have not considered the effect of grain size distribution on the mechanical properties of the Cu film. Given graphene's high strength, we expect any strengthening seen in the Cu-Gr-Cu nanolaminate to be due to graphene and not due to the difference in the grain size distribution. Moreover, the grain sizes in the above two studies are two orders of magnitude larger than the grain sizes in our work. In micrometer grain size, dislocation are nucleated in the grains via Frank-Read sources. However at 300 nm grain size in our work, dislocation nucleation from

grain boundaries rather than Frank-Read sources [39] are the predominant sources. Grain boundary dislocation nucleation depends upon the details of the grain boundary [39], and therefore the nucleation criterion is not as sensitive to grain size distribution (as seen in Fig.1.2) as Frank-Read sources are for micrometer scale grains. Furthermore, for a mean grain size of 300 nm, the strength of nanocrystalline copper is expected to be independent of the texture [40]. Hence, neither the grain size distribution nor the difference in texture is expected to significantly influence the yield strength.

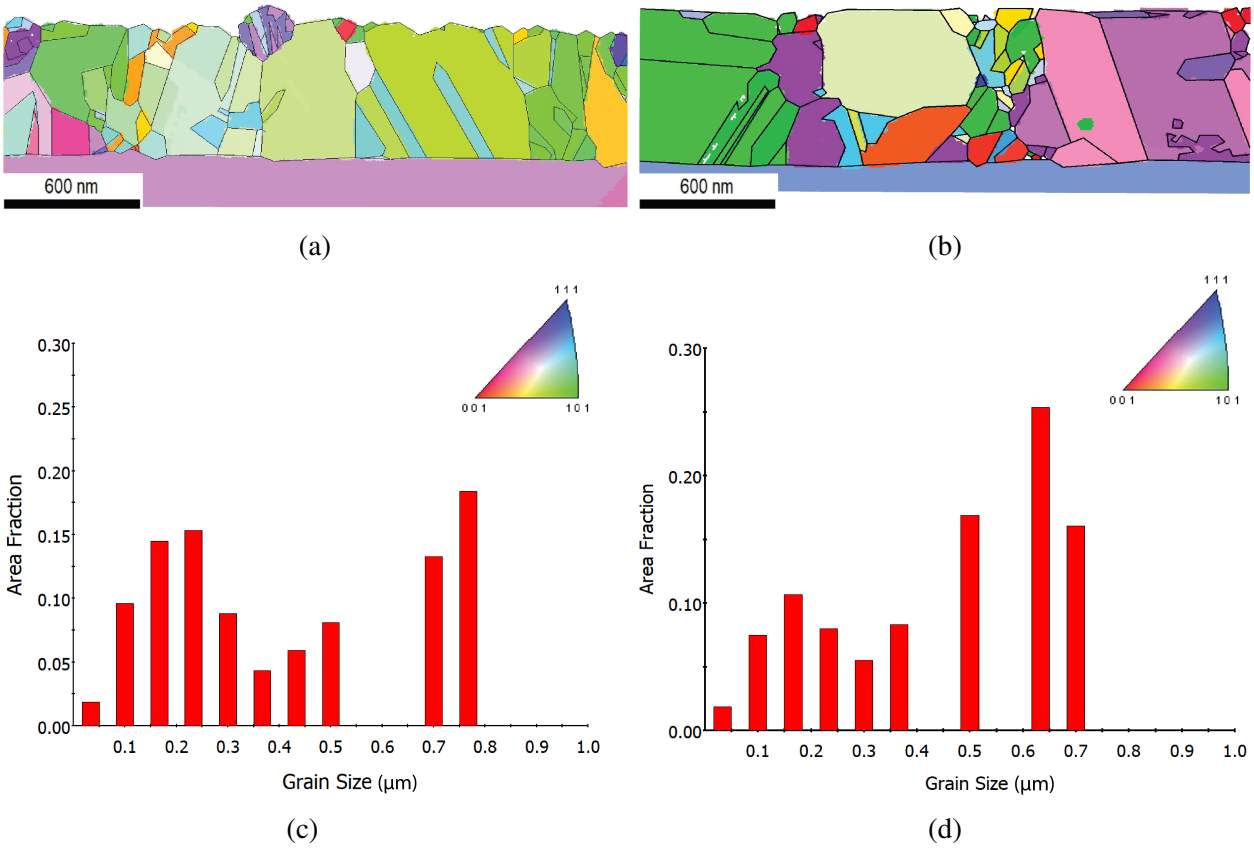


Figure 2.4: TEM Precession Electron Diffraction grain size analysis: (a) IPF map for Cu-Cu, (b) IPF map for Cu-Gr-Cu, (c) grain size distribution for Cu-Cu, (d) grain size distribution for Cu-Gr-Cu.

Since an SEM-EBSD has a resolution of 100 nm, and if we consider a general rule of thumb of collecting 10 data points per grain, then 1 µm becomes the lower limit of grain size measurement using SEM-EBSD. Hence, to measure the grain size of the Cu film with greater accuracy, we

use the recently developed TEM orientation mapping technique based on a collection of precession electron diffraction (PED) patterns, commercially known as ASTAR$^{TM}$ [41]. The diffraction patterns were collected on an FEI Talos S/TEM by scanning the electron beam with 12 nm step size at an accelerating voltage of 200 kV. The Inverse Pole Figure (IPF) maps for Cu-Cu, and Cu-Gr-Cu nanolaminate structures are shown in Fig. 2.4(a) and Fig. 2.4(b), respectively. The grain size distribution shown in Fig. 2.4(c) and Fig. 2.4(d) indicates that the grain size of the Cu film ranges between 200 nm to 600 nm for both Cu-Cu and Cu-Gr-Cu nanolaminate structures reiterating that the sole difference between the lamellar composite is the presence of a single atomic layer of graphene.

## 2.3 Mechanical Characterization

Micro-Vickers hardness data was obtained from a Leco LM-100 microhardness tester (LECO Corporation, St. Joseph, Michigan, USA) to determine the effective yield strength of Cu nanolaminates. A 300 g mass and a dwell time of 10 seconds were used. Ten micro-Vickers indentations were randomly placed on samples of the following alloys: Al6061, Cu182, Brass 360, Low Carbon Steel, and the high purity annealed Cu substrate. The micro-Vickers hardness values for each material were then averaged and are shown in Table 2.1. The yield strength of each material (except for the annealed Cu-substrate) at 0.2% offset was calculated using the stress-strain data obtained from tensile testing.

The correlation between Vickers Hardness and yield strength is shown in Fig. 2.5(a), indicating a linear relationship. Fig. 2.5(b) shows the correlation of the average nanoindentation data to micro-Vickers hardness data, indicating a linear relationship between data obtained using nanoindentation and micro-Vickers hardness test. Using the above two correlations and the nanoindentation hardness data, the yield strength of the annealed Cu substrate, as well as the effective yield strength of nanolaminates, Cu-Gr-Cu and Cu-Cu, can be obtained.

| Material | Vickers Hardness (MPa) | Yield Strength (MPa) | Nanoindentation Hardness (Gpa) |
|---|---|---|---|
| Al6061 | 654 | 269 | 0.850 |
| Cu182 | 1530 | 493 | 1.78 |
| Brass 360 | 1280 | 301 | 1.68 |
| Low-Carbon Steel | 2650 | 637 | 3.04 |
| Cu-substrate | 359 | 161 | 0.540 |

Table 2.1: Summary of Hardness and Yield Strength for Five Materials. The values in the table have been rounded to 3 significant figures.

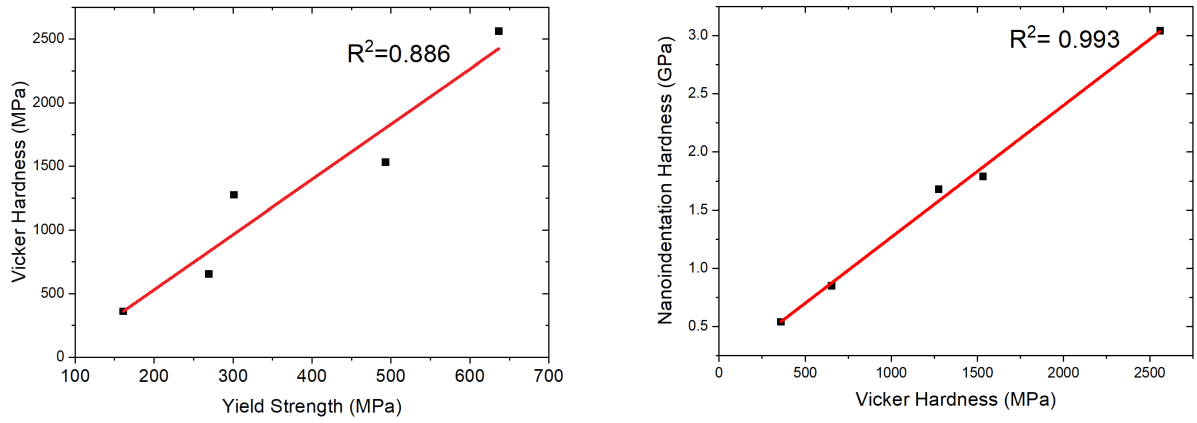


(a) (b)

Figure 2.5: Correlation between (a) micro-Vikers hardness and yield strength, (b) nanoindentation hardness and micro-Vikers hardness.

In summary, we report an industrially scalable transfer-free process to synthesize Cu-Gr-Cu nanolaminate. A continuous monolayer of high-quality graphene was grown on an electropolished high purity Cu substrate. A layer of Cu film was then deposited via physical vapor deposition on the grown graphene to synthesize the Cu-Gr-Cu nanolaminate. Grain size and grain orientation were measured using Electron Backscatter Diffraction on SEM and precession electron diffraction (PED) on TEM. The grain size distribution indicated that the grain size of the Cu film ranges between 200 nm to 600 nm for both Cu-Cu and Cu-Gr-Cu nanolaminate structures. Micro-Vickers hardness test was performed on a set of well-known alloys and the Cu substrate to determine the

effective yield strength of the Cu substrate to be 161 MPa. A correlation between the Vickers hardness and the yield strength was established. Another linear correlation between the nanoindentation hardness and the Vickers hardness was determined. These two correlations will be used in chapter. 3 to determine the effective yield strength of Cu-Cu and Cu-Gr-Cu nanolaminates.

# Chapter 3: Increased Hardness of Cu-Gr-Cu nanolaminate

Nanoindentation has proven to be a versatile method to determine the mechanical properties of materials containing nanoscale components [42, 43]. It can be used to measure Young's modulus, hardness, creep response, fracture toughness, and interfacial adhesion [44, 45]. Experimentation and modeling studies indicate [46, 47] that nanoindentation can distinguish the mechanical behavior of metals.

This chapter reports the measurement and calculation of the effective Young's modulus and effective flow strength of the synthesized Cu-Gr-Cu nanolaminate. We evaluate the enhanced load-bearing capacity and dislocation propagation barrier ability of graphene in Cu-Gr-Cu nanolaminate during deformation. Though nanopillar compression tests of Cu-Gr composites have already shown that the graphene interface provides an effective barrier to dislocation motion across the interface when loaded in compression, in nanoindentation, the sample surface becomes conformal with the probe tip shape, where deformation, other than perpendicular to the surface is introduced during loading. In the following sections, we outline the nanoindentation methodology and report the experimental results. Details of the FEA simulations of nanoindentation are presented in the finite element modeling section, along with the numerical results.

## 3.1 Nanolaminate Fabrication

A high purity, 1 mm thick, copper substrate (Alfa Aesar, 99.9999%) is electropolished using Rotating Disk Electrode (RDE) polishing to remove surface contamination and reduce the surface roughness to less than 2 nm. The Cu substrate is mounted on a rotating disk, which acts as an anode and is dipped into an 85% (by volume) phosphoric acid electrolyte. A platinum mesh (Alfa Aesar) is used as a cathode, while a Gamry Calomel (Ag/AgCl) electrode is used as a reference.

The Cu substrate is electropolished to remove 110 µm of material thickness and reduce the surface roughness to less than 2 nm.

A continuous single atomic layer of graphene is then grown on the substrate via chemical vapor deposition (CVD). The electropolished copper substrate is first annealed at 1000 °C for 2 hrs in a gas mixture of $H_2$ (5 sccm) and Ar (50 sccm) at 1 Torr. Graphene growth takes place at 1000 °C for 30 min using methane as the precursor gas. During the growth stage, methane and hydrogen flow at 5 sccm and 10 sccm, respectively, while maintaining a pressure of 0.3 Torr. Raman spectroscopy confirmed that the resulting graphene is primarily a single atomic layer with a good G/2D ratio of 1/3 [12, 36].

To ensure we capture the influence of graphene on the frictional behavior of the composite, a 700 nm Cu film is deposited onto single-layer graphene via physical vapor deposition (PVD) at room temperature to synthesize a Cu-Gr-Cu nanolaminate.

For comparison, a control — Cu-Cu nanolaminate — sample (not shown) was synthesized according to the procedure described above; however, methane did not flow through the furnace during the graphene growth stage, ensuring both nanolaminate structures were subjected to the same thermal cycle. Another modification while fabricating the control sample was to deposit the Cu film at 200 °C on the Cu-Substrate to ensure similarity in the grain size distribution of the Cu film in both Cu-Gr-Cu and Cu-Cu nanolaminate structure.

Grain size and grain orientation were measured using Electron Backscatter Diffraction on SEM and precession electron diffraction (PED) on TEM. The grain size distribution indicated that the grain size of the Cu film ranges between 200 nm to 600 nm for both Cu-Cu and Cu-Gr-Cu nanolaminate structures. The reader can refer to chapter2 for further details on the fabrication process and the grain size distribution charts.

### 3.2 Nanoindentation Experiments

The lamellar composite's mechanical behavior was tested by nanoindentation using a G200 Nanoindenter (KLA Corporation, Milpitas, CA, USA). A diamond Berkovich tip — a three-sided

pyramid diamond tip — was used to indent to a depth of 300 nm. When the depth limit was reached, the load on the indenter was held constant for 5 s. The indenter was then unloaded to 90% of the peak load at a rate equal to the maximum loading rate. Subsequently, the thermal drift was measured for 75 s. The indenter was then withdrawn from the sample completely.

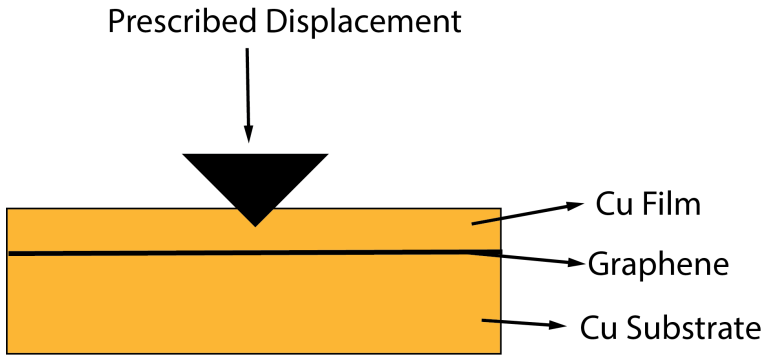


Figure 3.1: Schematic representing indentation into Cu-Gr-Cu nanolaminates using a Berkovich tip.

The nanoindentation tests were performed 15 times on Cu-Gr-Cu nanolaminate and 15 times on Cu-Cu nanolaminate.

### 3.2.1 Experiment Results

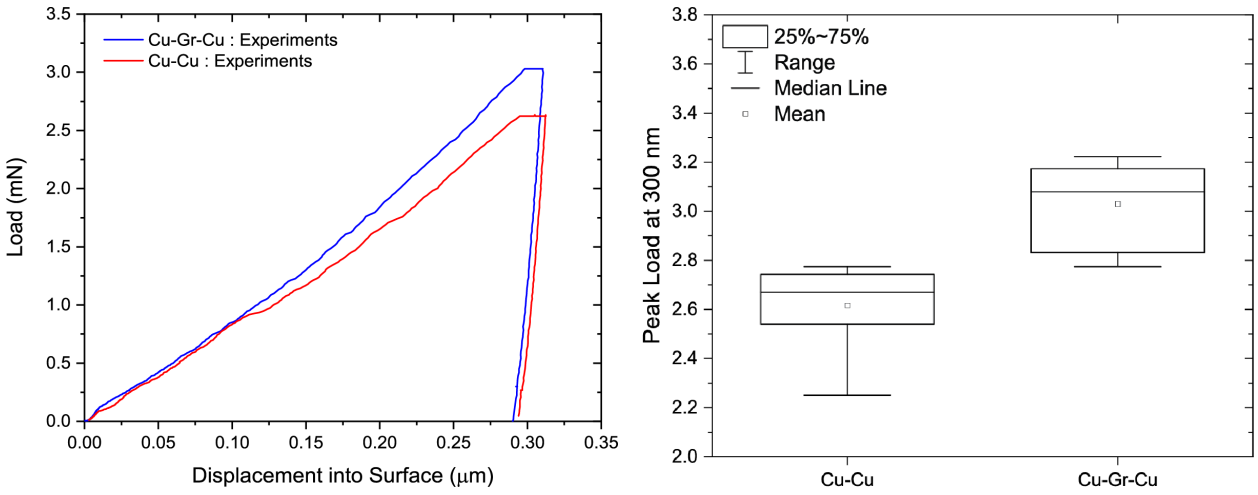


Figure 3.2: (a) Force-displacement curves for nanoindentation on Cu-Cu and Cu-Gr-Cu nanolaminate structure, (b) box plot representing the distribution of peak load measured at 300 nm.

The representative load-displacement curves for Cu-Cu nanolaminate and Cu-Gr-Cu nanolaminate are shown in Fig. 3.2(a). These load-displacement curves reveal that a significantly larger force is required to indent to a depth of 300 nm in Cu-Gr-Cu nanolaminate as compared to Cu-Cu nanolaminate suggesting improved load-bearing capacity in Cu-Gr-Cu nanolaminate. This increase in peak load and hence the strength of Cu-Gr-Cu is solely due to a single atomic layer of graphene. The mean of the peak load for Cu-Gr-Cu is 3.03 mN with a standard deviation of 0.16 mN, while the mean of peak load for Cu-Cu is 2.60 mN standard deviation of 0.16 mN. A two-sample t-test performed on the peak load data measured for Cu-Cu, and Cu-Gr-Cu nanolaminates resulted in a p-value of 0.000002. This p-value was much less than a significance level of 0.05, irrespective of the assumption of equal or unequal variance, reiterating that enhancement in strength of Cu-Gr-Cu nanolaminate is mainly due to the presence of single-layer graphene and not due to random noise in the data.

Another critical observation made from these force-displacement curves is that no interfacial material failure occurs at the Cu/Gr interface for an indentation depth of 300 nm into the 700 nm thick films. However, failure at the Cu/Gr interface is observed at a larger indentation depth of 500 nm indicated by the plateau in Fig. 3.3. This suggests that for an indentation depth of 300 nm used in our work, a no-slip condition exists at the Cu/Gr interface.

Summary of the mechanical properties measured or calculated from the nanoindentation data is presented in table 3.1. The values shown in table 3.1 for Cu-Cu and Cu-Gr-Cu represent the composite's effective behavior as a whole. The nanoindentation hardness and Young's modulus are calculated as per the Oliver-Pharr method [43]. The hardness H of the nanolaminate is determined using the equation below:

$$H = \frac{P_{max}}{A} \tag{3.1}$$

where A is the projected contact area at $P_{max}$ i.e., the maximum applied load. The effective modulus $E_{eff}$ is determined from the reduced modulus $E_r$ given by:

$$E_r = \frac{S}{2\beta}\sqrt{\frac{\pi}{A}} \tag{3.2}$$

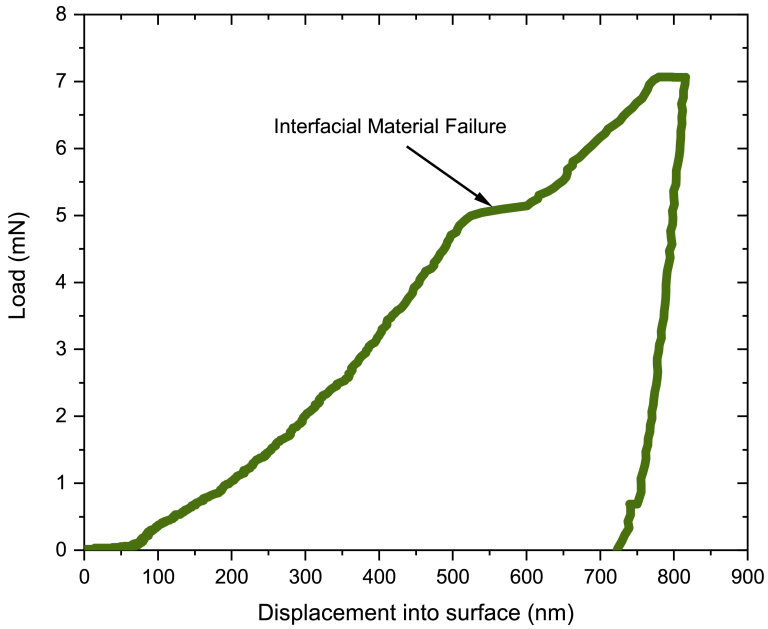


Figure 3.3: Representative load-displacement curve for nanoindentation on Cu-Gr-Cu nanolaminate structure. The plateau region, indicative of material failure at the Cu/Gr interface, occurs at indentation depth of 500 nm.

where $\beta$ is a constant that depends only on the geometry of the indenter. For a Berkovich tip $\beta = 1.034$. $S = dP/dh$ is the slope of the initial portion of the unloading curve. The effective Young's modulus E is then calculated using expression :

$$\frac{1}{E_r} = \frac{1-\nu^2}{E} + \frac{1-\nu_i^2}{E_i} \tag{3.3}$$

where $\nu$ is the Poisson's ratio of Cu, $\nu_i$ and $E_i$ are the Poisson's ratio and the Young's Modulus of the indenter respectively.

It is compelling to note that the addition of a single atomic layer of graphene increases the effective Young's modulus of the composite by 20% when compared to the effective Young's modulus of Cu-Cu nanolaminate. A 45% increase in nanoindentation hardness is observed in Cu-Gr-Cu nanolaminate when compared to Cu-Cu nanolaminate. The lamellar composites' yield strength was calculated from the correlation between yield strength and nanoindentation hardness established in section 2.3. A 35% increase in yield strength is observed in Cu-Gr-Cu nanolaminate compared to Cu-Cu nanolaminate.

| Parameters | Cu Substrate | Cu-Cu | Cu-Gr-Cu |
|---|---|---|---|
| Number of Indents | 15 | 15 | 15 |
| Peak Load (mN) | 2.0 ± 0.070 | 2.6 ± 0.090 | 3.0 ± 0.080 |
| Std. Dev of Peak Load (mN) | 0.14 | 0.16 | 0.16 |
| Young's modulus (GPa) | 110 ± 0.80 | 110 ± 2.4 | 130 ± 5.2 |
| Std. Dev of Young's modulus (Gpa) | 1.4 | 4.3 | 9.5 |
| Nanoindentation Hardness (GPa) | 0.60 ± 0.0050 | 0.92 ± 0.030 | 1.3 ± 0.040 |
| Std. Dev of Nanoindentation Hardness (Gpa) | 0.010 | 0.060 | 0.070 |
| Yield Strength (MPa) | 160 | 240 | 320 |
| Flow Strength at 8% strain (GPa) | 0.22 | 0.34 | 0.50 |

Table 3.1: Summary of the Mechanical Properties Measured and Calculated from the Nanoindentation Experiment. The values in the table have been rounded to 2 significant figures.

Flow strength is another essential mechanical property that quantifies the strength of a material. For Berkovich tip, the flow strength $\sigma_{\mathrm{f}}$ at 8% plastic strain can be calculated from nanoindentation hardness (H) using the below equation:

$$H = K \cdot \sigma_{\mathrm{f}}$$

where $K$ is Tabor's Constraint and is equal to 2.7.

The effective flow strength at 8% plastic strain for Cu-Gr-Cu is 0.5 GPa, a 47% increase compared to the effective flow strength of Cu-Cu nanolaminate. For, Cu-Gr-Cu nanolaminate, the flow strength at 8% plastic strain is as high as 12.4% of the theoretical shear strength of Cu as given by $G/10 = 4.0\,\mathrm{GPa}$, where G is the shear modulus. Thus, passivating the interface between the Cu substrate and the Cu film with a single layer graphene enhances the load-bearing capacity of

Cu-nanolaminate.

These results suggest that graphene restricts the dislocation motion across the Cu/Gr interface and thus accumulating plastic deformation within the Cu film. This behavior is consistent with previous studies on metal nanolayered composites that demonstrate a Hall-Petch like behavior at a length scale greater than 100 nm [18, 23, 48, 49]. The strength of nanolaminates increases in accordance with the Hall-Petch relation: $\sigma_f \propto h^{-0.5}$ ( h is the layer thickness). We can thus synthesize Cu-Gr-Cu nanolaminates with smaller Cu film thickness and achieve higher flow strength than reported here.

The flow strengths calculated in our work are consistent with results from the literature. Kim et al. [24] performed nanopillar compression tests of Cu-Gr nanolayered composites with varying layer spacing (70 nm, 125 nm, and 200 nm). The flow stress at 5% plastic strain was plotted against the corresponding metal layer spacing. The slope of this plot was reported to be -0.402. If we use this slope to extrapolate the flow strength of a hypothetical Cu-Gr nanolayered composite with a layer spacing of 700 nm, we will obtain a flow strength of 0.56 GPa. This value is in close agreement with the effective flow strength of 0.5 GPa exhibited by Cu-Gr-Cu nanolaminate in our experimental work.

The strength of our Cu-Gr-Cu nanolaminate is higher than the reported strengths of nanolaminates with similar metal layer spacing. For example, the Cu/Ni multilayers with 100 nm Cu and 100 nm Ni repeat layer spacing were reported to have a strength of 0.89 GPa [22]. If we consider a hypothetical Cu-Gr-Cu nanolaminate with a Cu film thickness to be 100 nm then according to Hall-Petch relation, the strength of our Cu-Gr-Cu nanolaminate will be 1.6 GPa.

Many metal nanolaminates have demonstrated enhanced strength with decreasing layer thickness. For example, nanolaminates like Au-Ni, Ag-Ni, and Cu-Nb have exhibited a peak strength of 2 GPa with a layer thickness of a couple of nanometers. The strengthening effect seen in our Cu-Gr-Cu nanolaminates is due to a single atomic layer of graphene. If we reduce the layer thickness of Ni in Au-Ni nanolaminate from 2 nm to a single atomic layer, the strength of the Au-Ni nanolaminate will drastically drop since the stress required to cross the Au/Ni interface will decrease signifi-

cantly. Thus, the strengthening effect of the atomic Ni layer is expected to be significantly lower than our Cu-Gr-Cu nanolaminates.

Moreover, we do not see rupture of graphene during indentation. We confirm this through a high-resolution cross-sectional TEM image (Fig. 3.4) of Cu-Gr-Cu nanolaminate with 100 nm Cu film deposited over monolayer graphene. The Cu-Gr-Cu interface shows the presence of mostly single-layer graphene with few double layers. Thus, the high intrinsic mechanical strength of graphene and its excellent adhesion to copper prevents the rupture and delamination of graphene even at extreme deformation.

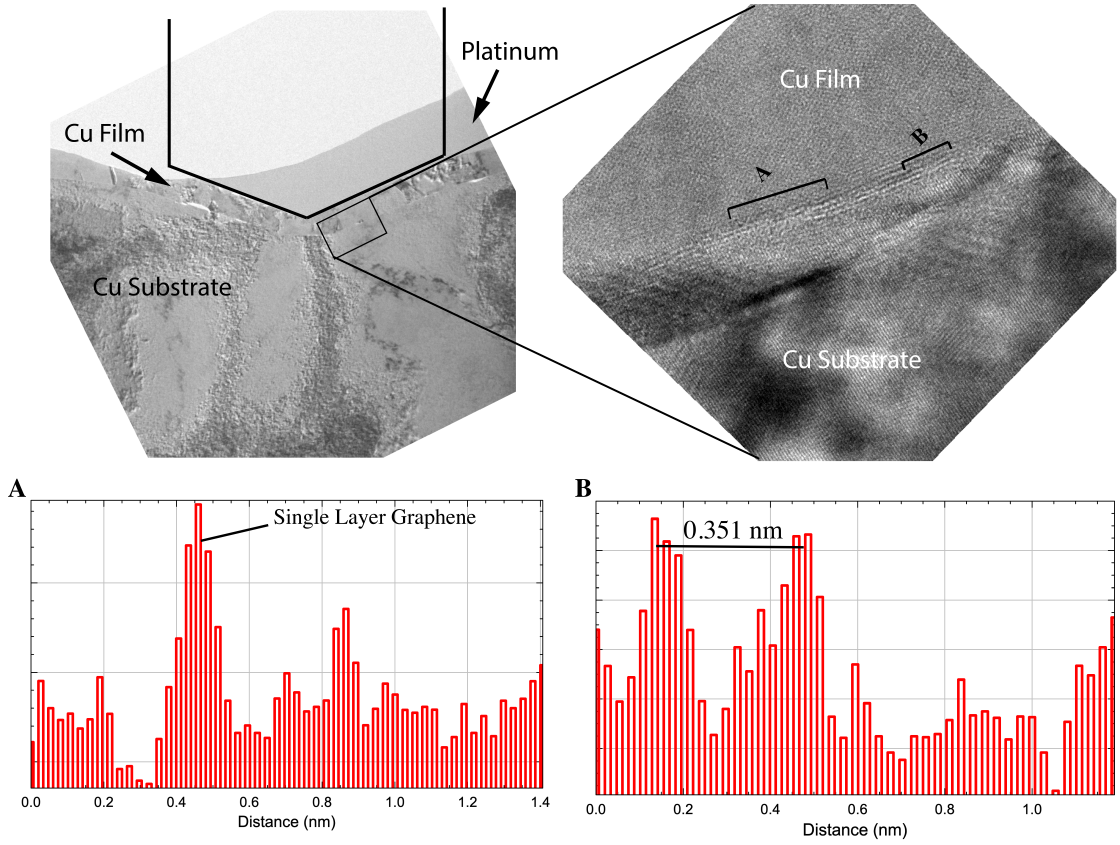


Figure 3.4: TEM cross-sectional image of Cu/Gr interface after indentation showing presence of mostly single layer graphene and few bilayer patches.

## 3.3 Analysis of Experimental Results

### 3.3.1 Governing Equations

In this section, governing equations used to analyze the behavior of our Cu/Gr nanolaminates are reviewed. We adopt the summation convention. Let $\sigma_{ij}$ denote the Cauchy stress distribution within a deformed solid, $a_i$ denote the acceleration of a material particle in a deformed solid, and $b_i$ denote the body force per unit volume acting on the solid. The equilibrium equation can be written as:

$$\sigma_{ij,j} + \rho b_j = \rho a_j \tag{3.4}$$

where, $\rho$ is the mass density of the solid. The notation $(, j)$ represents. $d/dx_j$.

The indentation into the Cu nanolaminate is considered quasi-static, and the material is not subjected to body forces. Hence, the above equation reduces to:

$$\sigma_{ij,j} = 0. \tag{3.5}$$

Finite deformation kinematics are employed. The total strain rate $\dot{\varepsilon}_{ij}$ is the symmetric part of the spatial gradient of the displacement rate $\dot{u}_i$, such that

$$\dot{\varepsilon}_{ij} = (\dot{u}_{i,j} + \dot{u}_{j,i} + \dot{u}_{k,i}\dot{u}_{k,j})/2. \tag{3.6}$$

The dot on top of a variable represents the time derivative of a variable.

In flow plasticity theories, it is assumed that the total strain in a body can be decomposed into an elastic part ($\dot{\varepsilon}^e$) and a plastic part ($\dot{\varepsilon}^p$). The elastic part of the strain can be computed from a linear elastic constitutive model. The plastic strain is determined from the plastic flow rule and a strain hardening model. A plastic flow rule determines the relationship between stress and plastic strain under multi-axial loading, while a strain hardening model controls how resistance to plastic

flow increases with plastic straining.

$$\dot{\varepsilon}_{ij} = \dot{\varepsilon}^e_{ij} + \dot{\varepsilon}^p_{ij}. \tag{3.7}$$

Regarding the constitutive relationship, the elastic part of the strain rate is related to stress rate using the linear elastic equation,

$$\dot{\sigma}_{ij} = C_{ijkl}\dot{\varepsilon}^e_{ij} \tag{3.8}$$

where $C_{ijkl}$ is the forth order elastic stiffness tensor.

An yield criterion is required to determine when the material starts deforming plastically. Assuming plastic deformation occurs at constant volume (i.e, $\varepsilon^p_{11} = 0$), we use Von-Mises yield criterion (Eqn. 3.9) to determine the yield point.

$$f(\sigma_{ij}, \bar{\varepsilon}^p) = \sqrt{\frac{3}{2}S_{ij}S_{ij}} - \sigma_y(\bar{\varepsilon}^p) = 0. \tag{3.9}$$

In the above equation $\sigma_y(\bar{\varepsilon}^p)$ is the yield stress determined from the experiments. Since the yield stress may increase during plastic straining, $\sigma_y(\bar{\varepsilon}^p)$ is written as a function of total plastic strain $\bar{\varepsilon}^p$. The total plastic strain for isotropic hardening is given by [50]

$$\bar{\varepsilon}^p = \int_0^t \sqrt{\frac{2}{3}\dot{\varepsilon}^p_{ij}\dot{\varepsilon}^p_{ij}}. \tag{3.10}$$

$S_{ij}$ is the deviatoric stress tensor and is given by

$$S_{ij} = \sigma_{ij} - \frac{1}{3}\sigma_{kk}\delta_{ij}.$$

To complete the plastic constitutive relations, the plastic strains induced by stressing the material beyond the yield point are predicted by the plastic flow rule,

$$d\varepsilon^p_{ij} = d\bar{\varepsilon}^p \frac{3}{2}\frac{S_{ij}}{\sigma_y} \tag{3.11}$$

where $d\varepsilon^p_{ij}$ and $d\bar{\varepsilon}^p$ are incremental plastic strain and incremental total plastic strain.

Finally, to model elastic unloading, the following unloading condition can be used [50],

$$S_{ij} d\sigma_{ij} < 0 \tag{3.12}$$

where $d\sigma_{ij}$ is the incremental stress and is calculated at every time increment during the analysis.

Since indentation generates large deformations in the material below and around the indenter, non-linear geometric effects become significant. Hence, non-linear kinematics were used during the loading and unloading step.

### 3.3.2 Problem Formulation

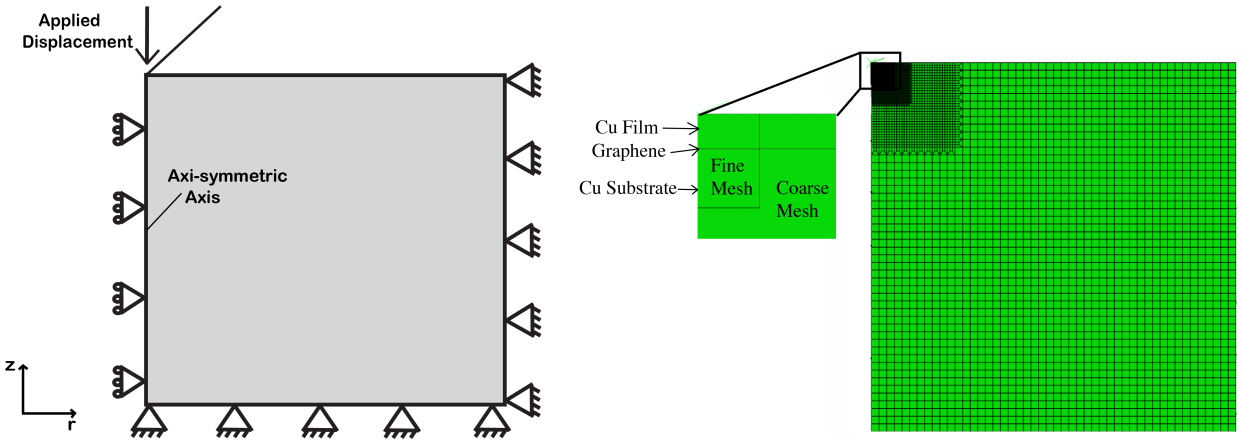


Figure 3.5: Finite element simulations of experiments, (a) schematic of the axi-symmetric Indentation of a Semi-Infinite Elastoplastic Material, (b) overall mesh with rigid indenter showing boundary conditions. Note: r here is the radial direction of the axi-symmetric domain.

A numerical study of graphene's role in Cu nanolaminates was performed using the commercial finite element code ABAQUS [51]. The simulations were performed at a constant indentation rate to a prescribed depth, followed by a withdrawal of the indenter tip. The Berkovich tip is modeled as an analytical rigid surface shaped like a cone with a half apex angle of 70.3° and a tip radius of 50 nm so that the ratio of cross-sectional area to depth is the same as the Berkovich indenter [43, 52].

The present indentation problem can be approximated as an axisymmetric (2-dimensional)

model due to symmetries of both geometry and loading conditions. The indentation into the Cu nanolaminate is considered adiabatic, and the material is not subjected to body forces. The mesh domain size is $33.6 \times 33.6\,\mu m^2$ and the indentation depth is 300 nm. Thus the extent of the substrate is about 1000 times the indentation depth. The simplified domain in Fig. 3.5(a) shows a rigid, conical indenter being pressed into the surface of what is essentially a semi-infinite material. The vertical and radial displacement at the bottom and the right edge are zero, while the left edge has zero displacements in the radial direction. The coefficient of friction between the contacting surface is set to 1.

The finite element Cu-Gr-Cu mesh shown in Fig. 3.5(b) has 365651 nodes with axisymmetric elements. The plastic zone under the indent has a higher mesh density and is meshed with eight-node bi-quadratic elements with reduced integration and hybrid with linear pressure (CAX8RH). The rest of the region is meshed with four-node bi-linear elements with reduced integration, hybrid with linear pressure (CAX4RH), and enhanced hourglass control. The hourglass stiffness for the coarse mesh region was set to 0.6% of the elastic shear modulus of copper. The plastic zone was meshed using eight-node bi-quadratic reduced integration elements instead of four-node bi-linear elements with reduced integration to avoid volumetric locking.

Graphene is modeled with two-node linear membrane axisymmetric elements. In ABAQUS, membrane elements account for contributions to the elastic strain energy density from in-plane strains but neglect those from bending strains. Thus, while modeling graphene, we have assumed that the out-of-plane bending stiffness is zero despite graphene having non-zero bending stiffness [18]. This assumption is valid for deformation states for which out-of-plane rotations occur as long as the elastic strain energy induced by the bending deformation is much less than the elastic strain energy induced by the in-plane deformation as it is with nanoindentation. Since graphene is monoatomically thin, it is considered to be a two-dimensional material with an indeterminate thickness. However, the finite element formulation requires membrane elements to have a prescribed effective thickness, which we have arbitrarily chosen to be $t = 0.335$ nm which is the interlayer spacing of the basal planes of graphite [53]. In our experiments, we observed a no-slip interfacial

condition between graphene and copper. In our numerical study, the no-slip interfacial condition is modeled by tying the nodes at the bottom of the film surface to the graphene nodes, which are then tied to nodes at the top substrate surface.

| Composite Type | | Young's Modulus (GPa) | Poisson's Ratio | Yield Strength (MPa) | Work Hardening (MPa) | Peak Load (mN) |
|---|---|---|---|---|---|---|
| Cu-Cu | Film | 107.8 | 0.343 | 600 | n/a | 2.6 |
| | Substrate | 107.8 | 0.343 | 160 | n/a | |
| Cu-Gr-Cu | Film | 107.8 | 0.343 | 600 | n/a | 2.7 |
| | Substrate | 107.8 | 0.343 | 160 | n/a | |
| | Graphene | 1000 | 0.169 | | | |
| Cu-Gr-Cu-Final | Film | 107.8 | 0.343 | 600 | 900 | 3.0 |
| | Substrate | 107.8 | 0.343 | 160 | n/a | |
| | Graphene | 1000 | 0.169 | | | |

Table 3.2: Summary of Mechanical Properties Used in the FEA Simulations of Nanoindentation.

The Young's modulus and the yield strength of the Cu substrate used in the simulations were obtained from the nanoindentation results shown in the table. 3.2. A Poisson's ratio of 0.34 was set for copper.

Since the grain size for the Cu film lies between 300 nm and 600 nm, the yield strength of the Cu film is determined to be 600 MPa using inverse finite element analysis. In Cu-Gr-Cu nanolaminate, the material properties for film and substrate are the same as that used in Cu-Cu. The presence of graphene slightly increases the strength (peak load) but not enough to match the experiment peak load of 3.0 mN.

The study by Nicola et al. [23] on plastic deformation of thin films shows that having a passivation layer (in our work, graphene is the passivation layer) on one side of the thin film dramatically increases the strength of film with high work-hardening observed as the dislocations remain inside the film due to being pinned at the interface between the film and the passivation layer. Similarly, strain hardening was also observed while compressing metal-graphene nanopillars [24], indicating the dislocation propagation being effectively blocked by graphene. Hence, to accurately model the

plastic hardening of Cu-Gr-Cu in our numerical study, the film is assumed to harden linearly to 900 MPa at a 0.1 strain (see material properties of Cu-Gr-Cu-Final).

The 2D Young's Modulus of graphene is $348\,\mathrm{N\,m^{-1}}$, which upon normalizing by $t = 0.335\,\mathrm{nm}$ yields an effective 3D Young's modulus of 1 TPa [4]. The in-plane Poisson's ratio for graphene is 0.17 [4, 12]. The out-of-plane Poisson's ratio is taken to be zero.

Discretization errors occur from representing the governing equations and physical models as algebraic expressions in a discrete space and time domain. The temporal discreteness is manifested through the time step taken while mesh size determines the discrete spatial domain. Therefore, it is essential to examine the sensitivity of the simulation results to the magnitude of the time increments and the mesh size. Implicit analysis is unconditionally stable hence not sensitive to the size of the time increment. As the mesh is refined, the solution becomes less sensitive to the mesh size and approaches the continuum solution.

Spatial convergence were performed to ensure minimum discretization error. The analysis was rerun by refining the mesh size by 25%. The numerical study did not show any sensitivity to the mesh size.

A similar numerical study was performed on the control copper nanolaminates in the absence of graphene and work hardening in Cu film. A summary of the material properties used in both Cu-Cu and Cu-Gr-Cu nanolaminates are shown in Table 3.2.

### 3.3.3 Analysis Results

Numerical simulations were performed using ABAQUS as described in section 3.3.2. Fig. 3.6 compares the force-displacement behavior of the simulation and experimental nanoindentation results for both Cu-Gr-Cu and Cu-Cu nanolaminates. The numerical simulations are in close agreement with the nanoindentation results at higher loads. The deviation at lower loads may be due to the idealized conical indenter tip used in the simulations.

Fig. 3.7(a) and Fig. 3.7(b) represent the equivalent plastic strain contours in the Cu-Cu and Cu-Gr-Cu nanolaminates near the indented region. Equivalent plastic strain is the total plastic

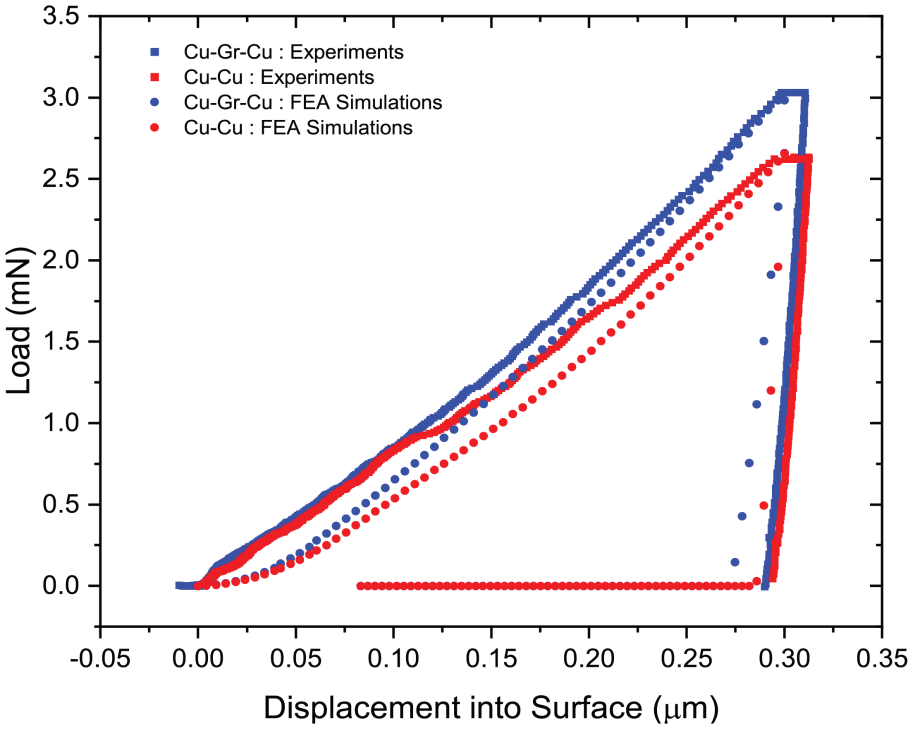


Figure 3.6: Comparison of load-displacement curves obtained from simulations to that from experiments.

strain, $\bar{\varepsilon}^p = \int_0^t \sqrt{\frac{2}{3}\dot{\varepsilon}^p_{ij}\dot{\varepsilon}^p_{ij}}$, presented in section. 3.3.1. Though the extent of plastic deformation in the substrate is similar for Cu-Cu and Cu-Gr-Cu nanolaminates, there is a significant reduction in plastic deformation in the substrate just below graphene in the Cu-Gr-Cu nanolaminate as compared to Cu-Cu nanolaminate. Thus, suggesting that graphene inhibits dislocation motion and confines plastic deformation to the Cu film when subjected to equibiaxial stress under the indenter.

Fig. 3.7(c) and Fig. 3.7(d) represent plastic energy dissipated per unit volume for Cu-Cu and Cu-Gr-Cu nanolaminates. The contours indicate a modest increase in plastic energy dissipated in the Cu film due to graphene presence. To quantify the difference observed in the contour plots, the plastic energy dissipated at the centroid of each element is exported and averaged. In the presence of graphene, the plastic energy dissipated in the Cu film is 0.077 nJ while the plastic energy dissipated in the substrate is 0.011 nJ. In comparison, the plastic energy dissipated in the Cu film and substrate for Cu-Cu nanolaminate is 0.063 nJ and 0.012 nJ respectively.

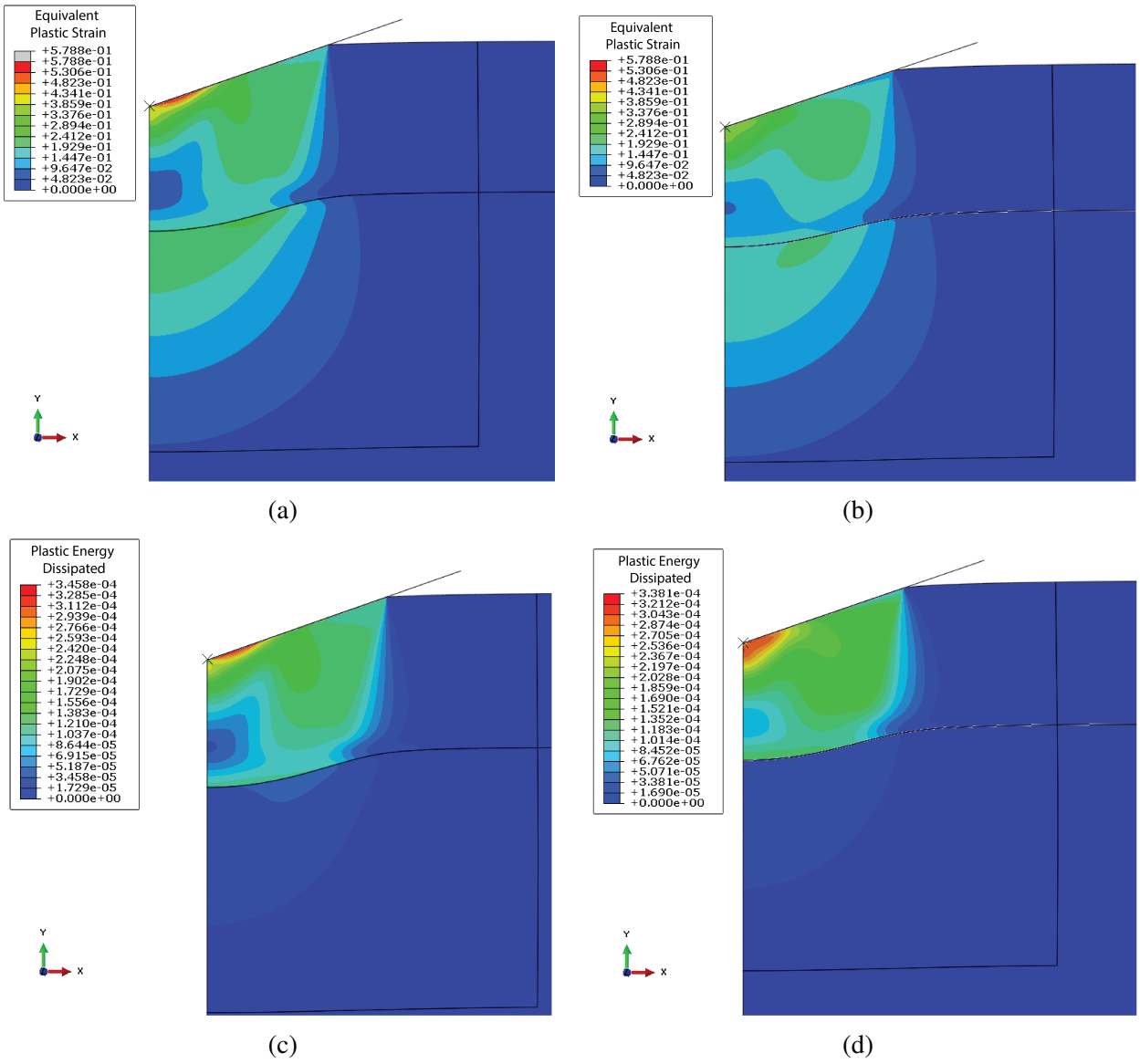


Figure 3.7: The equivalent plastic strain contours of (a) Cu-Cu and (b) Cu-Gr-Cu, plastic energy dissipated per unit volume for (c) Cu-Cu and (d) Cu-Gr-Cu. Equivalent plastic strain is the total plastic strain, $\bar{\varepsilon}^p = \int_0^t \sqrt{\frac{2}{3}\dot{\varepsilon}_{ij}^p \dot{\varepsilon}_{ij}^p}$, presented in section. 3.3.1.

The area under the load-displacement curves for the simulations as well as nanoindentation experiments are presented as bar graphs in Fig. 3.8. The red bar is the elastic energy stored in the nanolaminates, the blue bar is the energy dissipated into heat, and the green bar is work done on the composite. Both simulations and experiments show that there is more elastic energy stored in Cu-Gr-Cu nanolaminates compared to Cu-Cu nanolaminates.

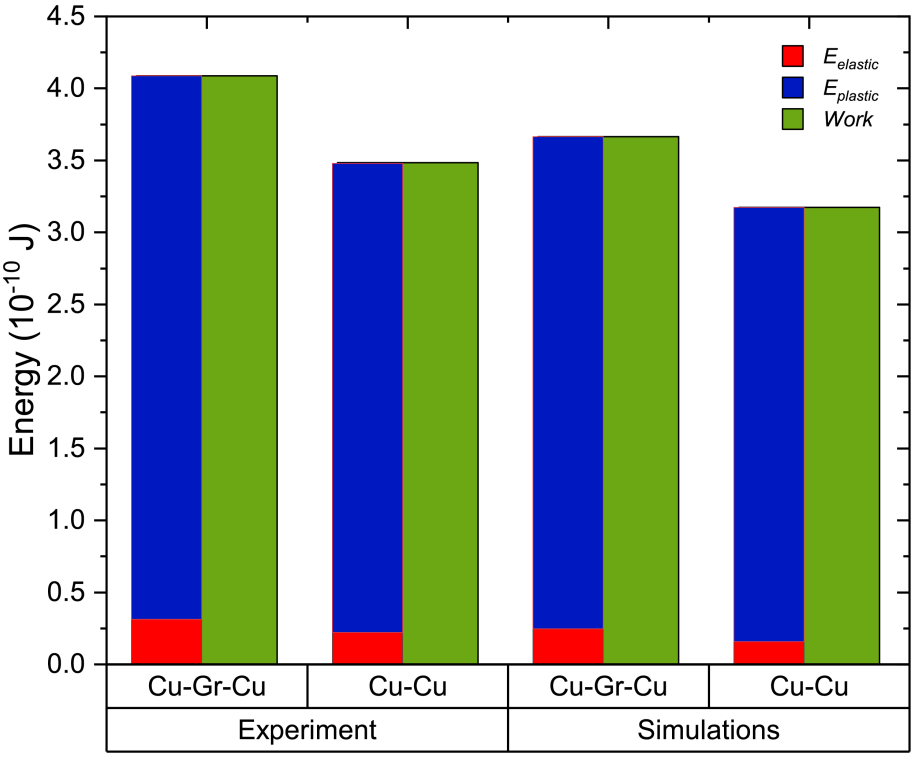


Figure 3.8: Energy dissipated during indentation.

Furthermore, the graphene element just below the indenter is strained to an equibiaxial logarithmic strain of 8.2%. The multiscale model developed [12] to characterize the in-plane nonlinear elastic behavior of graphene, suggests that at 8.2% strain, linear elastic behavior would dominate the mechanical response of graphene under equibiaxial stresses with some nonlinearity creeping in. The multiscale model also predicts that the elastic behavior of graphene becomes noticeably anisotropic when strained beyond 15%. This warrants the decision to model graphene elements in our work as linear elastic isotropic material.

The 2D strain energy density of the graphene element strained at 8.2% is 3.17 J/m$^2$. To validate this result, the elastic strain energy density is calculated using a higher-order continuum elastic

constituent model [12]. Since graphene is modeled as a linear elastic material, the elastic strain energy density is quadratic in strain and can be expressed as,

$$\Psi = 1/2 C_{ijkl}\eta_{ij}\eta_{kl} \tag{3.13}$$

where $\eta$ in the above equation is Lagrangian strain. Employing the Voigt notation for subscripts: 11 $\rightarrow$1, 22 $\rightarrow$2, 33 $\rightarrow$3, 23 $\rightarrow$4, 31 $\rightarrow$5, and 12 $\rightarrow$6, Eqn. 3.13 can be rewritten as,

$$\Psi = 1/2 C_{IJ}\eta_I\eta_J. \tag{3.14}$$

Since we are considering only in-plane stress and strain components while calculating the strain energy density for graphene, only components with subscripts 1,2 and 6 are considered. Upon accounting for the symmetry of the atomic lattice of graphene, we find that $C_{11} = C_{22}$, $C_{16} = C_{26} = 0$, $C_{11} = 0.5(C_{11} - C_{12})$ and considering $\eta_1 = \eta_2 = \eta$ and $\eta_6 = 0$ for equibiaxial strains, the linear elastic constitutive relation can be expressed as,

$$\Psi = (C_{11} + C_{12})\eta^2. \tag{3.15}$$

On substituting the values of linear elastic constants, $C_{11}$ and $C_{22}$, determined by Wei et al. [12], and plugging in $\eta = 0.089$ (calculated from logarithmic strain obtained from ABAQUS simulations), we obtain the elastic strain energy density of $3.32\,\mathrm{J/m^2}$. Thus, validating our numerical simulations.

In addition, the FEA simulations of indentation of circular freestanding graphene membrane demonstrate that the rupture of graphene in indentation tests occurred approximately at a strain of 0.228 [12]. In our work, with graphene strained at 0.082, we do not expect rupture of graphene during indentation. We confirm this through a high-resolution cross-sectional TEM image (Fig. 3.4) of Cu-Gr-Cu nanolaminate with 100 nm Cu film deposited over monolayer graphene. The Cu-Gr-Cu interface shows the presence of mostly single-layer graphene with few double layers. Thus, the

high intrinsic mechanical strength of graphene prevented its rupture.

In summary, we report a nanolaminate microstructure design of Cu-Gr-Cu that enhances the load-bearing capacity of the composite. The inclusion of a single layer of graphene increases the effective Young's modulus by 20% and the effective flow strength by 45%. The increase in the strength of the composite is due to graphene's ability to constrain dislocation propagation across the Cu-graphene interface. Our FEA simulations confirm the increase in plastic energy dissipated in Cu film due to the presence of graphene and the reduction in plastic deformation in the Cu substrate just below graphene.

# Chapter 4: Improved Frictional Behaviour of Cu-Gr-Cu nanolaminate

Tribological behavior plays a vital role in the performance of ultra-precision mechanical systems such as micro-electro-mechanical systems (MEMS) that consist of moving parts. The effectiveness of components such as switches, gears, and actuators is strongly dependent on their frictional behavior, while the wear resistance determines the mechanical and commercial viability of the device. Moreover, lubricating fluids can not be employed in micro-systems to reduce friction due to surface tension effects. Therefore, to develop reliable micro-devices, the tribological properties of the components must be optimized under dry sliding conditions. Graphene's remarkable mechanical [4, 12], thermal [3], and electrical properties [1] make it an ideal candidate for a solid lubricant. In recent years graphene's ability to reduce friction between contact surfaces on the micro and nanoscale while protecting the coated surface has garnered attention [54–56].

Graphene films grown on Cu and Ni metal catalysts by chemical vapor deposition effectively reduced the frictional forces [57]. Scratch tests were also performed on graphene sheet transferred onto to $SiO_2/Si$ substrate. It was found that the tribological properties of graphene depend on the adhesion between graphene and the substrate. Higher adhesion exists when graphene is grown on a substrate (in this case Ni) when compared to graphene transferred onto $SiO_2$. Hence, the coefficient of friction was significantly lower for graphene grown on Ni when compared to graphene transferred onto $SiO_2$. However, irrespective of the substrate, the presence of graphene reduced the coefficient of friction compared to the non-coated substrate. Berman et al. [58] achieved superlubricity by using graphene in combination with crystalline diamond nanoparticles and diamond-like carbon. Simulations showed that sliding of the graphene patches around the tiny nanodiamond particles led to nanoscrolls with reduced contact areas that slide easily against the amorphous

diamond-like carbon surface.

Traditional methods of coating a metal surface to lubricate can result in the graphene layer being worn out and thus losing its beneficial effect. Instead, Zhai et al. [59] added graphene nanoplatelets (GNPs) to metal matrix $Ni_3Al$ and tested for the friction and wear behavior through a series of scratch tests. The tribological test revealed that small amounts of GNPs in the metal matrix drastically reduced the friction coefficients and wear rates. However, the addition of graphene platelets to a metal matrix leads to a non-uniform dispersion of graphene platelets and agglomeration of the graphene flakes leading to poor reliability and strength enhancement.

Alternatively, one can consider using a metal/graphene nanolayered composite that can suppress friction. In the previous chapter, we demonstrated that inserting a single layer of graphene (Gr) between a Cu film of 700 nm thickness and a Cu-substrate increased the effective Young's modulus and effective flow strength of the Cu-Gr-Cu nanolaminate by 20% and 45% respectively when compared to Cu-Cu nanolaminate. The strengthening effect was due to graphene's ability to prevent dislocation motion across the Cu/Gr interface. In this chapter, graphene's ability to constrain dislocation motion reduces the coefficient of friction in Cu-Gr-Cu nanolaminate compared to Cu-Cu nanolaminate. In the following sections, we outline the scratch test methodology and report the frictional behavior of Cu-Gr-Cu nanolaminate. Details of the FEA simulations of scratch test on the lamellar composites are presented in the finite element modeling section, along with the numerical results.

## 4.1 Nanolaminate Fabrication

A high purity, 1 mm thick, copper substrate (Alfa Aesar, 99.9999%) is electropolished using Rotating Disk Electrode (RDE) polishing to remove surface contamination and reduce the surface roughness to less than 2 nm. The Cu substrate is mounted on a rotating disk, which acts as an anode and is dipped into an 85% (by volume) phosphoric acid electrolyte. A platinum mesh (Alfa Aesar) is used as a cathode, while a Gamry Calomel (Ag/AgCl) electrode is used as a reference. The Cu substrate is electropolished to remove 110 µm of material thickness and reduce the surface

roughness to less than 2 nm (Fig. 4.1(b).

(a) (b) (c)

Figure 4.1: Picture of Cu substrate (a) before electropolishing and (b) after electropolishing, (c) a scanning electron microscopy image of graphene grown on the Cu substrate. The dark contrast spots are nucleation spots and also bi-layer graphene patches. Scale is 3 µm.

A continuous single atomic layer of graphene is then grown on the substrate via chemical vapor deposition (CVD). The electropolished copper substrate is first annealed at 1000 °C for 2 hrs in a gas mixture of $H_2$ (5 sccm) and Ar (50 sccm) at 1 Torr. Graphene growth takes place at 1000 °C for 30 min using methane as the precursor gas. During the growth stage, methane and hydrogen flow at 5 sccm and 10 sccm, respectively, while maintaining a pressure of 0.3 Torr. Raman spectroscopy confirmed that the resulting graphene is primarily a single atomic layer with a good G/2D ratio of 1/3 [12, 36]. Fig. 4.1(c) is an SEM image of CVD graphene grown on our Cu substrate.

To ensure we capture the influence of graphene on the frictional behavior of the composite, a 400 nm Cu film is deposited onto single-layer graphene via physical vapor deposition (PVD) at room temperature to synthesize a Cu-Gr-Cu nanolaminate.

For comparison, a control — Cu-Cu nanolaminate — sample (not shown) was synthesized according to the procedure described above; however, methane did not flow through the furnace during the graphene growth stage, ensuring both nanolaminate structures were subjected to the same thermal cycle. Another modification while fabricating the control sample was to deposit the Cu film at 200 °C on the Cu-Substrate to ensure similarity in the grain size distribution of the Cu film in both Cu-Gr-Cu and Cu-Cu nanolaminate structure.

Grain size and grain orientation were measured using Electron Backscatter Diffraction on SEM

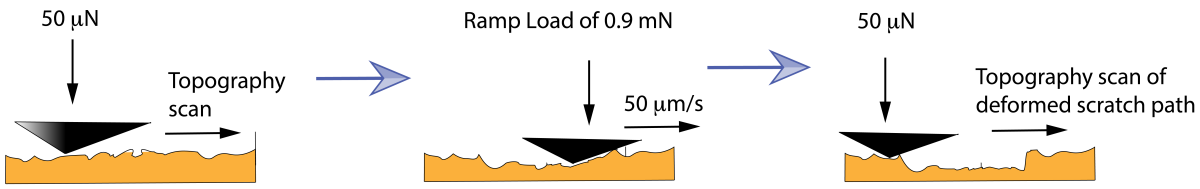


Figure 4.2: Schematic representing the scratch test methodology using a Berkovich tip.

and precession electron diffraction (PED) on TEM. The grain size distribution indicated that the grain size of the Cu film ranges between 200 nm to 600 nm for both Cu-Cu and Cu-Gr-Cu nanolaminate structures. The reader can refer to chapter 2 for further details on the fabrication process and the grain size distribution charts.

## 4.2 Frictional Characterization

The frictional behavior of Cu nanolaminates was tested using a G200 nanoindenter (KLA Corporation, Milpitas, CA, USA).

A schematic of a typical scratch test is shown in Fig. 4.2. The Berkovich tip first performed a surface topography scan over the scratch length of 500 μm at a relatively low normal load of 50 μN. The tip then returned to the origin and was ramp loaded to the prescribed maximum normal load while the sample was translated at a scratch velocity of 50 μm/s. The system continuously measured the lateral forces acting on the Berkovich tip during the scratch. It is important to note that the Berkovich tip is pyramidal in shape (see Fig. 4.3), hence while using a Berkovich tip, one can perform a scratch test either using the edge orientation or the face orientation (Fig. 4.3). In this work, all the scratch tests were performed using the edge-oriented Berkovich tip.

The maximum normal load for the scratch test was determined through a series of depth controlled indentations performed for depths ranging from 60 nm to 180 nm. The corresponding load-displacement curves shown in Fig. 4.4 indicate that the laminate exhibited an increased tendency of interfacial material failure (plateau region) for normal loads greater than 1 mN. Hence, the maximum ramp load was set to 1 mN. The scratch test was performed 11 times on the Cu-Gr-

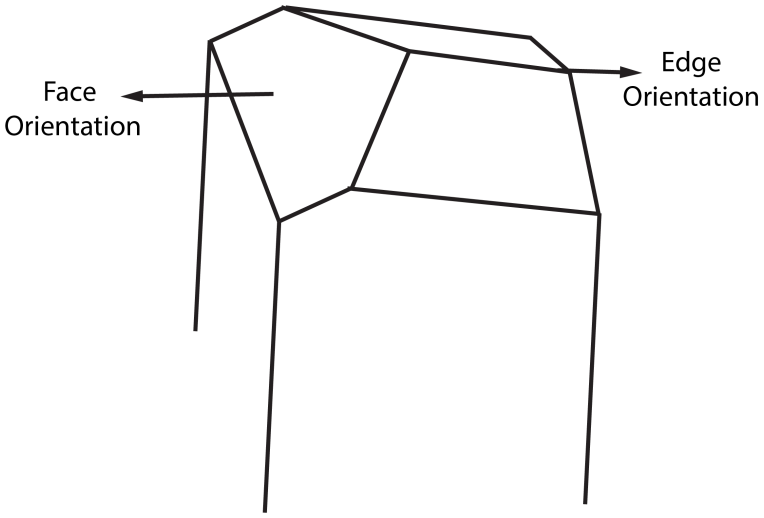


Figure 4.3: Schematic of a Berkovich tip.

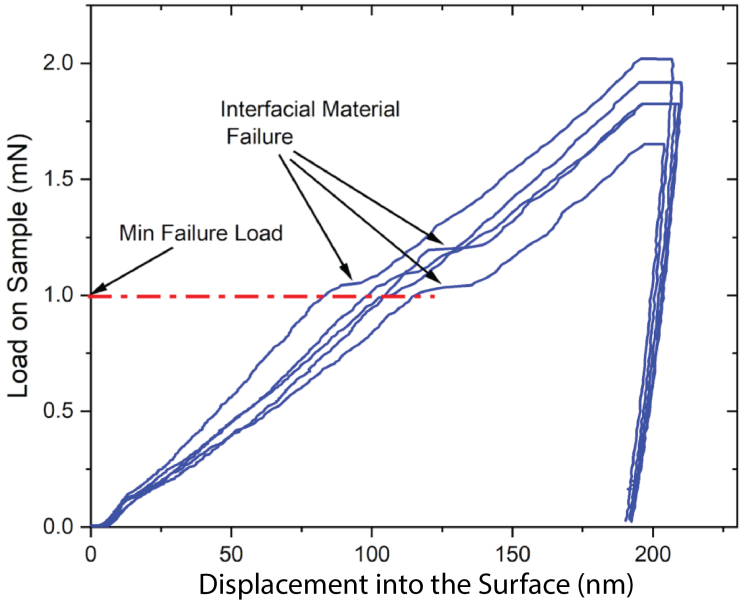


Figure 4.4: Load-displacement curves of Cu-Gr-Cu nanolaminate exhibiting interfacial material failure for normal loads greater than 1 mN. Max ramp load of 1 mN was chosen for the scratch test.

Cu nanolaminate and 12 times on the Cu-Cu nanolaminate. Fig. 4.5(a) is a scanning electron microscopy image of the scratch performed on our Cu nanolaminates.

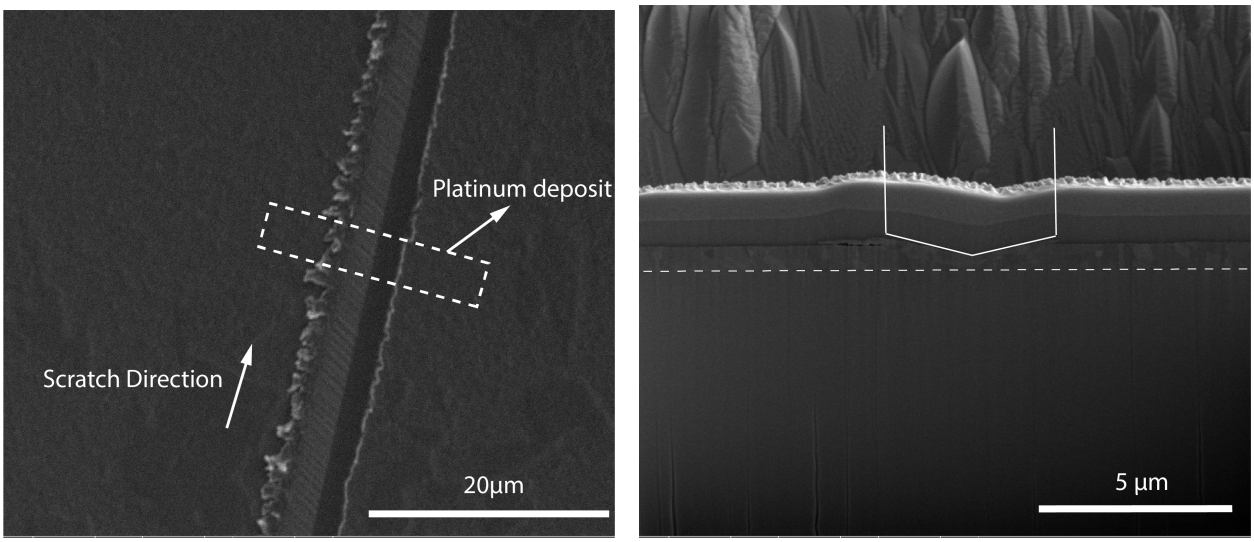


(a) (b)

Figure 4.5: (a) An SEM image of the scratch on our Cu nanolaminates. The dotted rectangle depicts the position of the Pt deposit on the scratch. (b) Cross-sectional SEM image of the scratch. The dotted line depicts graphene sandwiched between the Cu film and the Cu substrate. The outline of the indenter is also shown.

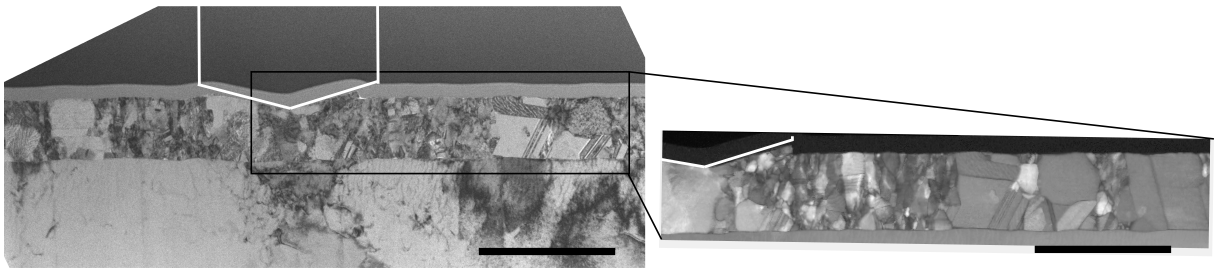

Figure 4.6: Cross-sectional TEM image of Cu-Gr-Cu nanolaminate perpendicular to the scratch. Scale is 2 µm. Inset shows the extent of recrystallization due to severe plastic deformation near the scratch compared to regions away from the scratch. Scale is 2 µm.

Fig. 4.6 is bright field TEM cross-sectional image of Cu-Gr-Cu nanolaminate perpendicular to the scratch. The cross-sectional specimens for the TEM were fabricated by cutting across the scratch path using Focused Ion Beam Fig. 4.5(b). In the TEM image, the Cu substrate is a single crystal for the length scale shown here, the straight line at the interface of the Cu film and the

Cu substrate denotes a single atomically thin layer of graphene. The Cu film deposited atop the graphene is polycrystalline and columnar. A micrometer thick platinum film was deposited on the Cu film while fabricating the TEM sample using Focused-Ion Beam (FIB) to protect the Cu film from damage due to ion bombardment during the milling and thinning process of TEM sample preparation. The protective platinum layer was deposited using an ion beam with energy of 30 kV. The scratch width measured from the TEM image is approximately 2 μm.

Transmission Electron Microscopy was used to investigate the influence of graphene on the frictional behavior of copper laminates. Scratch tests induce plastic deformation (dislocation) in the microstructure; hence, in addition to the conventional bright field imaging, a weak beam dark field (WBDF) technique was used to obtain high resolution images of dislocations. The WBDF technique involved orienting the sample with respect to the electron beam such that the Bragg condition was only met for one reflection in the reciprocal lattice or one diffraction vector $\mathbf{g_{022}}$ and no other reflections are excited. The weak beam image was then formed by tilting the beam using the DF beam deflecting coils so that the reflection $\mathbf{g_{022}}$ is brought to the optic axis, thus achieving the required $\mathbf{g_{022}}(\mathbf{3g_{022}})$ condition. By doing so, we make $\mathbf{s}_{\mathbf{g_{022}}}$ (excitation error: it is the distance measured in reciprocal space that determines how far the diffraction spot is from satisfying Bragg's condition) large, and if a defect is present, the diffracting planes are bent locally back into the Bragg-diffracting orientation to give more intensity in the DF image. This means that the dislocation is imaged as a bright line on a dark background under dark field conditions. The reader may refer to appendix A for a more detailed understanding of WBDF imaging. Since we would like to investigate the influence of graphene, a region 500 nm below the Cu/Cu and Cu/Graphene interface was considered sufficient. All the TEM imaging was carried out in FEI Talos S/TEM instrument operating at 200 kV.

Extreme plastic deformation in the Cu film due to scratching can lead to the recrystallization of grains in the Cu film. In Fig. 4.6 grains closer to the scratch are smaller in size compared to the grains away from scratch, thus confirming that a certain degree of recrystallization occurs in the Cu film due to scratching. Recently developed TEM orientation mapping technique based on

a collection of precession electron diffraction (PED) patterns, commercially known as ASTAR$^{TM}$ [41] can be used to determine the degree of recrystallization that occurs due to scratching in the Cu film for Cu-Cu and Cu-Gr-Cu nanolaminates The grain orientation maps were collected on an FEI Talos S/TEM by scanning the electron beam with 12 nm step size at an accelerating voltage of 200 kV.

### 4.2.1 Experimental Results

Fig. 4.7(a) shows the typical normal-load versus scratch distance curve for Cu-Cu and Cu-Gr-Cu nanolaminates. The measured lateral force and the frictional coefficient for the lamellar composites are shown in Fig. 4.7(b) and Fig. 4.7(c). The lateral force measured for Cu-Gr-Cu nanolaminate is considerably lower than the lateral force measured for Cu-Cu nanolaminate. The lateral forces for the two nanolaminates are similar up to a scratch length of 50 nm (first 10% scratch length), confirming similarity in surface roughness for both the samples. Since the grain size of the Cu film is the same in both nanolaminate structures, the difference in the lateral force is entirely due to the presence of a single atomic layer of graphene.

The coefficient of friction (CoF) was calculated by taking the ratio of the measured lateral force to the normal load applied by the indenter. The mean CoF for Cu-Gr-Cu is 0.2 with a standard deviation of 0.0130, while the mean CoF for Cu-Cu is 0.3 with a standard deviation of 0.0128. A two-sample t-test was performed to establish a significant difference in the mean CoF for Cu-Cu nanolaminate and Cu-Gr-Cu nanolaminate. A p-value of $8 \times 10^{-14}$ and $10 \times 10^{-14}$ was observed with the assumption of equal variance and unequal variance, respectively. Since the p-value is much less than the significance level of 0.05, the decrease in CoF is not attributed to the random noise in the data.

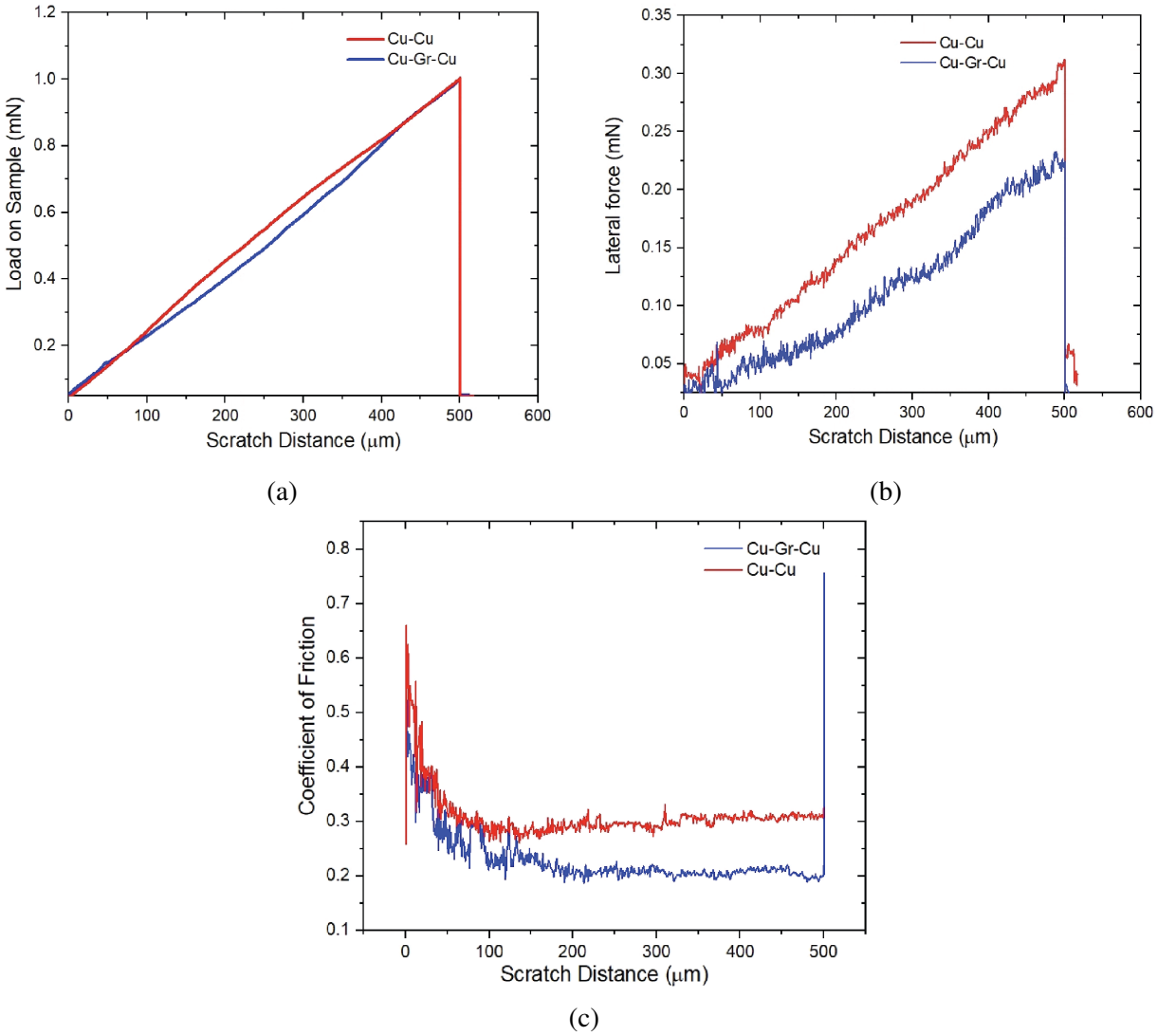


Figure 4.7: (a) Typical normal-load versus scratch distance curve, (b) measured lateral force, and (c) coefficient of friction (CoF) for Cu-Cu and Cu-Gr-Cu nanolaminates.

It is impressive to note that the inclusion of a single atomic layer of graphene can decrease the COF of the composite by 33% compared to Cu-Cu nanolaminate. The frictional work done in a scratch test depends on the coefficient of friction ($\mu$), the normal load applied ($F_N$), and the scratch length ($d$) ($W_f = \mu \cdot F_N \cdot d$). Since the scratch length and the normal load applied are the same for Cu-Cu and Cu-Gr-Cu nanolaminates, a decrease in friction coefficient implies lower frictional work done/energy dissipated during scratch in Cu-Gr-Cu nanolaminate. A large part of this frictional work done is attributed to plastic deformation. Hence, a lower measured

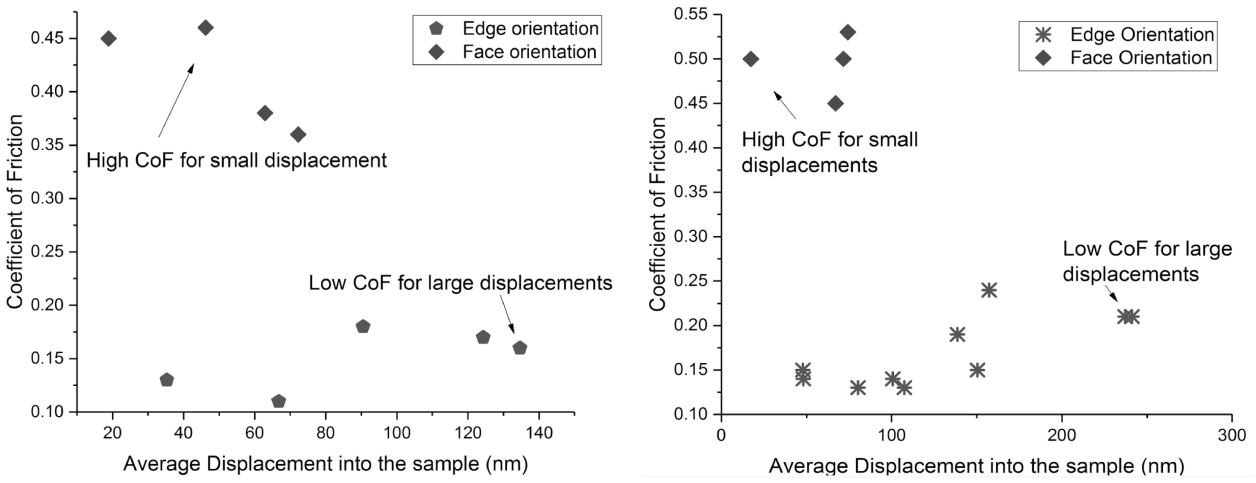


(a) (b)

Figure 4.8: Effect of Berkovich tip orientation on CoF,(a) scratch test performed on 300 nm Cu film thickness, (b) scratch test performed on 400 nm Cu film thickness. Face-oriented scratch has higher CoF compared to edge-oriented scratch, irrespective of layer thickness.

COF corresponds to lower energy dissipation during the scratch segment and consequently a lower degree of plastic deformation in the Cu-Gr-Cu nanolaminate.

Due to the Berkovich tip's pyramidal shape, a scratch test can be performed using either the edge orientation or the face orientation ( Fig. 4.3). Scratch tests performed on Cu-Gr-Cu nanolaminate using the face orientation have a higher CoF compared to the edge orientation for similar average displacement into the surface. Fig. 4.8 compares the CoF calculated for Cu-Gr-Cu nanolaminate when scratched using face-oriented Berkovich tip to when the nanolaminate was scratched using edge-oriented Berkovich tip. The comparison was performed for two Cu-Gr-Cu nanolaminate structures, one with the Cu film thickness as 300 nm and the other with Cu film thickness as 400 nm. Face-oriented scratch test on Cu-Gr-Cu nanolaminate results in a CoF of 0.4, same as that for Cu-Cu nanolaminate. Hence, suggesting that the plastic deformation formed during scratching is too large for graphene to constrain it within the film effectively. Therefore, we postulate that the Cu/Gr interface eventually gives away and allows plastic deformation to move to the substrate.

Weak Beak BF images of the deformed region (under the scratch) and the undeformed region (away from the scratch) for Cu-Gr-Cu nanolaminate are shown in Fig.4.9. The dark lines present in the copper substrate in both the images are dislocation lines imaged on a bright background.

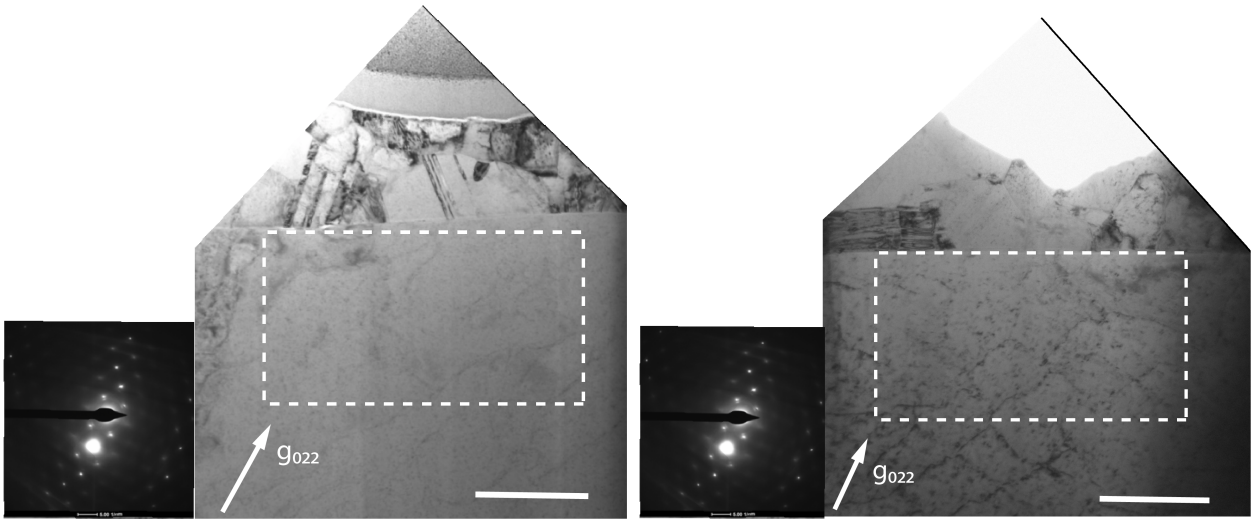


(a) (b)

Figure 4.9: Weak Beak BF images of the (a) deformed region (under the scratch), and (b) the undeformed region (away from the scratch) for Cu-Gr-Cu nanolaminate. Scale is 500 nm. Note: in (b) the top portion of the Cu film was lost during the TEM sample prep using Focused Ion Beam.

Interestingly, the density of dislocations in the Cu substrate is of the same order - $10^{13}$ $m^{-2}$ for both the deformed and the undeformed regions (see the appendix section on how the dislocation density was calculated). Thus, suggesting that graphene blocks dislocations from exiting the Cu film.

Severe plastic deformation in polycrystalline metals can lead to the recrystallization of grains. In Fig. 4.6 grains closer to the scratch are smaller in size compared to the grains away from scratch, thus confirming that a certain degree of recrystallization occurs in the Cu film due to scratching. A TEM orientation mapping technique commercially known as ASTAR$^{TM}$ [41] was used to measure the grain size and determine the extent of recrystallization in both Cu-Cu and Cu-Gr-Cu nanolaminates. The Inverse Pole Figure (IPF) maps for Cu-Cu, and Cu-Gr-Cu nanolaminate structures are shown in Fig. 4.10(a) and Fig. 4.10(b), respectively. The grain size distributions are shown in Fig. 4.10(c) and Fig. 4.10(d). Most of the recrystallized grains lie under the scratch and have a grain size of approximately 200 nm or less.

Area fraction is used as the metric to compare the extent of recrystallization in Cu-Cu and Cu-Gr-Cu nanolaminate. The sample size for grain orientation imaging was 3 for both Cu-Cu and

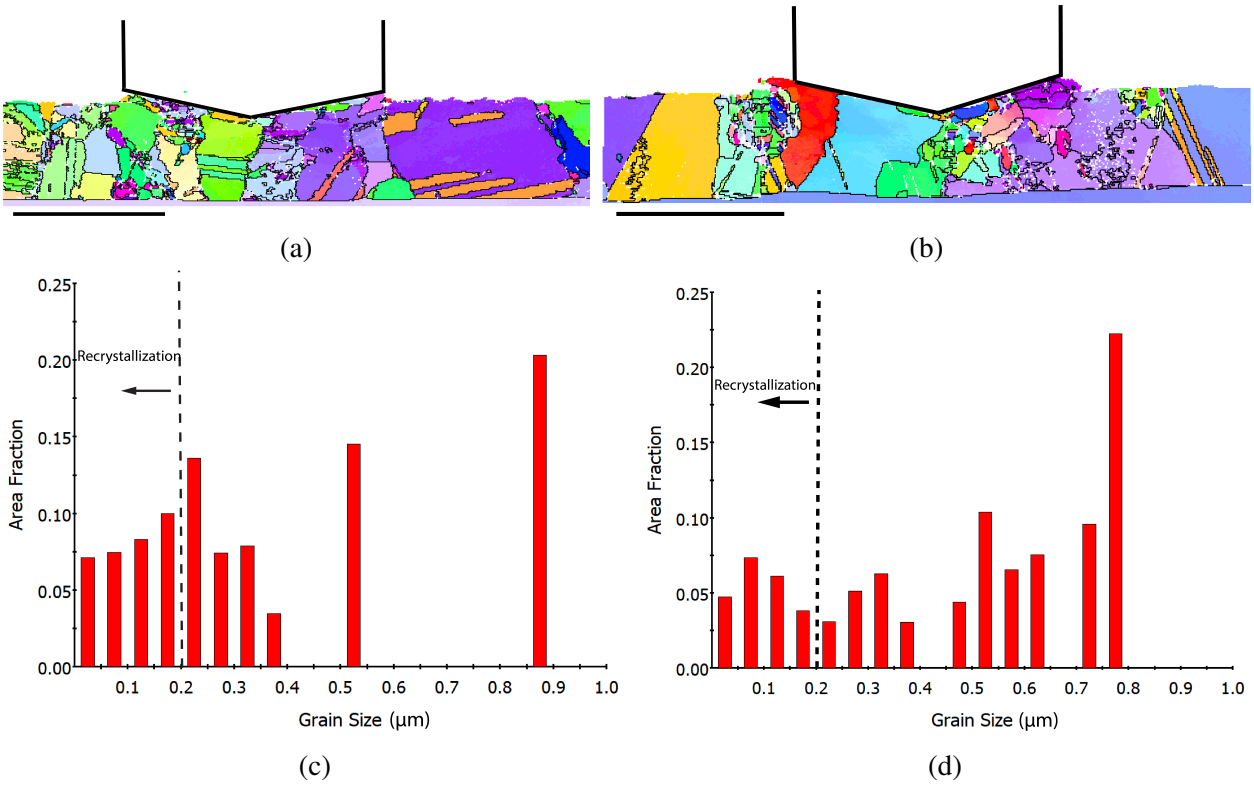


Figure 4.10: Determining extent of recrystallization in the Cu film using TEM Precession Electron Diffraction grain size analysis: (a) IPF map for Cu-Cu, (b) IPF map for Cu-Gr-Cu, (c) grain size distribution for Cu-Cu, (d) grain size distribution for Cu-Gr-Cu. Grains with size less than 200 nm are considered to be recrystallized due to severe plastic deformation. Scale is 500 nm

Cu-Gr-Cu nanolaminate. The mean area fraction of recrystallized grains is 0.25108 and 0.18903 for Cu-Gr-Cu and Cu-Cu nanolaminate, respectively. A two-sample t-test was performed to establish a significant difference in the mean area fraction for Cu-Cu nanolaminate and Cu-Gr-Cu nanolaminate. A p-value of 0.3 and 0.35 was observed with the assumption of equal variance and unequal variance, respectively. Since the p-value is larger than the significance level of 0.05, the difference between the two mean area fractions is not statistically significant. Thus, we could not establish the difference in the degree of recrystallization due to scratch in Cu-Cu and Cu-Gr-Cu nanolaminate. This could be due to the small sample size or choosing an inaccurate metric to measure the extent of recrystallization. A more detailed study is required to determine the deformation behavior of nanolaminates due to scratch.

FEA study described in the next section will help us further understand the frictional behavior

of Cu-Gr-Cu nanolaminate.

## 4.3 Analysis of Experimental Results

### 4.3.1 Governing Equations

In this section, governing equations used to analyze the behavior of our Cu/Gr nanolaminates are reviewed. We adopt the summation convention. Let $\sigma_{ij}$ denote the Cauchy stress distribution within a deformed solid, $a_i$ denote the acceleration of a material particle in a deformed solid, and $b_i$ denote the body force per unit volume acting on the solid. The equilibrium equation can be written as:

$$\sigma_{ij,j} + \rho b_j = \rho a_j \tag{4.1}$$

where, $\rho$ is the mass density of the solid. The notation $(, j)$ represents. $d/dx_j$.

The indentation into the Cu nanolaminate is considered quasi-static, and the material is not subjected to body forces. Hence, the above equation reduces to:

$$\sigma_{ij,j} = 0. \tag{4.2}$$

Finite deformation kinematics are employed. The total strain rate $\dot{\varepsilon}_{ij}$ is the symmetric part of the spatial gradient of the displacement rate $\dot{u}_i$, such that

$$\dot{\varepsilon}_{ij} = (\dot{u}_{i,j} + \dot{u}_{j,i} + \dot{u}_{k,i}\dot{u}_{k,j})/2. \tag{4.3}$$

The dot on top of a variable represents the time derivative of a variable.

In flow plasticity theories, it is assumed that the total strain in a body can be decomposed into an elastic part ($\dot{\varepsilon}^e$) and a plastic part ($\dot{\varepsilon}^p$). The elastic part of the strain can be computed from a linear elastic constitutive model. The plastic strain is determined from the plastic flow rule and a strain hardening model. A plastic flow rule determines the relationship between stress and plastic strain under multi-axial loading, while a strain hardening model controls how resistance to plastic

flow increases with plastic straining.

$$\dot{\varepsilon}_{ij} = \dot{\varepsilon}^e_{ij} + \dot{\varepsilon}^p_{ij}. \tag{4.4}$$

Regarding the constitutive relationship, the elastic part of the strain rate is related to stress rate using the linear elastic equation,

$$\dot{\sigma}_{ij} = C_{ijkl}\dot{\varepsilon}^e_{ij} \tag{4.5}$$

where $C_{ijkl}$ is the forth order elastic stiffness tensor.

An yield criterion is required to determine when the material starts deforming plastically. Assuming plastic deformation occurs at constant volume (i.e, $\varepsilon^p_{11} = 0$), we use Von-Mises yield criterion (Eqn. 4.6) to determine the yield point.

$$f(\sigma_{ij}, \bar{\varepsilon}^p) = \sqrt{\frac{3}{2}S_{ij}S_{ij}} - \sigma_y(\bar{\varepsilon}^p) = 0. \tag{4.6}$$

In the above equation $\sigma_y(\bar{\varepsilon}^p)$ is the yield stress determined from the experiments. Since the yield stress may increase during plastic straining, $\sigma_y(\bar{\varepsilon}^p)$ is written as a function of total plastic strain $\bar{\varepsilon}^p$. The total plastic strain for isotropic hardening is given by [50]

$$\bar{\varepsilon}^p = \int_0^t \sqrt{\frac{2}{3}\dot{\varepsilon}^p_{ij}\dot{\varepsilon}^p_{ij}}. \tag{4.7}$$

$S_{ij}$ is the deviatoric stress tensor and is given by

$$S_{ij} = \sigma_{ij} - \frac{1}{3}\sigma_{kk}\delta_{ij}. \tag{4.8}$$

To complete the plastic constitutive relations, the plastic strains induced by stressing the material beyond the yield point are predicted by the plastic flow rule,

$$d\varepsilon^p_{ij} = d\bar{\varepsilon}^p \frac{3}{2}\frac{S_{ij}}{\sigma_y} \tag{4.9}$$

where $d\varepsilon^p_{ij}$ and $d\bar{\varepsilon}^p$ are incremental plastic strain and incremental total plastic strain.

Finally, to model elastic unloading, the following unloading condition can be used [50],

$$S_{ij} d\sigma_{ij} < 0 \tag{4.10}$$

where $d\sigma_{ij}$ is the incremental stress and is calculated at every time increment during the analysis.

Since indentation generates large deformations in the material below and around the indenter, non-linear geometric effects become significant. Hence, non-linear kinematics were used during the loading and unloading step.

### 4.3.2 Explicit Analysis

The FEA study was performed with ABAQUS/Explicit solution method. The explicit solution method is a dynamic procedure initially developed to model high-speed impact events in which inertia plays a dominant role in the solution. ABAQUS/Explicit has proven to be valuable in solving quasi-static problems as well. However, specific special considerations need to be made while applying ABAQUS/Explicit to a quasi-static problem. When modeling a problem as quasi-static, the loading parameters need to be accelerated to make the analysis computationally efficient. If the loading event is too accelerated, then the quasi-static analysis evolves into a state of dynamic equilibrium. Hence, load rate scaling or mass scaling is often used to obtain a quasi-static solution that requires less CPU time. The load should be applied as a smooth step function so that the artificial kinetic energy does not oscillate and is less than 1% of the internal energy – this ensures quasi-static assumption in explicit analysis.

In a static analysis, the lowest modes of the structure dominate the response. Knowing the lowest natural frequency and, correspondingly, the period of the lowest mode, one can estimate the time required to obtain a static response. The following equations show how the stable time increment is related to the material density:

$$\Delta t = \frac{L^e}{c_d} \tag{4.11}$$

where $L^e$ is the characteristic element length and $c_d$ is the dilatational wave speed of the material.

$$c_d = \sqrt{\frac{E}{\rho}} \tag{4.12}$$

where $\rho$ is the mass density of the material. According to the above equations, artificially increasing the density of a material decreases the dilation speed $c_d$, increasing the stable time increment. Scaling the mass (artificially increasing the density) has precisely the same influence on inertial effects as artificially increasing the loading rate. Ensuring that the kinetic energy of the deforming material does not exceed a small fraction (typically 5% to 10%) of the internal energy throughout the simulation helps avoid erroneous solutions due to mass scaling and load rate scaling.

### 4.3.3 Adaptive Meshing

In many nonlinear analyses, the material in the structure undergoes large deformations. These deformations distort the finite element mesh such that the mesh cannot provide accurate numerical results or the analysis terminates for numerical reasons. Adaptive meshing is used to avoid extreme distortion of elements.

Most problems in ABAQUS use a pure Lagrangian description where the mesh moves with the material. A pure Lagrangian model makes it easy to apply boundary conditions and keep track of surfaces. However, the quality of the results quickly deteriorates as the mesh gets distorted when the material is subjected to severe plastic deformation. A simulation model can also be described using an Eulerian description where the nodes stay fixed while material flows through the mesh. It becomes harder to track surfaces in an Eulerian description, but no mesh distortion occurs as the mesh is fixed. Adaptive meshing in ABAQUS/Explicit uses the arbitrary Lagrangian-Eulerian (ALE) method combines the features of pure Lagrangian analysis and pure Eulerian analysis. The mesh motion is constrained to the material motion on surfaces on which boundary conditions are prescribed (at free boundaries), whereas, in regions of large deformation, the mesh motion and material motion are independent of each other.

When adaptive meshing is employed in an analysis, a smooth mesh is generated at regular time increments to reduce element distortion and maintain good element aspect ratios. The re-meshing frequency is kept as low as possible so that the precision of the solution is not lost while maintaining an undistorted element shape. Usually, a convergence test is done with varying mesh frequencies to ensure the accuracy of the results.

### 4.3.4 Problem Formulation

An FEA study was performed using commercial finite element code: ABAQUS [51] to analyze graphene's role in reducing friction during a scratch test. The Berkovich tip, modeled as an analytical rigid surface, is ramp loaded to the prescribed maximum load while simultaneously scratching the surface at 50 µm/s until steady-state conditions are achieved.

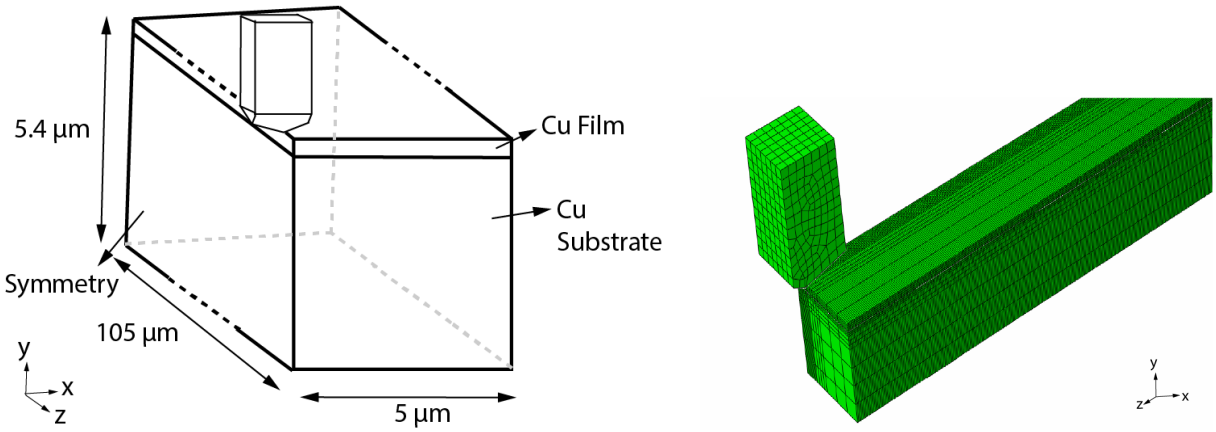


(a) (b)

Figure 4.11: Finite element simulations of friction experiments, (a) schematic of the scratch test of Cu-Gr-Cu nanolaminate, (b) overall mesh with rigid indenter.

The mesh domain size is $5 \times 5.4 \times 105\ \mu m^3$. The simplified domain in Fig.4.11(a) shows a rigid, Berkovich indenter scratching the Cu-Gr-Cu nanolaminate surface. The domain is divided in half along the scratch length to decrease computational time. Symmetry conditions ($U_x = U_{R_y} = U_{R_z} = 0$) are applied to the left surface. The displacement and rotation (in all directions) for the bottom surface are set to zero. The displacement in the z-direction is restricted for the front and end surface. Finally, the right surface is assigned zero displacement in the x-direction. The inertial

contact friction between the Cu film and the indenter is proposed to be 0.11. This value is believed to represent a typical contact condition between a diamond tip and the polished surface of metal covered with a thin layer of natural oxides [60].

Simulations were performed with explicit time steps and reduced integration elements. To ensure a quasi-static assumption in an explicit analysis, the load is applied as a smooth step function so that the artificial kinetic energy does not oscillate and is less than 1% of the internal energy. During the scratch step, an explicit time step of 2 s is prescribed, which results in a scratch distance of 100 µm. The corresponding prescribed maximum load from the scratch experiments is 0.248 mN. A mass scaling of 1000 is used to decrease the computational time further. Adaptive meshing was used to avoid extreme distortion of elements. Since every remapping of the mesh causes some loss in precision [51, 61], the re-meshing frequency in adaptive meshing was kept as low as possible so that the precision of the solution is not lost while maintaining an undistorted element shape. We found that re-meshing every $5000^{th}$-time step was ideal for our simulation.

| Composite Type | | Young's Modulus (GPa) | Poisson's Ratio | Yield Strength (MPa) | Work Hardening (MPa) | Peak Load (mN) |
|---|---|---|---|---|---|---|
| Cu-Cu | Film | 107.8 | 0.343 | 600 | n/a | 2.6 |
| | Substrate | 107.8 | 0.343 | 160 | n/a | |
| Cu-Gr-Cu-Final | Film | 107.8 | 0.343 | 600 | 900 | 3.0 |
| | Substrate | 107.8 | 0.343 | 160 | n/a | |
| | Graphene | 1000 | 0.169 | | | |

Table 4.1: Summary of Mechanical Properties Used in the FEA Simulations of a Scratch Test.

The finite element Cu-Gr-Cu mesh shown in Fig.4.11(b) has 1456728 eight-node linear brick elements (C3D8R). These elements were chosen since they show a faster convergence than tetrahedral elements and do not have the inherent contact problems of quadratic elements [51]. Graphene is modeled with four-node quadrilateral membrane elements (M3D4R) with thickness $h = 0.335$ nm. In ABAQUS, membrane elements account for contributions to the elastic strain energy density from in-plane strains but neglect those from bending strains. Thus, while modeling graphene, we

have assumed that the out-of-plane bending stiffness is zero despite graphene having non-zero bending stiffness [18]. This assumption is valid for deformation states for which out-of-plane rotations occur as long as the elastic strain energy induced by the bending deformation is much less than the elastic strain energy induced by the in-plane deformation as it is with the friction test. In our nanoindentation experiments, we observed a no-slip interfacial condition between graphene and copper. Hence, in our numerical study, the no-slip interfacial condition is modeled by tying the nodes at the bottom of the film surface to the graphene nodes, which are then tied to nodes at the top substrate surface.

The Young's modulus and the yield strength of the Cu substrate used in the simulations were obtained from the nanoindentation results shown in the table. 3.2. A Poisson's ratio of 0.34 was set for copper.

Since the grain size for the Cu film lies between 300 nm and 600 nm, the yield strength of the Cu film is determined to be 600 MPa using inverse finite element analysis. The study by Nicola et al. [23] on plastic deformation of thin films shows that having a passivation layer (in our work, graphene is the passivation layer) on one side of the thin film dramatically increases the strength of film with high work-hardening observed as the dislocations remain inside the film due to being pinned at the interface between the film and the passivation layer. Similarly, strain hardening was also observed while compressing metal-graphene nanopillars [24], indicating the dislocation propagation being effectively blocked by graphene. Hence, to accurately model the plastic hardening of Cu-Gr-Cu in our numerical study, the film is assumed to harden linearly to 900 MPa at a 0.1 strain.

The 2D Young's Modulus of graphene is $348\,\mathrm{N\,m^{-1}}$, which upon normalizing by $t = 0.335$ nm yields an effective 3D Young's modulus of 1 TPa [4]. The in-plane Poisson's ratio for graphene is 0.17 [4, 12]. The out-of-plane Poisson's ratio is taken to be zero. A summary of the material properties used in both Cu-Cu and Cu-Gr-Cu nanolaminates are shown in Table 4.1.

Discretization errors occur from representing the governing equations and physical models as algebraic expressions in a discrete space and time domain. The temporal discreteness is manifested

through the time step taken while mesh size determines the discrete spatial domain. Therefore, it is essential to examine the sensitivity of the simulation results to the magnitude of the time step and the mesh size. As the mesh is refined, the solution becomes less sensitive to the mesh size and approaches the continuum solution. Similarly, decreasing the time step ensures continuum representation of the equations and zero temporal discretization error in the numerical study.

Temporal and spatial convergence was performed to ensure minimum discretization error. The analysis was rerun with the time step was reduced by 25%. Similarly, another spatial convergence study was performed by refining the mesh size by 25%. The numerical study did not show any sensitivity to the mesh size or the time step.

In an explicit analysis, apart from the time and mesh size convergence study, the sensitivity of the numerical results to mass scaling needs to be performed. Mass scaling is added to the explicit analysis for computational efficiency. The mass scaling factor value used in the simulation is 1000. For the convergence study, the numerical analysis was performed for a mass scaling factor of 500 and 1500. The numerical results did not show any sensitivity to the mass scaling factor.

A similar numerical study was performed on the control Cu-Cu nanolaminate in the absence of graphene and work hardening in Cu film.

### 4.3.5 Analysis Results

Fig. 4.12(a) and Fig. 4.12(b) represent the equivalent plastic strain contours in Cu-Cu and Cu-Gr-Cu nanolaminates near the scratch region. Equivalent plastic strain is the total plastic strain, $\bar{\varepsilon}^p = \int_0^t \sqrt{\frac{2}{3}\dot{\varepsilon}^p_{ij}\dot{\varepsilon}^p_{ij}}$, presented in section. 4.3.1. There is a significant reduction in plastic deformation in the Cu film for Cu-Gr-Cu nanolaminate compared to Cu-Cu nanolaminate. This confirms our hypothesis that graphene reduces the degree of plastic deformation in Cu nanolaminate, leading to lower work done/energy dissipated during scratch, consequently leading to lower CoF.

Fig. 4.14(a) and Fig. 4.14(b) represent the plastic energy dissipated contours in Cu-Cu and Cu-Gr-Cu nanolaminates near the scratch region. There is slightly higher plastic energy dissipated in Cu-Gr-Cu nanolaminate compared to Cu-Cu nanolaminate.

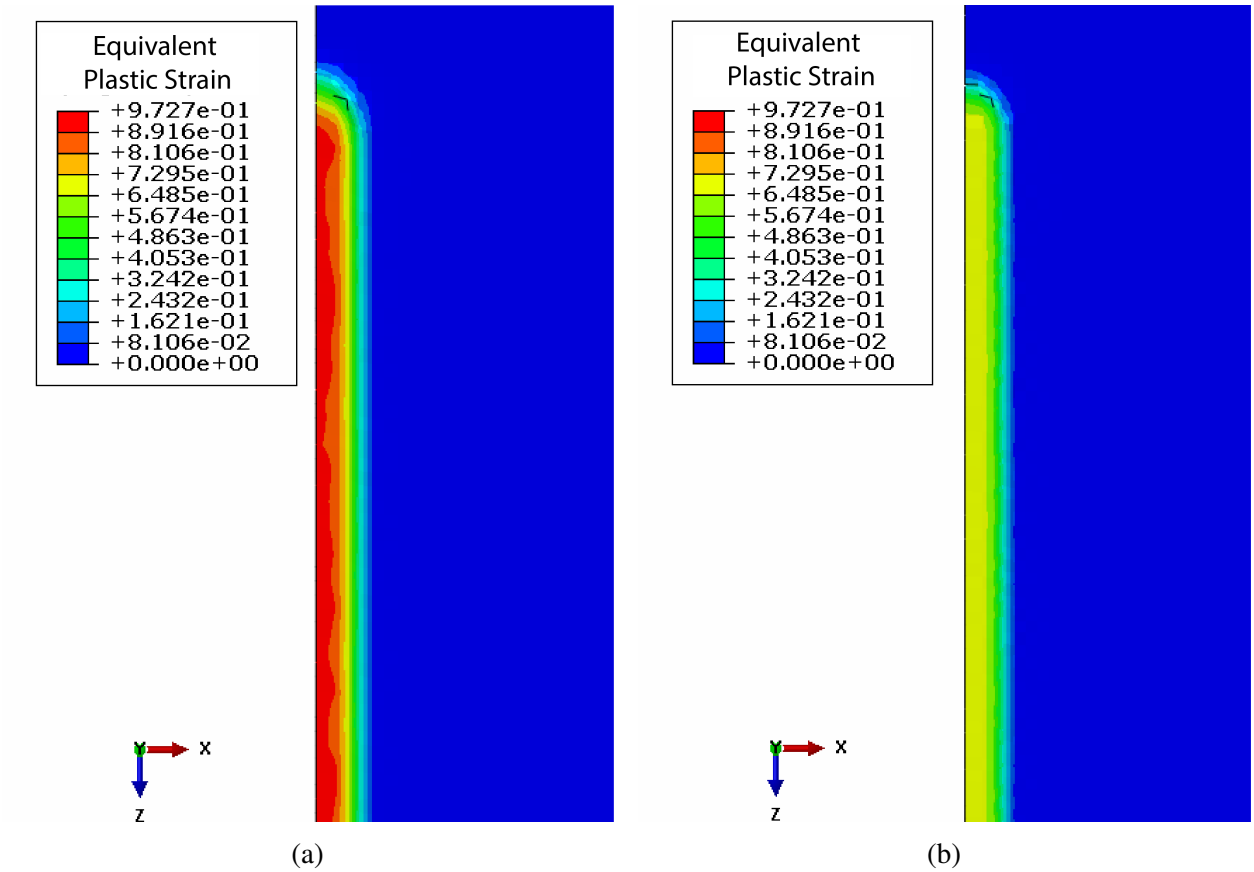


Figure 4.12: Top view of equivalent plastic strain contours for (a) Cu-Cu nanolaminate, and (b) Cu-Gr-Cu nanolaminate. Equivalent plastic strain is the total plastic strain, $\bar{\varepsilon}^p = \int_0^t \sqrt{\frac{2}{3}\dot{\varepsilon}^p_{ij}\dot{\varepsilon}^p_{ij}}$, presented in section. 4.3.1.

Fig. 4.15(a), Fig. 4.15(b), and Fig. 4.15(c) are FEA results presenting the normal load applied during a scratch, the lateral force measured during the scratch, and the calculated CoF respectively. The lateral force measured is slightly higher for Cu-Cu compared to Cu-Gr-Cu nanolaminates. Consequently, the CoF (calculated by taking the ratio of the lateral force to the normal load applied) is also slightly higher for Cu-Cu compared to Cu-Gr-Cu nanolaminates.

Though our numerical study shows that the plastic strain/deformation is significantly lower in Cu-Gr-Cu nanolaminate, continuum mechanics cannot accurately capture the influence of reduced plastic deformation on CoF.

Future work can entail using strain gradient plasticity or atomic-scale simulations methods to gain a fundamental understanding of the role of graphene in reducing the coefficient of friction in Cu-Gr-Cu nanolaminate. Gao and Urbassek [62] used molecular dynamics (MD) to study the influence of grain boundaries on scratching of Fe crystal using a hard repulsive tip. Scratch was performed on nanocrystalline Fe with the grain size varying from 71.4 Å to 114.2 Å. The MD results suggested that the coefficient of friction (CoF) decreased with an increase in grain size (at a fixed indenter size). Grain boundaries are known to act as a sink for dislocations, i.e., grain boundaries can absorb dislocations. Thus, the relative amount of grain boundary decreases with increasing grain size, resulting in a lower CoF. In our Cu/Gr nanolaminate, we expect graphene to act as an "anti-grain-boundary" in the sense that dislocation can not penetrate it. Thus decreasing the extent of plastic deformation in Cu-Gr-Cu nanolaminate and consequently reducing the CoF. An atomic-scale simulation of a scratch on Cu-Gr-Cu nanolaminates could give us an insight into the frictional response of Cu-Gr-Cu nanolaminate.

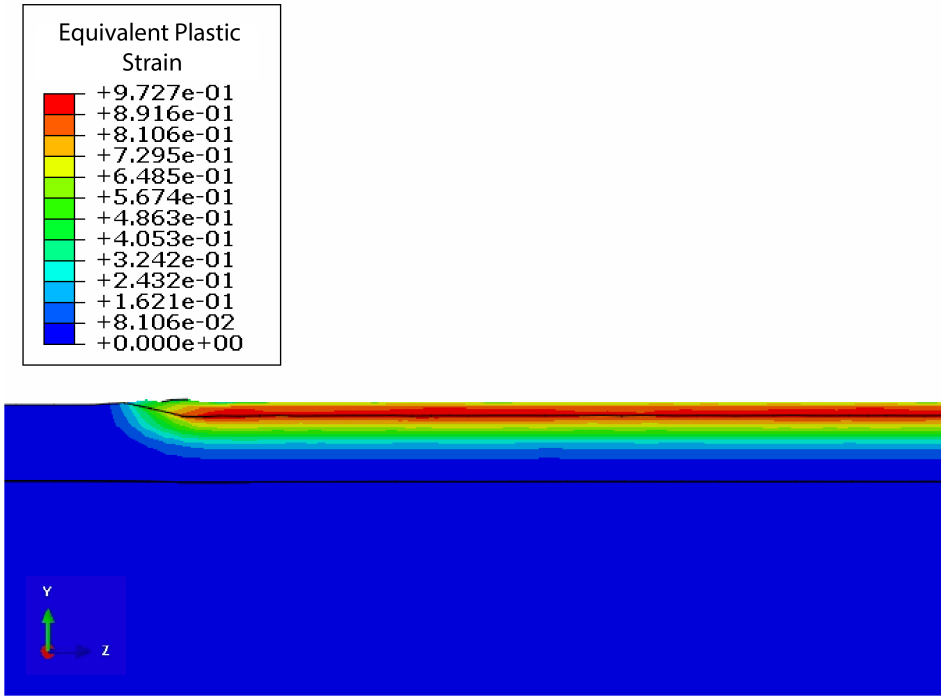


(a)

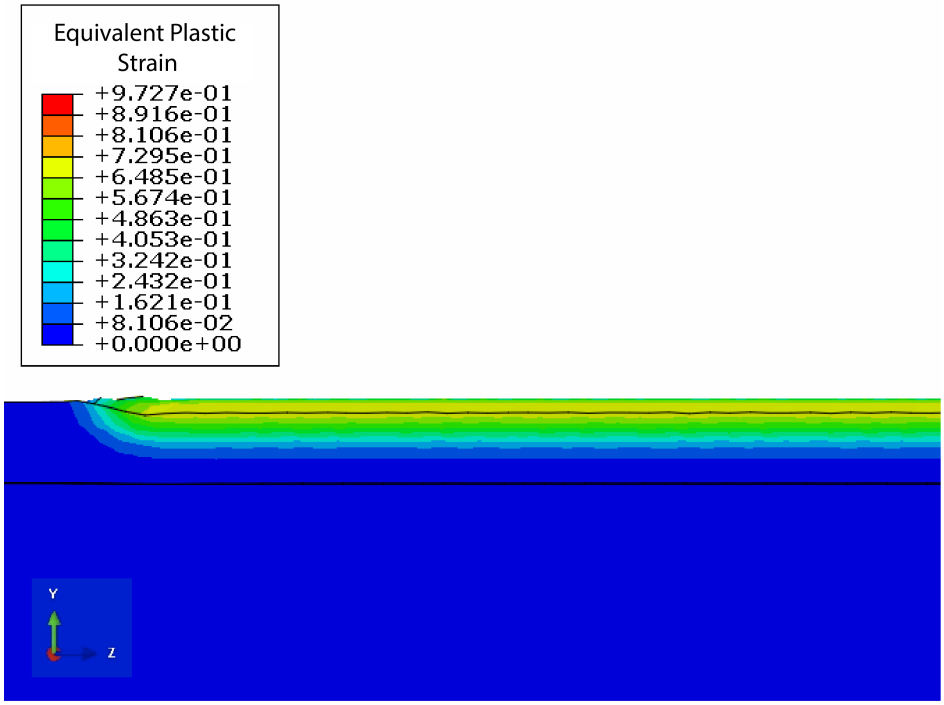


(b)

Figure 4.13: Side view equivalent plastic strain contours for (a) Cu-Cu nanolaminate, and (b) Cu-Gr-Cu nanolaminate. Equivalent plastic strain is the total plastic strain, $\bar{\varepsilon}^p = \int_0^t \sqrt{\frac{2}{3}\dot{\varepsilon}^p_{ij}\dot{\varepsilon}^p_{ij}}$, presented in section. 4.3.1.

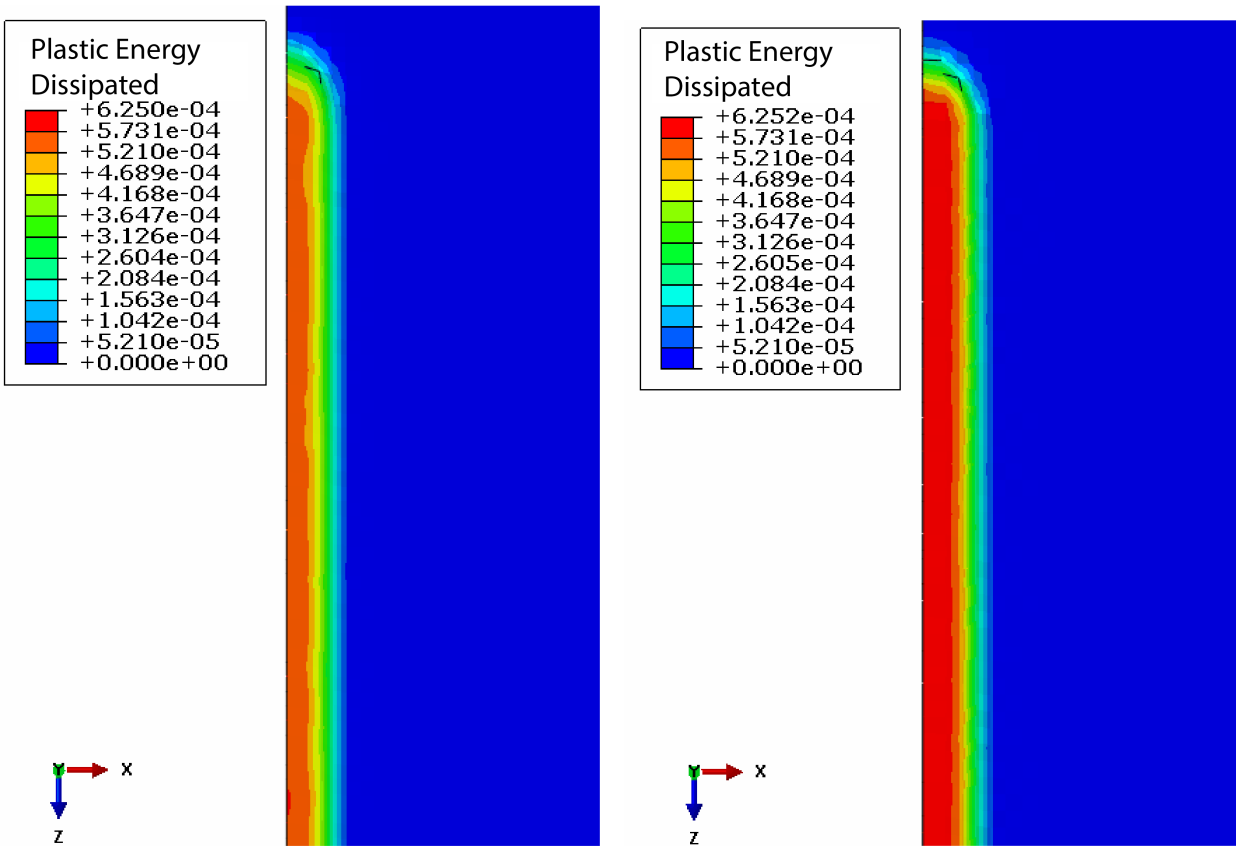


Figure 4.14: Top view of plastic energy dissipated (per unit volume) contours for (a) Cu-Cu nanolaminate, and (b) Cu-Gr-Cu nanolaminate.

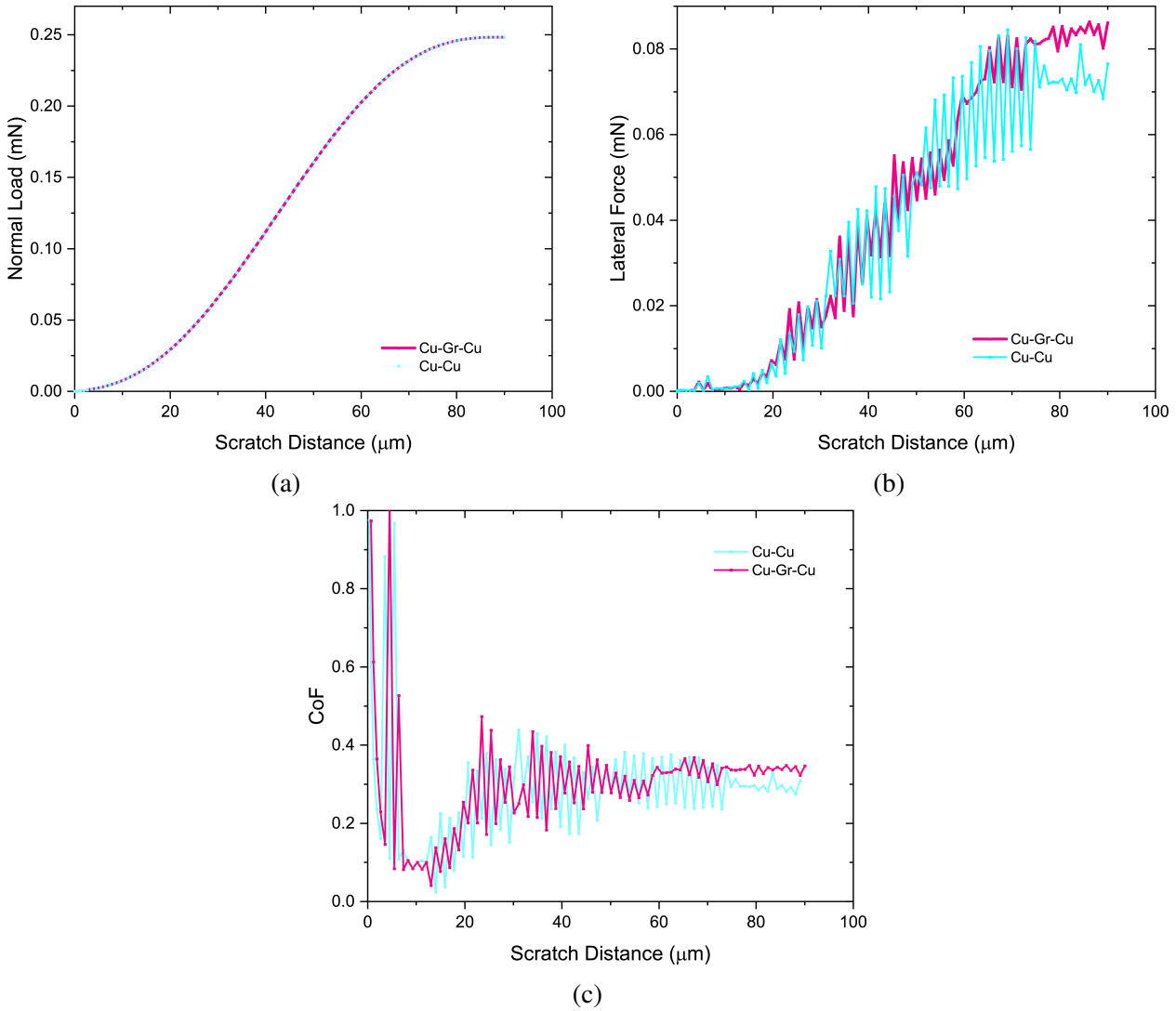


Figure 4.15: FEA results (a) Typical normal load vs. scratch distance, (b) measured lateral force, and (c) coefficient of friction (CoF) for Cu-Cu and Cu-Gr-Cu nanolaminates.

# Chapter 5: Enhanced Strength of Cu-Gr-Cu nanolaminate

In chapter 3 and chapter 4, graphene's ability to constrain dislocation motion across the Cu/Gr interface led to increased hardness and reduction in coefficient of friction in Cu-Gr-Cu nanolaminate. In this chapter, we utilize graphene's effectiveness in blocking dislocations to enhance the strength of Cu-Gr-Cu nanolaminate. In the following sections, we outline the fabrication of nanolaminate cantilever beams. Bending tests performed on fabricated Cu-Gr-Cu nanolaminate cantilever beams exhibited a remarkable strengthening effect over a control Cu-Cu nanolaminate. The enhancement in strength of Cu-Gr-Cu nanolaminate suggests a build-up of dislocations at the Cu-Gr interface, limiting the plastic slip that can occur at the internal interface. We employed a strain gradient plasticity computational model of the experimental system based upon Gudmundson's higher-order theory and implemented it as a user element in ABAQUS. A set of material parameters is identified that reproduce the experimental force vs. displacement results for both the Cu-Cu and the Cu-Gr-Cu nanolaminate. The results give insight into the design of metal-graphene composites and the structure of strain gradient plasticity theories. Details and results of the FEA simulations are presented in the finite element modeling section.

## 5.1 Nanolaminate Fabrication

A high purity, 1.5 mm thick, single crystal copper substrate is electropolished using Rotating Disk Electrode (RDE) polishing to remove surface contamination and reduce the surface roughness to less than 2 nm. The Cu substrate is mounted on a rotating disk, which acts as an anode and is dipped into an 85% (by volume) phosphoric acid electrolyte. A platinum mesh (Alfa Aesar) is used as a cathode, while a Gamry Calomel (Ag/AgCl) electrode is used as a reference. The Cu substrate is electropolished to remove 110 μm of material thickness and reduce the surface roughness to less

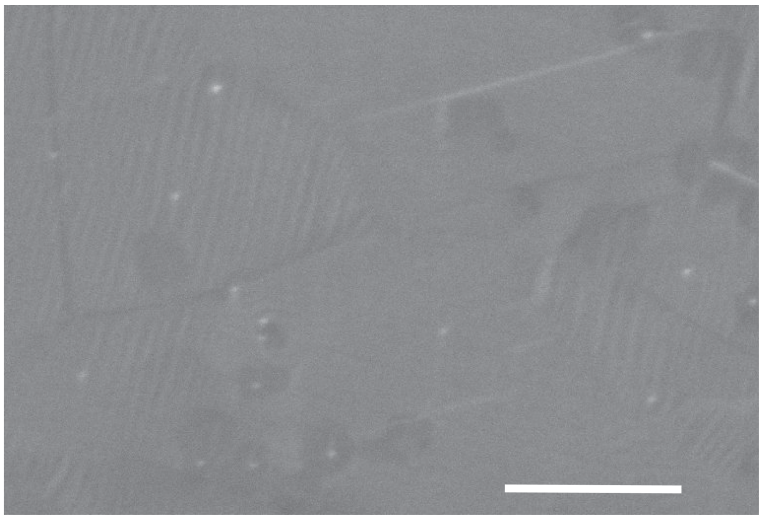

Figure 5.1: Scanning Electron Microscopy image of graphene. Scale is 2 µm.

than 2 nm.

A continuous single atomic layer of graphene is then grown on the substrate via chemical vapor deposition (CVD)(Fig. 5.1). The electropolished copper substrate is first annealed at 1000 °C for 2 hrs in a gas mixture of $H_2$ (5 sccm) and Ar (50 sccm) at 1 Torr. Graphene growth takes place at 1000 °C for 30 min using methane as the precursor gas. During the growth stage, methane and hydrogen flow at 5 sccm and 10 sccm, respectively, while maintaining a pressure of 0.3 Torr. Raman spectroscopy confirmed that the resulting graphene is primarily a single atomic layer with a good G/2D ratio of 1/3 [12, 36].

Next, a high-purity Cu film of thickness 280 nm is deposited via physical vapor deposition (PVD) at room temperature atop the graphene to synthesize a Cu-Gr-Cu nanolaminate.

For comparison, a control — Cu-Cu nanolaminate — sample (not shown) was synthesized according to the procedure described above; however, methane did not flow through the furnace during the graphene growth stage, ensuring both nanolaminate structures were subjected to the same thermal cycle. Another modification while fabricating the control sample was to deposit the Cu film at 200 °C on the Cu-Substrate to ensure similarity in the grain size distribution of the Cu film in both Cu-Gr-Cu and Cu-Cu nanolaminate structure.

Grain size and grain orientation were measured using Electron Backscatter Diffraction on scan-

ning electron microscope. Fig. 5.2 shows that the mean grain size is 290 nm for both Cu-Cu and Cu-Gr-Cu nanolaminate structures. The reader can refer to chapter 2 for further details on the fabrication process and the grain size distribution charts.

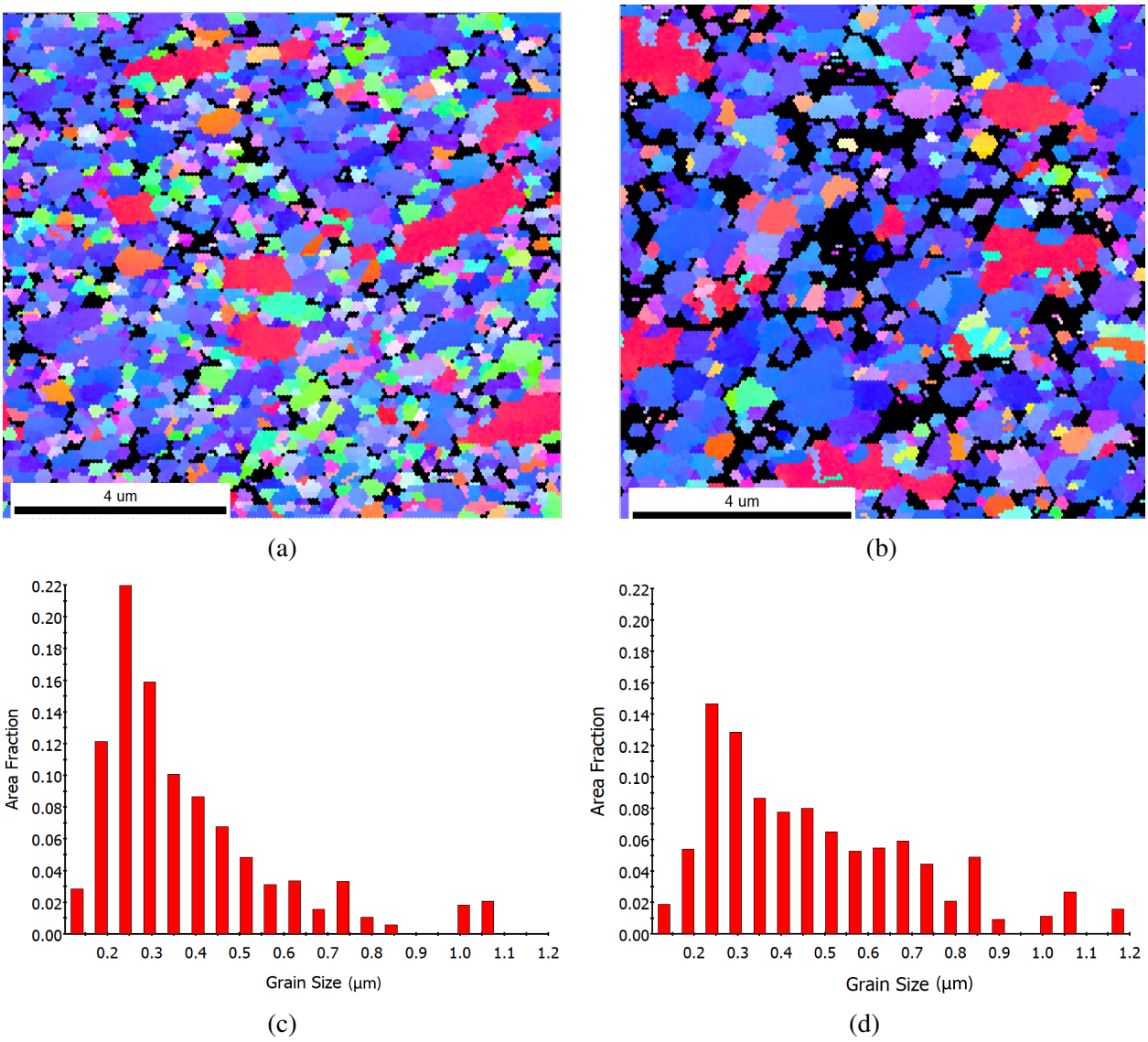


Figure 5.2: EBSD mapping, (a) Inverse Pole Figure (IPF) map for Cu-Cu, (b) IPF map for Cu-Gr-Cu, (c) grain size distribution for Cu-Cu, (d) grain size distribution for Cu-Gr-Cu.

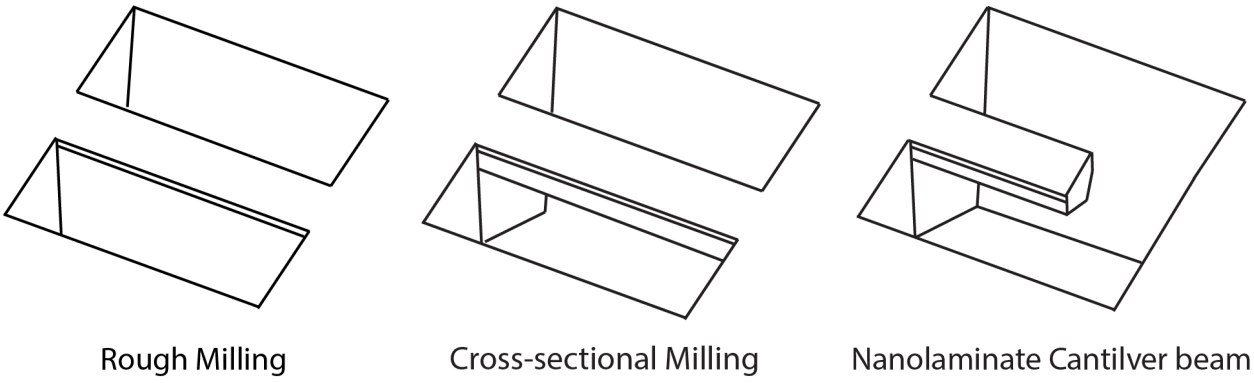


Figure 5.3: Schematic detailing cantilever fabrication process, (a) rough milling to create two trapezoidal cavities, (b) cross-milling (c) final polishing to fabricate cantilever beam with pentagonal cross-section.

## 5.2 Experiments

### 5.2.1 Fabrication of Cantilever Beams

All cantilever beams were fabricated with the longitudinal axis along the [1 0 0] crystallographic direction and the top surface corresponding to the (0 0 1) plane of the Cu substrate. This ensured uniformity in the mechanical behavior of the Cu-substrate across all cantilever beams during the bending test. Cantilever beams of Cu-Cu and Cu-Gr-Cu nanolaminates were fabricated using the FEI Helios NanoLab 660, dual-beam SEM/FIB operated at 30 kV. The schematic detailing the cantilever fabrication process is shown in Fig. 5.3. Milling was carried out in three consecutive steps: (1) rough milling of two trapezoidal cavities 4 µm to 5 µm apart using 9.3 nA of current, (2) followed by cross-sectional milling (cutting) using 0.79 nA of current, and (3) final polishing of the cantilevers using 0.34 nA of current. The fabricated beams have a pentagonal cross-section, with length $L = 15$ µm, width $b = 3$ µm and total thicknesses $t = 4$ µm (Fig. 5.4(a)).

Fig. 5.4(b) is an SEM image of a fabricated Cu-Gr-Cu cantilever beam. Four cantilever beams of Cu-Gr-Cu nanolaminate and three cantilever beams of Cu-Cu nanolaminate were fabricated to characterize the strength of the lamellar composites.

Flexural rigidity or bending stiffness of a beam determines the resistance of a member against

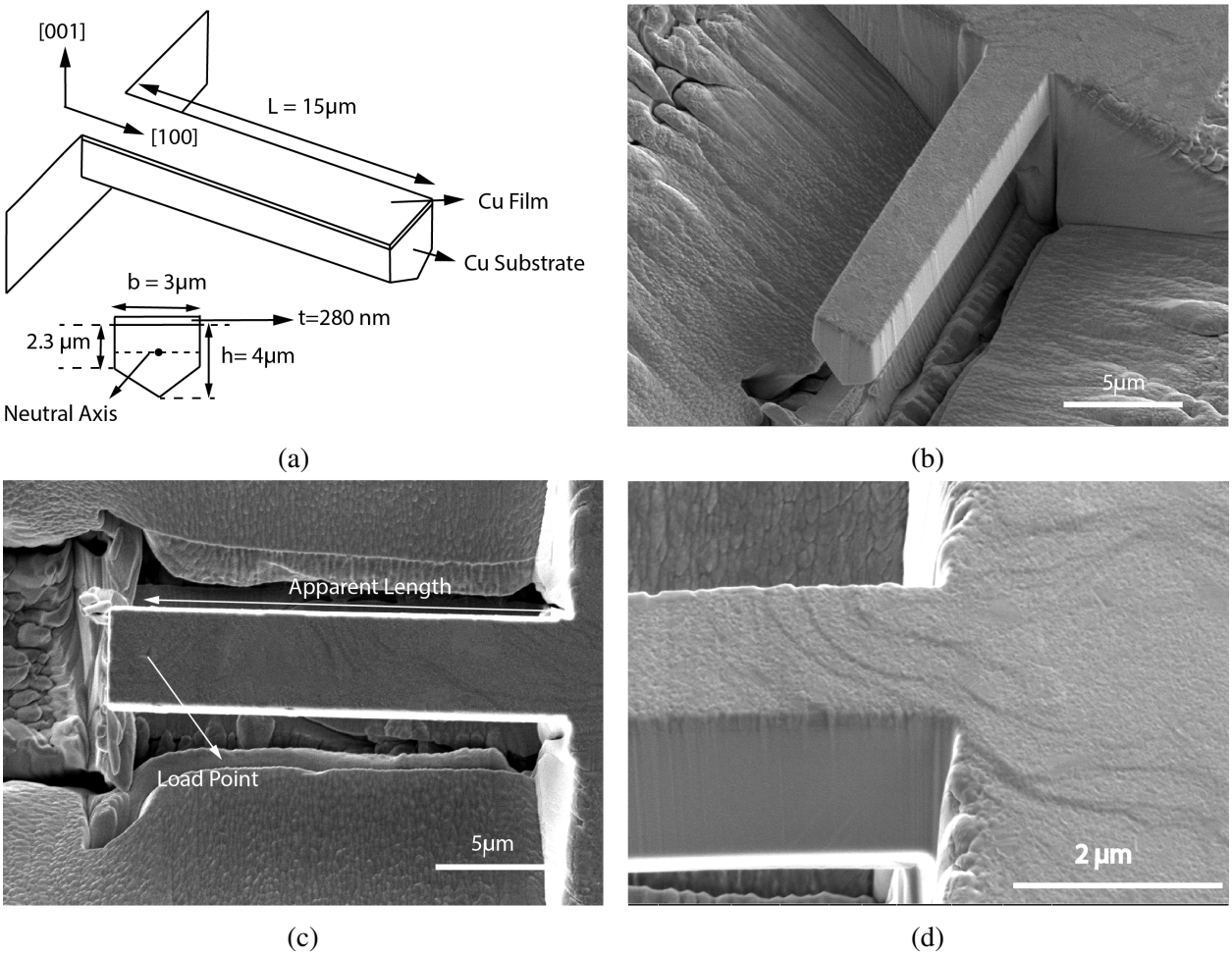


Figure 5.4: (a) Schematic detailing the dimensions of the fabricated cantilever beam, (b) SEM image of Cu-Gr-Cu cantilever beam before the bending test, (c) and (d) SEM images of Cu-Gr-Cu cantilever beam after the bending test. Slip planes, 45° to surface, are present in the Cu-substrate (d).

bending deformation. The first step towards calculating the flexural rigidity of the nanolaminates is to determine the position of the neutral axis (N.A.). The N.A. for Cu-Cu and Cu-Gr-Cu cantilever is at 2.19 μm and 2.195 μm from the top beam surface, respectively. The composite's effective flexural rigidity can then be calculated using the equation below:

$$EI_{eff} = E_s I_s + E_f I_f + E_g I_g. \tag{5.1}$$

The subscript $s$, $f$, and $g$ correspond to Cu-substrate, Cu film, and graphene. The calculated effective flexural rigidity for Cu-Cu and Cu-Gr-Cu nanolaminates are 840.14 mNμm$^2$ and

842.29 mNμm$^2$ respectively. All the above calculations are performed assuming the thickness of graphene to be $h = 0.335$ nm. Adding a single layer of graphene to the composite increases the flexural rigidity by 0.25%.

In the next section, the influence of a single layer of graphene on the strength of the composite is evaluated through a series of bending tests performed on the fabricated Cu-Gr-Cu cantilever beams.

### 5.2.2 Cantilever Beam Bending Experiments

The bending test of cantilever beams was performed using a G200 Nanoindenter (KLA Corporation, Milpitas, CA, USA). A diamond Berkovich tip was used to deflect the cantilever beam to a measured downward vertical displacement of 700 nm. When the displacement limit was reached, the indenter was withdrawn from the sample completely. Fig. 5.4(c) and Fig. 5.4(b) are SEM images of a Cu-Gr-Cu cantilever beam after the bending test. The load point was determined from the SEM images of the cantilever beams. The distance from the load point to the fixed end of the beam is the apparent length of the cantilever beam. Table 5.1 lists the apparent lengths of Cu-Gr-Cu and Cu-Cu nanolaminate cantilever beams. The average apparent length for Cu-Cu cantilever beam is 12.90 μm while the average apparent length for Cu-Gr-Cu cantilever beam is 12.89 μm.

Given the variation in length of cantilever beams, the best way to present the load-displacement curves is to normalize the load and displacement. According to classical beam theory, the vertical displacement or deflection of a cantilever beam depends on the length $L$, the flexural rigidity $EI$, and the force $F$:

$$\frac{FL^2}{EI} = 3\frac{d}{L}. \tag{5.2}$$

Hence, we normalize displacement by dividing it by length and normalize load by multiplying it by $L^2/EI$. According to Eqn. 5.2, the normalized load-displacement graph should give us a linear elastic slope of 3. However, on normalizing our experiment data, we obtain a linear elastic slope of 3.8 (Fig. 5.5). The high linear elastic slope can be attributed to:

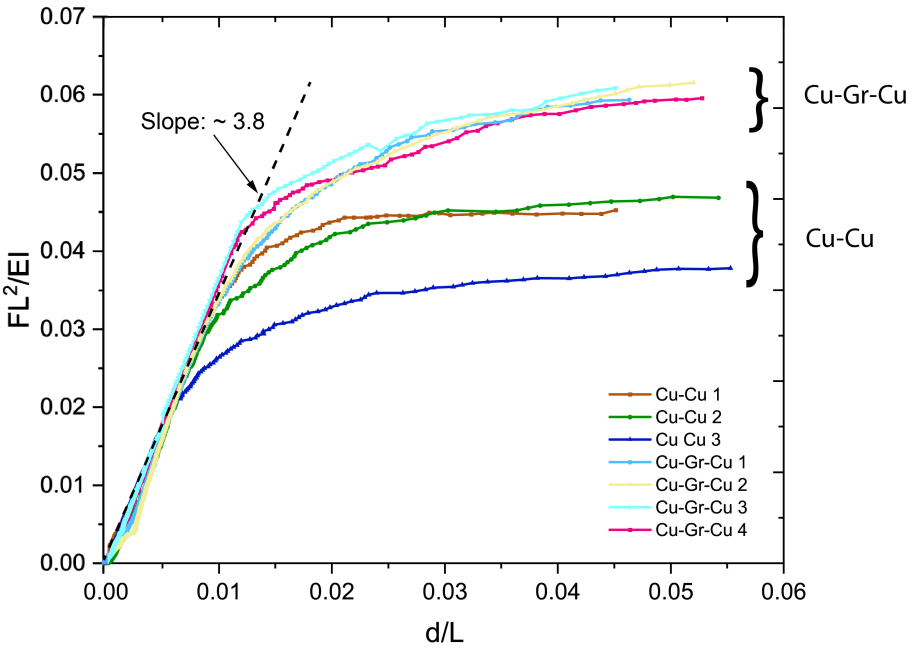


Figure 5.5: Initial normalized load-displacement curve with a linear elastic slope of 3.8.

- A small indentation on the beam at the load point.
- The cantilever beams are attached to an elastic foundation, hence a non-ideal boundary condition.
- Ambiguity in measuring the cantilever beams' length

Therefore, a series of corrections are applied to the experimental data to correct the indentation at the load point, the elastic foundation, and the length of the beam. The following paragraphs provide details of these corrections.

**Correcting for Indentation**

A small indent is seen at the load point, suggesting that the actual beam displacement is the prescribed displacement of the diamond indenter tip minus the indentation depth of the diamond tip into the beam. The following methodology is used to correct for the small penetration depth caused by indentation during beam bending:

1. A series 10 of nanoindentations were performed on the bulk nanolaminates and the measured force-displacement curves were averaged.

2. The indentation load-displacement curve was fitted and a quadratic relation between the displacement and force was found (Fig. 5.6)(b).

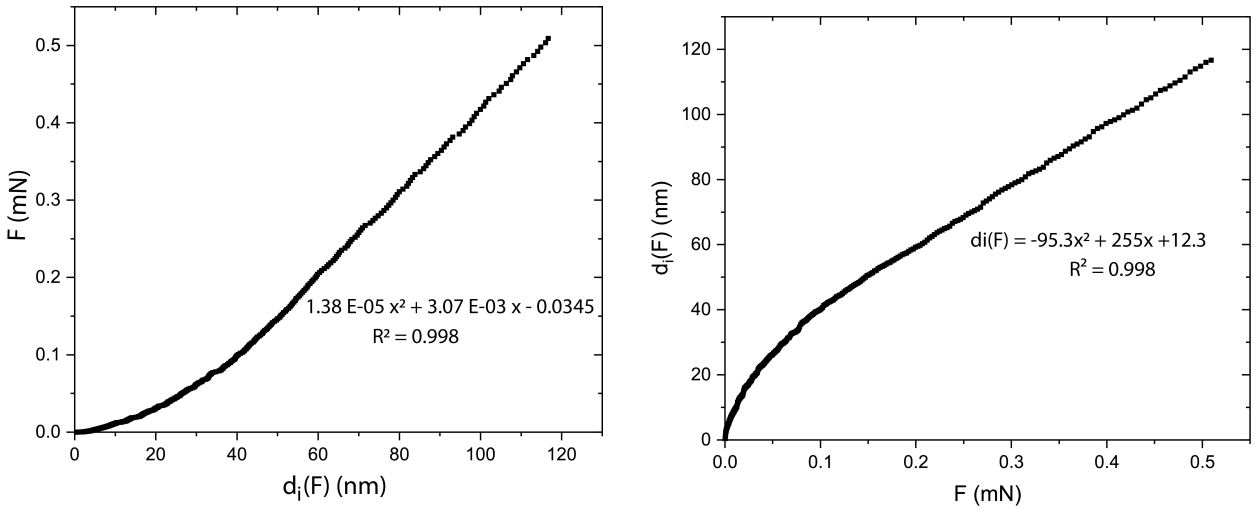


(a) (b)

Figure 5.6: (a) Load-displacement data for nanoindentation into the bulk of the nanolaminate, (b) displacement-load data for nanoindentation into the bulk of the nanolaminate.

3. The measured load data from the cantilever beam experiment was then substituted into the quadratic relation to determine the indentation-displacement correction factor $d_i$.

4. Finally, $d_i$ was subtracted from the measured displacement $d_m$ to correct for the indent depth.

$$d_{ci}(F) = d_m(F) - d_i(F). \tag{5.3}$$

**Accounting for Elastic Support**

The cantilever beams in the experiment are not ideally clamped to a rigid surface at the base. The elastic and plastic deformation at the base of the cantilever beam extends into the bulk of the nanolaminate permitting deformation. Thus we can consider the cantilever beam to be attached to an elastic support allowing us to account for the added compliance provided by the bulk of the nanolaminate. The following methodology is used to account for the contribution of the elastic support towards the beam bending behavior:

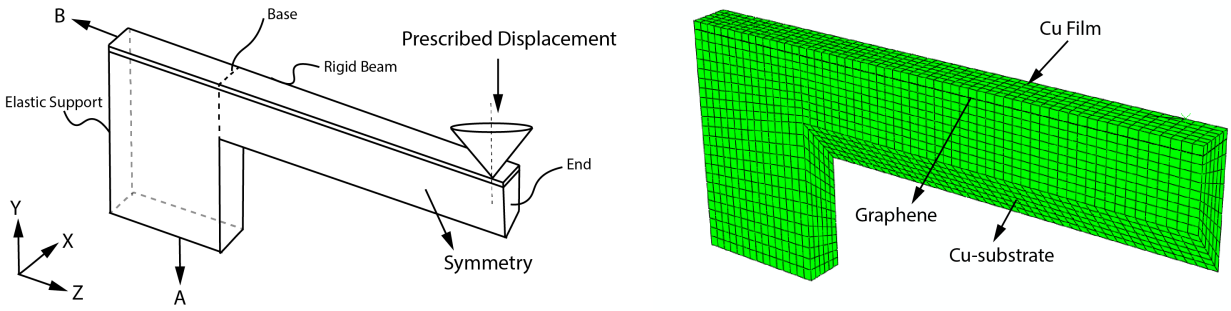


(a) (b)

Figure 5.7: 3D finite element simulations of cantilever bending experiments, (a) schematic of the bending test of Cu-Gr-Cu nanolaminate, (b) overall mesh with rigid indenter.

1. Numerical 3D simulations of the bending test were performed using ABAQUS [51]. The Berkovich indenter modeled as a rigid analytical surface shaped like a cone was used to displace the end of the nanolaminate cantilever beam Fig. 5.7(a). An elastic support attached to the base of the cantilever beam was modeled to permit elastic deformation in the support. The single crystal Cu-support was modeled using a user-material subroutine that incorporates single-crystal elasticity and plasticity constitutive relations to account for the kinematics of finite deformation and lattice rotation associated with single-crystal plasticity [63]—making the numerical analysis of beam bending closest to the experiments. The single crystal portion of the support was modeled as anisotropic elastic while the film was modeled as isotropic elastic. Further details of the model and the mesh are presented in appendix C.

2. To single out the elastic contribution of the support, the cantilever beam is modeled as a rigid beam while the rectangular support exhibits linear elastic behavior.

3. The slope of the observed normalized linear displacement-force relation is the support compliance $C_s$ (Fig. 5.8).

4. The support compliance, $C_s$, was multiplied with the normalized bending load data to find the support-displacement correction factor ($d_s$).

$$\frac{d_s}{L} = C_s \frac{FL^2}{EI}. \tag{5.4}$$

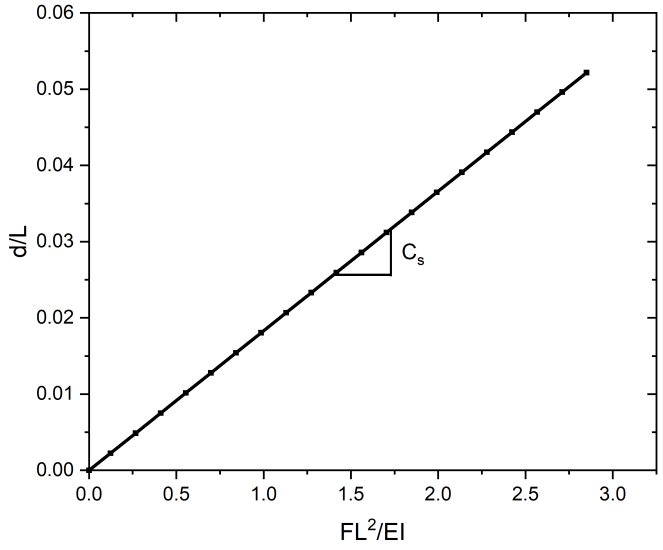


Figure 5.8: Slope of the normalized displacement-load relation provides the support compliance $C_s$ that will account for an elastic support.

Here, EI = 840.14 mNμm$^2$.

5. Finally, $\frac{d_s}{L}$ can be subtracted from the normalized indentation corrected displacement to correct for the elastic support.

$$\frac{d}{L} = \frac{d_{ci}}{L} - \frac{d_s}{L}. \tag{5.5}$$

The ratio $\frac{d_s}{L}$ is unambiguous, but the length L used to normalize $d_{ci}$ is ambiguous. The effective length used to normalize the experiment data is determined in the next section.

**Determining the Effective Length of the Cantilever Beam**

Since a Berkovich tip is used to deflect the beam, an ideal point load condition does not exist, leading to ambiguity in measuring the length of the cantilever beam. In addition, the presence of curved corners at the fixed end of the cantilever (an artifact of the FIB fabrication process) adds to the uncertainty in measuring the length of the cantilever beam. Hence, an "effective" length (Table 5.1) is determined for each cantilever beam such that when used to normalize our experiment data, the experiments have a linear elastic slope of 3:

$$\frac{FL^2}{EI} = 3\frac{d}{L}. \tag{5.6}$$

On substituting Eq. 5.5 and Eq. 5.4 in Eq. 5.6, we get

$$\frac{FL^2}{EI} = 3\left(\frac{d_{ci}}{L} - \frac{d_s}{L}\right) \tag{5.7}$$

$$\frac{FL^2}{EI} = 3\left(\frac{d_{ci}}{L} - C_s\frac{FL^2}{EI}\right) \tag{5.8}$$

$$\frac{1}{3}\frac{FL^2}{EI} = \frac{d_{ci}}{L} - C_s\frac{FL^2}{EI} \tag{5.9}$$

$$\left(C_s + \frac{1}{3}\right)\frac{FL^2}{EI} = \frac{d_{ci}}{L} \tag{5.10}$$

$$\frac{FL^3}{EI} = \frac{3}{1+3C_s}d_{ci} \tag{5.11}$$

$$\frac{F}{d_{ci}} = \frac{3EI}{(1+3C_s)L^3} = m_{ci} \tag{5.12}$$

where $m_{ci}$ is the slope of the force vs. indentation corrected displacement in our experiment. Hence we rearrange the above equation to determine the effective length of the cantilever beam

$$L = \left(\frac{3EI}{(1+3C_s)m_{ci}}\right)^{\frac{1}{3}}. \tag{5.13}$$

The effective length for each cantilever beam is calculated and listed in table.5.1. The effective length is $2-5\%$ smaller than the apparent length of the cantilever beams.

| **Cantilever Beam** | **Apparent Length** (μm) | **Effective Length** (μm) | **% Length** |
|---|---|---|---|
| Cu-Cu 1 | 13.0 | 12.7 | -1.90 |
| Cu-Cu 2 | 12.1 | 11.5 | -4.80 |
| Cu-Cu 3 | 12.2 | 11.6 | -4.80 |
| Cu-Gr-Cu 1 | 11.2 | 10.9 | -2.60 |
| Cu-Gr-Cu 2 | 12.7 | 12.4 | -2.30 |
| Cu-Gr-Cu 3 | 11.4 | 11.3 | -1.60 |
| Cu-Gr-Cu 4 | 12.8 | 12.3 | -3.90 |

Table 5.1: Summary of Apparent and Effective Lengths of Cu-Cu and Cu-Gr-Cu Nanolaminate Cantilever Beam. The values in the table have been rounded to 3 significant figures.

### 5.2.3 Experimental Results

Effective lengths are used to normalize the corrected load-displacement curves for all Cu-Cu and Cu-Gr-Cu cantilever beams and are presented in Fig. 5.9. The average normalized load-displacement curves for both Cu-Cu and Cu-Gr-Cu cantilever beams are also shown in Fig. 5.10. These normalized force-displacement curves reveal that a significantly higher load is required to deflect a Cu-Gr-Cu cantilever beam to a vertical displacement of 700 nm. Additionally, an increase in flow strength and strain hardening is observed in Cu-Gr-Cu nanolaminate due to the presence of graphene.

The mean normalized peak load for Cu-Gr-Cu is 0.052 with a standard deviation of 0.00082, while the mean normalized peak load for Cu-Cu is 0.036 with a standard deviation of 0.0031. A two-sample t-test was performed to establish a significant difference in the mean normalized peak load for Cu-Cu nanolaminate and Cu-Gr-Cu nanolaminate. A p-value of 0.0002 was observed irrespective of the assumption of equal or unequal variance. Since the p-value is much less than the significance level of 0.05, we can confidently state that the enhancement in strength is due to a single layer of graphene and not attributed to the random noise in the data.

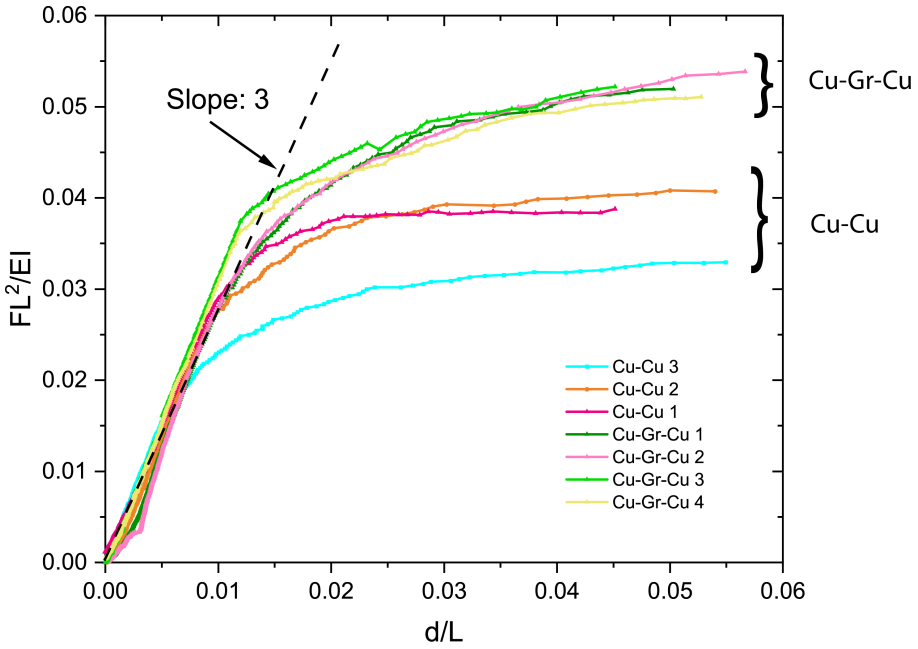


Figure 5.9: Normalized experiment load-displacement curves of all nanolaminate cantilever beams

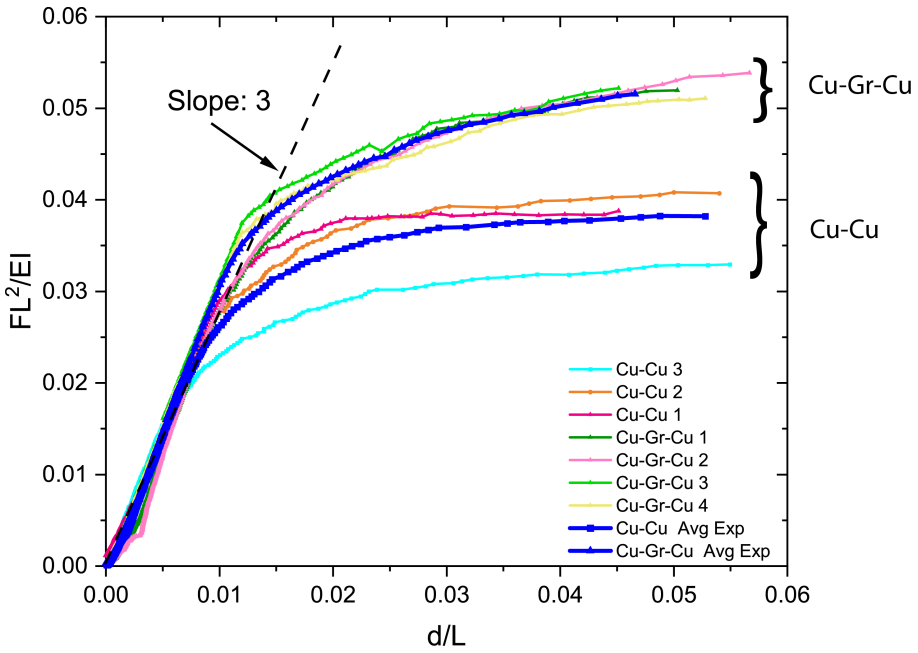


Figure 5.10: Average normalized load-displacement curve for Cu-Cu and Cu-Gr-Cu. The dark blue curves are the average normalized load-displacement curve for Cu-Cu and Cu-Gr-Cu.

Bending tests of Cu-Gr-Cu nanolaminate cantilever beams revealed that a single atomic layer of graphene enhances the strength of the Cu nanolaminate. A significantly higher force was required to deflect the Cu-Gr-Cu cantilever beam when compared to the Cu-Cu cantilever beam. The inclusion of graphene increased the flow strength when compared to Cu-Cu nanolaminate. In addition, an increased degree of strain hardening was observed in Cu-Gr-Cu nanolaminates.

Flow strength of a material corresponds to the stress required at a given strain rate for continuous nucleation, multiplication, and propagation of plastic deformation in the crystalline material. The enhancement of strength found in Cu-Gr-Cu nanolaminate suggests that the dislocations formed in the Cu-substrate during beam bending are prevented from crossing the Cu/Gr interface due to graphene's ability to block dislocation propagation. The constraints on plastic slip across the Cu/Gr interface results in the remarkable strengthening of the Cu nanolaminate. These findings suggest that graphene's high intrinsic mechanical strength provides an effective barrier against dislocation motion despite being only a single atomic layer in thickness.

The remarkable strengthening effect seen in our work is consistent with previous studies on passivated thin films [31], and metal nanolayered composites [18, 23, 48, 49]. For example, the experimental study by Xiang and Vlassak [31] and Nicola et al. [23] showed that a passivated Cu film (in our work, graphene is the passivation layer) has a higher yield stress and work hardening when compared to unpassivated film of the same grain size and thickness as the dislocations are pinned at the interface between the film and the passivation layer. Similarly, Kim et al. [24] performed nanopillar compression tests of Cu-Gr nanolayered composites and reported the 5% flow strength of Cu-Gr nanolayered composite to be 2.5 times the 5% flow strength of Cu nanolayered composite. Strain hardening was also observed while compressing metal-graphene nanopillars, indicating that the dislocation motion was being effectively blocked by graphene.

In the next section, we present a strain gradient plasticity (SGP) computational model of the experiment based on Gudmundson's higher-order theory [64] implemented as a user element in ABAQUS [65]. The use of SGP theory is motivated by the fact that constraint on plastic slip across the Cu/Gr interface leads to a plastic strain gradient near the Cu/Gr interface. The constraint on

plastic flow imposed by graphene cannot be described by classical plasticity theories but can be modeled with strain–gradient plasticity.

## 5.3 Strain Gradient Plasticity Description

### 5.3.1 A Brief Introduction to Strain–Gradient Plasticity

Dislocation theory suggests that the plastic flow strength of a solid depends on both the strains and the strain gradients. Plastic deformation is due to the combined presence of geometrically necessary dislocations associated with plastic strain gradients and statistically stored dislocations associated with plastic strain. Hence, the pivotal step in constructing phenomenological theories was to represent the plastic work in terms of plastic strain and plastic strain gradient, thereby adding a length scale into the material description. Generally, strain gradients are inversely proportional to the length scale over which plastic deformation occurs. Thus gradient effects become essential for plastic deformation taking place at the micrometer scale.

The Hall–Petch effect seen in our experiments can be interpreted in the context of plastic strain gradients. Since single-layer graphene acts as an obstacle to dislocation movement, the dislocation pile-up at the Cu-Gr interface leaves a large plastic strain gradient near the interface. The presence of large plastic strain gradients implies the presence of a large density of geometrically necessary dislocations. This increase in dislocation density increases the flow strength of Cu-Gr-Cu nanolaminate.

In order to accurately describe the size effect exhibited in micro/nanostructured materials and address the strengthening and hardening mechanisms, the SGP model incorporates both dissipative (that is, unrecoverable) and energetic (that is, recoverable) gradient contributions. Numerical investigations [66] of a material's response under cyclic shear show that the dissipative gradient effects lead to an increase in yield strength, whereas energetic gradient contributions lead to increased hardening and a Bauschinger effect. In our experiments we see enhancement of strength, we will only consider dissipative gradient contributions and ignore the energetic gradient contributions.

In the following section, the strain gradient plasticity (SGP) effect seen in our bending experiment is modeled using Gudmundson's higher-order theory [64] implemented as user elements in ABAQUS [65]. The constitutive model is presented in section 5.3.2.

### 5.3.2 Strain gradient plasticity model

Small deformation theory for strain gradient plasticity is adopted. The total strain rate $\dot{\varepsilon}_{ij}$ is the symmetric part of the spatial gradient of the displacement rate $u_i$ , such that $\dot{\varepsilon}_{ij} = (\dot{u}_{i,j} + \dot{u}_{j,i})/2$. It is assumed that the strain tensor $\varepsilon_{ij}$ can be expressed as the sum of elastic $\varepsilon^e_{ij}$ and plastic strains $\varepsilon^p_{ij}$, where plastic volume changes are neglected.

***Variational principles and governing equations***

Gudmundson's SGP model assumes that the plastic strain gradients contribute to the work per unit volume. Hence, the principle of virtual work includes contributions both from the elastic strains, the plastic strains and plastic strain gradients. The principle of virtual work over a volume $V$ with surface $S$ can be expressed as

$$\int_V \left( \sigma_{ij} \delta \varepsilon^e_{ij} + q_{ij} \delta \varepsilon^p_{ij} + \tau_{ijk} \delta \varepsilon^p_{ij,k} \right) \mathrm{d}V = \int_S \left( T_i \delta u_i + t_{ij} \delta \varepsilon^p_{ij} \right) \mathrm{d}S \tag{5.14}$$

where Cauchy stress is denoted by $\sigma_{ij}$. The right-hand side of Eq. (5.14) includes both conventional surface tractions $T_i$ and higher-order tractions $t_{ij}$. The work conjugates to plastic strains, and plastic strain gradients will be denoted as micro stresses $q_{ij}$ and as higher-order stress tensor $\tau_{ijk}$. It should be noted that only a deviatoric parts of $q'_{ij}$ and $\tau'_{ijk}$ contribute to virtual work. Below, the superscript primes denoting deviatoric parts of $q_{ij}$ and $\tau_{ijk}$ will be omitted. The deviatoric part of Cauchy stress $\sigma'_{ij}$ is a work conjugate to plastic strain. The principle of virtual work can be alternatively presented as

$$\int_V \left( \sigma_{ij} \delta \varepsilon^e_{ij} + (q_{ij} - \sigma'_{ij}) \delta \varepsilon^p_{ij} + \tau_{ijk} \delta \varepsilon^p_{ij,k} \right) \mathrm{d}V = \int_S \left( T_i \delta u_i + t_{ij} \delta \varepsilon^p_{ij} \right) \mathrm{d}S \tag{5.15}$$

where $n_k$ is the unit outward normal to the surface $S$. Applying Gauss divergence theorem, equilibrium within $V$ yields the governing equations

$$\begin{aligned} \sigma_{ij,j} &= 0 \\ \tau_{ijk,k} + \sigma'_{ij} - q_{ij} &= 0 \end{aligned} \tag{5.16}$$

with kinematic boundary conditions of prescribed $u_i$ and prescribed $\varepsilon^p_{ij}$, and with natural boundary conditions,

$$\begin{aligned} T_i &= \sigma_{ij} n_j \\ t_{ij} &= \tau_{ijk} n_k. \end{aligned} \tag{5.17}$$

***Constitutive description***

Gudmundson [64] and Fleck and Willis [67] elucidate that both $q_{ij}$ and $\tau_{ijk}$ can have disspative and energetic contributions : $q_{ij} \equiv q^D_{ij} + q^E_{ij}$ and $\tau_{ijk} \equiv \tau^D_{ijk} + \tau^E_{ijk}$, where the superscripts D and E denote dissipative and energetic, respectively. In our bending experiments we observe a strengthening effect, hence a purely dissipation formulation is adopted. The bulk free energy $\Psi$ of the solid will depend upon the elastic strains $\varepsilon^e_{ij}$ but not upon the plastic strains $\varepsilon^p_{ij}$ and the plastic strain gradients $\varepsilon^p_{ij,k}$,

$$\Psi\left(\varepsilon^e_{ij}\right) = \frac{1}{2}\varepsilon^e_{ij} C_{ijkl} \varepsilon^e_{kl}. \tag{5.18}$$

Here, $C_{ijkl}$ is the isotropic elastic stiffness tensor. The Cauchy stress can readily be derived as $\sigma_{ij} = \partial\Psi/\partial\varepsilon^e_{ij}$. Regarding plastic dissipation, for both the rate-dependent case and the rate-independent limit, the plastic work rate can be defined as

$$\dot{W}^p = \Sigma \dot{E}^p \tag{5.19}$$

where $\Sigma$ is an effective stress, work-conjugate to a gradient-enhanced effective plastic strain rate

$\dot{E}^p$. The latter is defined phenomenologically as

$$\dot{E}^p = \left( \frac{2}{3} \dot{\varepsilon}^p_{ij} \dot{\varepsilon}^p_{ij} + \ell^2 \dot{\varepsilon}^p_{ij,k} \dot{\varepsilon}^p_{ij,k} \right)^{1/2} \tag{5.20}$$

where $\ell$ is the material length scale, of dissipative nature. Upon noting that

$$\delta \dot{W}^p = \Sigma \delta \dot{E}^p = q_{ij} \delta \dot{\varepsilon}^p_{ij} + \tau_{ijk} \delta \dot{\varepsilon}^p_{ij,k} \tag{5.21}$$

the constitutive relations for the dissipative stress quantities read

$$q_{ij} = \frac{2}{3} \frac{\Sigma}{\dot{E}^p} \dot{\varepsilon}^p_{ij} \quad \text{and} \quad \tau_{ijk} = \frac{\Sigma}{\dot{E}^p} \ell^2 \dot{\varepsilon}^p_{ij,k}. \tag{5.22}$$

The effective stress $\Sigma$ is readily obtained by substitution of (5.22) into (5.20) to give

$$\Sigma = \left( \frac{3}{2} q_{ij} q_{ij} + \frac{1}{\ell^2} \tau_{ijk} \tau_{ijk} \right)^{1/2}. \tag{5.23}$$

***Numerical implementation***

A finite element framework, based upon Gudmundson [64] and Fleck and Willis [67] phenomenological theories, is presented below to model the bending of our nanolaiminate cantilever beam. Gradient plasticity theories are commonly implemented within a rate-dependent setting thus providing computational advantage and avoiding complications with identifying active plastic zones in time independent models. The viscoplasticity law by Panteghini and Bardella [68], allows us to achieve near rate independent solution when $\dot{\varepsilon}_0$ is very close to zero. The viscoplastic function $V(\dot{E}^p)$ is defined as

$$V(\dot{E}^p) = \begin{cases} \dot{E}^p / (2\dot{\varepsilon}_0), & \text{if } \dot{E}^p / \dot{\varepsilon}_0 \leq 1 \\ 1 - \dot{\varepsilon}_0 / (2\dot{E}^p), & \text{if } \dot{E}^p / (\dot{\varepsilon}_0) > 1. \end{cases} \tag{5.24}$$

The effective flow resistance can be expressed in terms of the gradient-enhanced effective plastic flow rate through a viscoplastic function,

$$\Sigma = \sigma_f(E^p)V(\dot{E}^p). \tag{5.25}$$

The current flow stress $\sigma_f$ in the above equation depends on initial yield stress $\sigma_y$ and $E^p$ on via isotropic hardening law,

$$\sigma_f = \sigma_y \left(1 + \frac{EE^p}{\sigma_y}\right)^N \tag{5.26}$$

where $E$ in the above equation is the Young's modulus and $N$ is the strain hardening exponent ($0 \leq N \leq 1$).

The finite element scheme takes displacement and plastic strain as kinematic variables. The displacement field $u_i$ at position $\mathbf{x}$ is written in terms of the shape functions $N_i^n$ and associated nodal displacements $U^n$, where n denotes the degree of freedom, such that

$$u_i = \sum_{(n=i)}^{D_u} N_i^n U^n. \tag{5.27}$$

Here, $D_u$ is the total number of degrees of freedom for the nodal displacements. Similarly, the plastic strain field $\varepsilon_{ij}^p$ is expressed in terms of the shape functions $M_{ij}^n$ and associated nodal quantities $\varepsilon_p^n$ as

$$\varepsilon_{ij}^p = \sum_{(n=i)}^{D_{\varepsilon_p}} M_{ij}^n \varepsilon_p^n \tag{5.28}$$

where $D_{\varepsilon_p}$ denotes the total number of degrees of freedom for the nodal plastic strain components. Quadratic shape functions are employed for interpolation of both displacements and plastic strains. Accordingly, the plastic strain gradient $\varepsilon_{ij,k}^p$ and total strain $\varepsilon_{ij}$ are computed from nodal plastic strains and displacement through associated gradient matrix $M_{ij}^n$ and the strain-displacement matrix $B_{ij}^n$, respectively.

The non-linear system of equations is solved iteratively by the Newton–Raphson method from

time step $t$ to $(t + \Delta t)$

$$\begin{bmatrix} u \\ \varepsilon_p \end{bmatrix}_{t+\Delta t} = \begin{bmatrix} u \\ \varepsilon_p \end{bmatrix}_t - \begin{bmatrix} K_{u,u} & K_{u,\varepsilon^p} \\ K_{\varepsilon^p,u} & K_{\varepsilon^p,\varepsilon^p} \end{bmatrix}_t^{-1} \begin{bmatrix} R_u \\ R_{\varepsilon^p} \end{bmatrix}_t \tag{5.29}$$

where the residuals comprise the out-of-balance forces,

$$R_u^n = \int_V \sigma_{ij} B_{ij}^n \, dV - \int_S T_i N_i^n \, dS \tag{5.30}$$

$$R_{\varepsilon^p}^n = \int_V \left[ (q_{ij} - \sigma'_{ij}) M_{ij}^n + \tau_{ijk} M_{ij,k}^n \right] dV - \int_S t_{ij} M_{ij,k}^n \, dS. \tag{5.31}$$

### 5.3.3 Problem Formulation

A numerical study of graphene's role in enhancing the strength of Cu nanolaminates was performed using the commercial finite element code: ABAQUS [51]. Gudmundson's higher-order theory [64], implemented as a user element (UEL) subroutine in ABAQUS, is used to model the strain gradient effect seen in our experiments [65]. The simulation model is considered to be adiabatic, and the materials are not subjected to body forces. The simulation model assumes plane strain, rate-independent isotropic elasto-plastic behavior with no volumetric plastic strain.

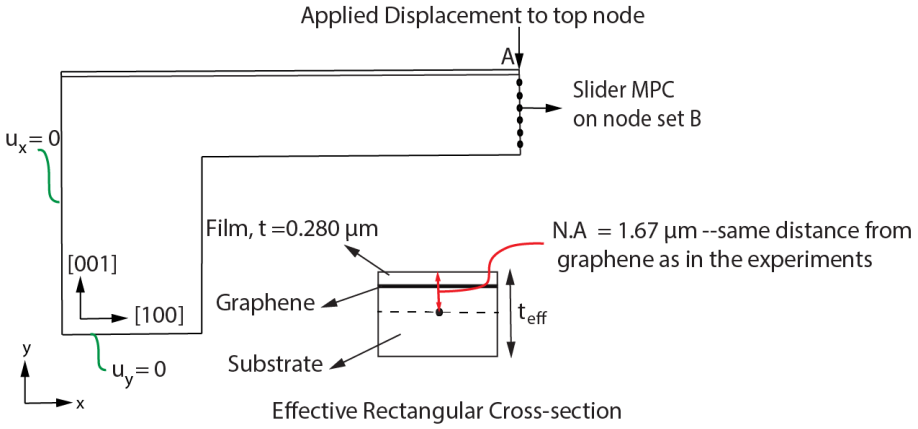


Figure 5.11: Schematic detailing the boundary conditions applied during bending test of Cu-Gr-Cu cantilever beam in strain gradient plasticity simulations.

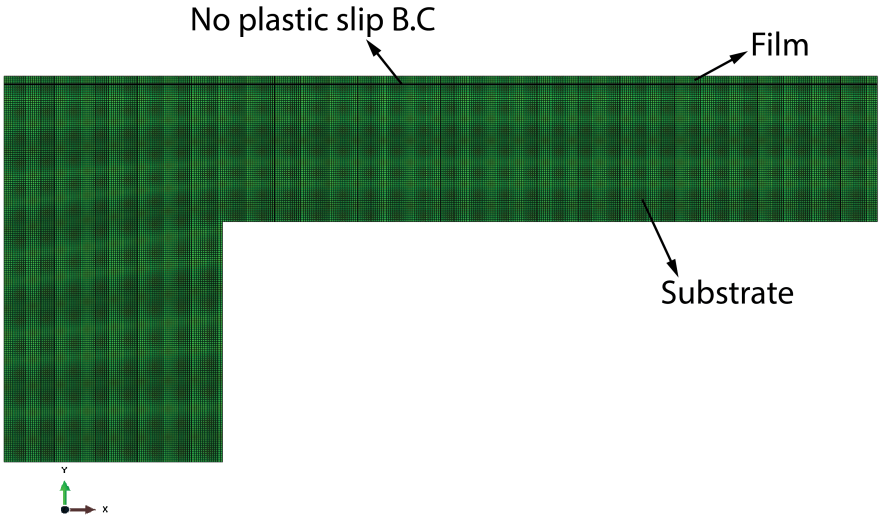


Figure 5.12: Overall mesh showing no plastic slip constrain at Cu/Gr interface.

The dimensions of the cantilever beam and the loading configuration used in the two-dimensional numerical analysis are shown in the Fig. 5.11. The cantilever beam in the numerical study has an effective rectangular cross-section instead of the pentagonal cross-section fabricated in our experiments. The effective thickness of the beam is calculated such that the neutral axis is the same distance below graphene as in the experiments. The effective thickness of the beam is $t_{eff} = 3.497\,\mu m$. The length of the beam is $15\,\mu m$. The width of the beam is taken to be $3\,\mu m$. Since the user subroutine only allows the element to be of unit thickness, the force (output variable) was multiplied by 3 to account for the width of the beam. The calculated effective flexural rigidity for two-dimensional Cu-Cu and Cu-Gr-Cu cantilever beams are $798.62\,mN\mu m^2$ and $800.6\,mN\mu m^2$ respectively.

A vertical displacement of 700 nm is applied to the top node A to deflect the beam. Slider Multi-Point Constraints (MPC) are implemented on the free-end node-set B to ensure that the initial planar cross-section remains planar with deformation. A portion of the nanolaminate (rectangular elastic support) attached to the cantilever beam is modeled to permit deformations. The vertical displacement at the bottom of the rectangular support is zero, while the left edge of the rectangular support has zero displacements in the x-direction.

One of the advantages of using a higher-order SGP model is prescribing boundary conditions on the plastic strains. Since, we assume plane strain condition, the plastic strain in the out-of-plane direction is constrained for the whole model, i.e, $\varepsilon^p_{13} = \varepsilon^p_{23} = \varepsilon^p_{33} = 0$. The SGP model assumes isotropic plasticity.

In an FCC crystal, 12 possible slip system exists: $\{1\,1\,1\}\ \langle 1\,1\,0\rangle$. On applying a load to a single crystal, shearing occurs on the slip system subjected to the largest resolved shear stress. The resolved shear stress acting on the $k^{th}$ slip system can be computed from the Cauchy stress $\sigma_{ij}$,

$$\tau^{(k)} = \mu^{(k)}_{ij}\sigma_{ij}. \tag{5.32}$$

Here, $\tau^{(k)}$ is the resolved shear stress acting on $k^{th}$ slip system and $\mu^{(k)}_{ij}$ is the Schmid tensor given

by:

$$\mu_{ij}^{(k)} = \frac{1}{2}(s_i^{(k)} n_j^{(k)} + s_j^{(k)} n_i^{(k)}) \tag{5.33}$$

where $n^{(k)}$ and $s^{(k)}$ are the slip plane normal and slip direction respectively.

Slip on a system initiates when the resolved shear stress exceeds the strength of the slip system. The single-crystal Cu substrate cantilever beam has the longitudinal axis oriented along the [1 0 0] direction and the top surface corresponding to (0 0 1) plane. Hence, due to the symmetries of the problem and the plane strain plastic deformation, 4 slip systems have equal magnitude of resolved shear stress: (1 1 1) [1 $\bar{1}$ 0], (1 $\bar{1}$ 1) [1 1 0], (1 $\bar{1}$ $\bar{1}$) [1 1 0], (1 1 $\bar{1}$) [1 $\bar{1}$ 0]. The resolved shear stress acting on these slip systems are calculated using Eq. 5.32:

$$\tau^{(k)} = \frac{\sigma_{11} - \sigma_{22}}{\sqrt{6}}. \tag{5.34}$$

The 4 active slip systems act at ±45° to the bottom edge of the cantilever beam ( or [1 0 0] direction). It is interesting to note that slip systems (1 1 1) [1 $\bar{1}$ 0] and (1 1 $\bar{1}$) [1 $\bar{1}$ 0] have the same resolved shear stress and slip direction. Similarly, slip systems (1 $\bar{1}$ 1) [1 1 0] and (1 $\bar{1}$ $\bar{1}$) [1 1 0] exhibit the same resolved shear stress and slip direction. This introduces plane strain deformation in the cantilever beam. Furthermore, appendix D shows that the other 8 slip systems can not be combined in any way to obtain a plain strain deformation.

Assuming all four slip systems are activated in equal amounts of slip, $\gamma$, the plastic strain tensor is,

$$\varepsilon_{ij}^{p} = \begin{bmatrix} 2\frac{\sqrt{2}}{\sqrt{3}}(\gamma) & 0 & 0 \\ 0 & -2\frac{\sqrt{2}}{\sqrt{3}}(\gamma) & 0 \\ 0 & 0 & 0 \end{bmatrix}. \tag{5.35}$$

Since the $\varepsilon_{12}^{p}$ in Eqn. 5.35 is zero, the plastic strain $\varepsilon_{12}^{p}$ for the Cu substrate is set to zero in the SGP model. Appendix D provides more details on the calculation of resolved shear stress in the single-crystal Cu substrate and the resulting plastic strain.

Change in volume can be determined from $trace(\varepsilon_p)$. From Eqn. 5.35, $trace(\varepsilon_p = 0)$, i.e,

there is no volumetric plastic strain hence, $\varepsilon^p_{11} = -\varepsilon^p_{22}$ is prescribed as a kinematic boundary condition to the entire domain in the SGP simulation.

The enhancement in strength seen in Cu-Gr-Cu nanolaminate suggests a build-up of dislocations at the Cu-Gr interface, limiting the plastic slip that can occur at the Cu/Gr interface. Hence, to mimic the presence of the graphene in Cu-Gr-Cu cantilever beam simulations, a zero plastic strain boundary condition, i.e., $\varepsilon^p_{11} = \varepsilon^p_{22} = \varepsilon^p_{12} = 0$ is enforced at the Cu-Gr interfaces.

The nanolaminate cantilever beam has a uniform mesh of 39600 elements (Fig. 5.12).

Table. 5.2 details a set of material parameters identified to reproduce the experimental force vs. displacement results for both the Cu-Cu and the Cu-Gr-Cu nanolaminate. The Young's modulus for the Cu film calculated from nanoindentation measurements is 107.8 GPa. The Young's modulus of Cu substrate, calculated from elastic constants, is equal to 66.7 GPa. A Poisson's ratio of 0.3 was set for both the Cu film and Cu substrate.

| **Material Properties** | **Film** | **Substrate** |
|---|---|---|
| Young's modulus (GPa) | 107.8 | 66.7 |
| Yield Stress (MPa) | 60 | 40 |
| $\ell$ (μm) | 1 | 2 |
| Strain Hardening Exponent | 0.1 | 0.06 |

Table 5.2: Summary of Material Properties Used in Strain Gradient Plasticity Simulations.

The yield point is determined by the yield stress and the dissipative length scale $l$. The yield stress of 40 MPa [69] and a corresponding $l = 2$ μm were ascertained to model the yield behavior of the Cu substrate. A strain hardening exponent of 0.06 was chosen for the Cu substrate. Since the Cu film is nanocrystalline in nature, a higher yield stress of 60 MPa and a corresponding $l = 1$ μm were determined to model yield behavior of the Cu Film. Consequently, a strain hardening exponent of 0.1 was chosen to model the Cu film. This set of material property for the Cu film is not unique. An yield stress of 40 MPa, a $l = 2$ μm, and a strain hardening exponent of 0.06 can also be assigned to the Cu film to reproduce the experimental force-displacement response of the cantilever beam.

The SGP simulations for Cu-Cu and Cu-Gr-Cu were performed with the same set of material

properties. The only difference in the simulations was the zero plastic strain boundary conditions that were enforced at the Cu-Gr interfaces in the Cu-Gr-Cu nanolaminate.

Discretization errors occur from representing the governing equations and physical models as algebraic expressions in a discrete space and time domain. The temporal discreteness is manifested through the time step taken while mesh size determines the discrete spatial domain. Therefore, it is essential to examine the sensitivity of the simulation results to the magnitude of the time increments and the mesh size. Implicit analysis is unconditionally stable hence not sensitive to the size of the time increment. As the mesh is refined, the solution becomes less sensitive to the mesh size and approaches the continuum solution.

Spatial convergence were performed to ensure minimum discretization error. The analysis was rerun by refining the mesh size by 25%. The numerical study did not show any sensitivity to the mesh size.

### 5.3.4 Analysis Results

Strain gradient plasticity simulations were performed using ABAQUS as described in section. 5.3.3. The normalized force-displacement behavior shown in Fig. 5.13 compares the simulations and experimental beam bending results for both Cu-Gr-Cu and Cu-Cu nanolaminates. The numerical results are in excellent agreement with the experiments.

Fig. 5.14(a) and Fig. 5.14(b) compares the distribution of transverse plastic strain ($\varepsilon_{p_{11}}$) for Cu-Cu and Cu-Gr-Cu nanolaminates. Both Fig. 5.14(a) and Fig. 5.14(b) have same contour limits. The contours suggests that the plastic deformation in Cu-Gr-Cu is predominately compression and is confined in the Cu substrate, consistent with graphene inhibiting dislocation motion across the Cu/Gr interface. In comparison, the plastic deformation in the Cu-Cu cantilever beam is predominantly tension. Plastic strain, $\varepsilon_{p_{11}}$, was chosen because according to Euler beam theory, $\sigma_{11}$ is the dominant stress in the beam.

Fig. 5.15(b) presents the strain $\varepsilon^p_{11}$ contour for Cu-Gr-Cu nanolaminate cantilever beam using a different set of contour limits. Suppression of plastic strain is seen at the Cu/Gr interface. The

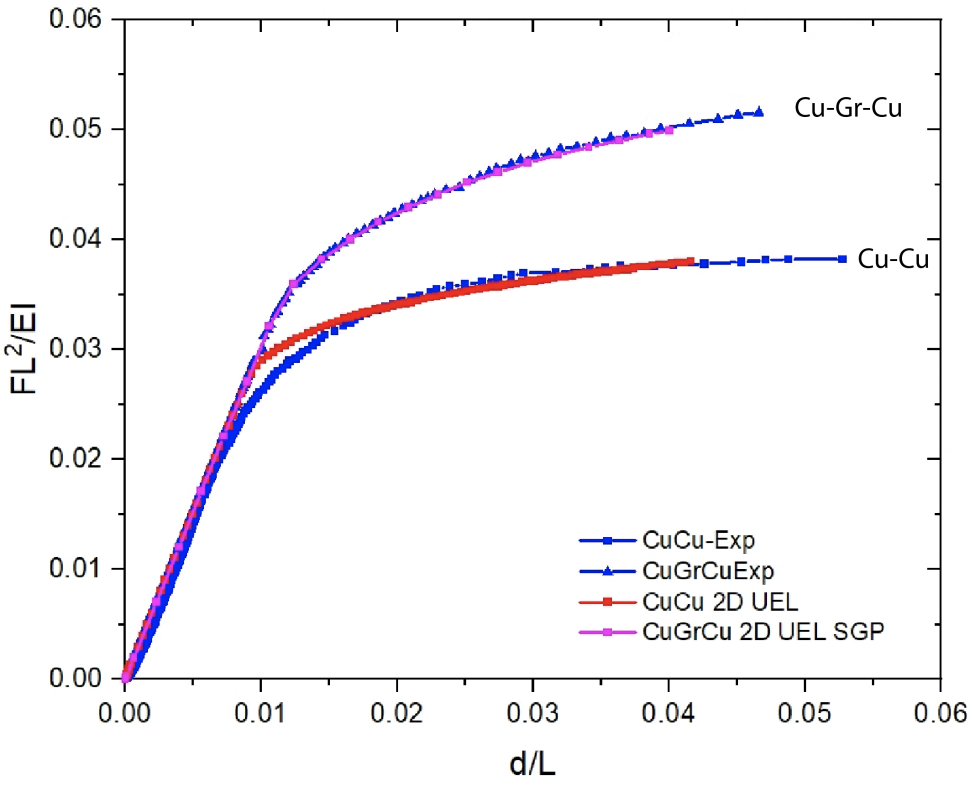


Figure 5.13: Comparison of load-displacement curves obtained from simulations to that from experiments.

presence of graphene effectively reduces the tensile strain at the top of the beam, thus causing the deformation to be compression dominated in Cu-Gr-Cu nanolaminate compared to the deformation being tensile dominated in Cu-Cu nanolaminate. Fig. 5.15(c) shows the strain $\varepsilon_{11}^{p}$ across the beam thickness. It is evident that a boundary layer with zero plastic strain exists near the Cu/Gr interface. The zero plastic strain boundary layer is absent in Cu-Cu nanolaminate.

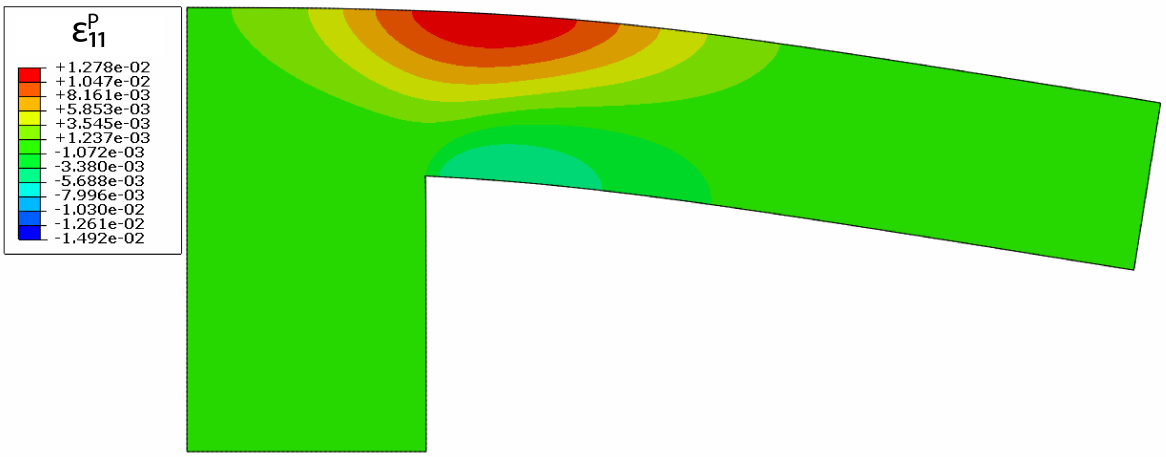


(a)

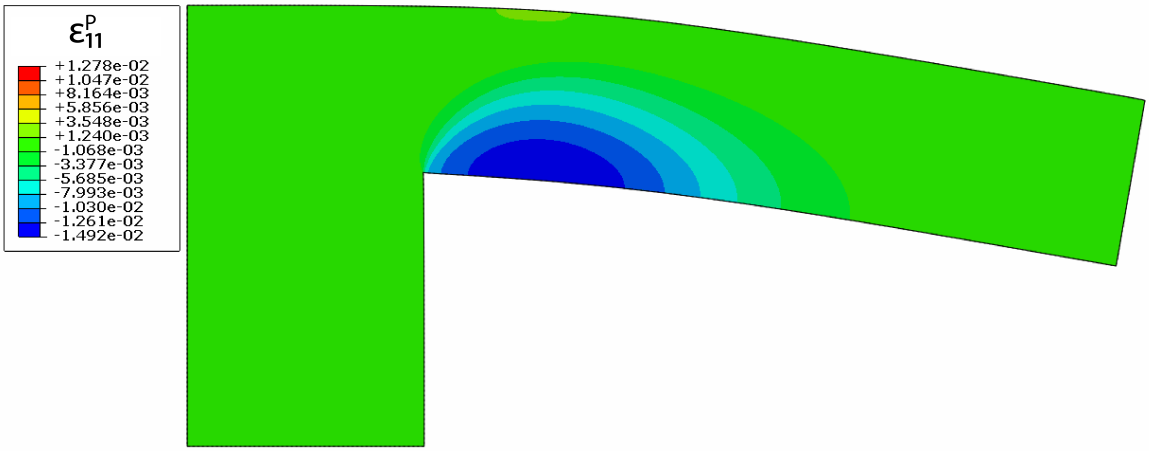


(b)

Figure 5.14: Plastic strain contour $\varepsilon_{p_{11}}$ (a) Cu-Cu, (b) Cu-Gr-Cu. Both figures have the same contour limits.

Fig. 5.16(a) and (b) presents the distribution of plastic strain gradient for Cu-Gr-Cu nanolaminate cantilever beam. In Cu-Cu nanolaminate (Fig. 5.16(a)), as expected, most of the plastic strain gradients emanate from the lower beam corner. While in Cu-Gr-Cu nanolaminate, large plastic strain gradients are also observed near the Cu/Gr interface. Fig. 5.16(c) plots the plastic strain gradient across the beam thickness. A boundary layer with a large plastic strain gradient exists at the Cu/Gr interface. This boundary layer is absent in Cu-Cu nanolaminate and forms naturally in Cu-Gr-Cu nanolaminate.

Graphene's ability to act as a barrier for dislocation motion is consistent with our strain gra-

dient plasticity simulations. The computational model assumes that the plastic flow is completely suppressed at the Cu/Gr interface. The identified material properties (table. 5.2) capture the increase in flow strength and strain hardening observed in our experiments. Enhancement of flow strength in Cu-Gr-Cu nanolaminate implies the presence of a large density of geometrically necessary dislocations ($\Delta\sigma_f \propto \sqrt{\rho_{GND}}$). The increase in the dislocation density, in turn, suggests the presence of large plastic strain gradients [70].

$$\rho_{GND} b = -\nabla\gamma \cdot \mathbf{s}. \tag{5.36}$$

The SGP simulation for Cu-Gr-Cu nanolaminate confirms the presence of a boundary layer with large plastic strain gradients near the Cu/Gr interface (Fig. 5.16(b)). This boundary layer is absent in Cu-Cu nanolaminate and forms naturally in Cu-Gr-Cu nanolaminate as graphene prevents dislocations from propagating across the interface leading to a dislocation pile up at the Cu/Gr interface.

Our SGP explanation is consistent with discrete dislocation simulations of a thin-film with one or more passivation layers [71] [23]. Nicola et al. [71] performed discrete dislocation simulations on unpassivated, one side passivated, and both sides passivated thin Cu films. They reported that the flow strength and the strain hardening increased with an increasing number of passivation layers. The discrete dislocation simulations indicated that a pile-up of dislocations was present at the passivation/film interface. The distribution of stress in the passivated film showed a higher stress level than the unpassivated film. Similarly, discrete dislocation analysis performed on single-crystal films, which were stressed due to thermal mismatch between the film and the substrate [23], revealed an increase in strain hardening due to a reduction in dislocation nucleation caused by the back stress associated with the dislocation pile-ups at the film-substrate interface.

In summary, we report a microstructure design of Cu-Gr-Cu nanolaminate that utilizes the high intrinsic strength of graphene to enhance the strength of the composite. The bending tests performed on fabricated Cu-Gr-Cu nanolaminate cantilever beams exhibit a remarkable strength-

ening effect over a control Cu-Cu nanolaminate cantilever beam. The inclusion of single-layer graphene significantly increases the load required to deflect a Cu-Gr-Cu nanolaminate cantilever compared to the Cu-Cu nanolaminate cantilever. The exceptional strengthening of the composite is attributed to the constraint on dislocation propagation across the Cu/Gr interface and the restriction of plastic slip across the Cu/Gr interface. Our strain gradient plasticity computation model validated the effectiveness of graphene as a barrier to dislocation motion. The same set of material properties were used to replicate the experiment load-displacement curve for both Cu-Cu and Cu-Gr-Cu nanolaminate cantilever beams. The sole difference in the numerical analysis of the two nanolaminate composites was that zero plastic strain boundary conditions were enforced at the Cu-Gr interfaces in the Cu-Gr-Cu nanolaminate.

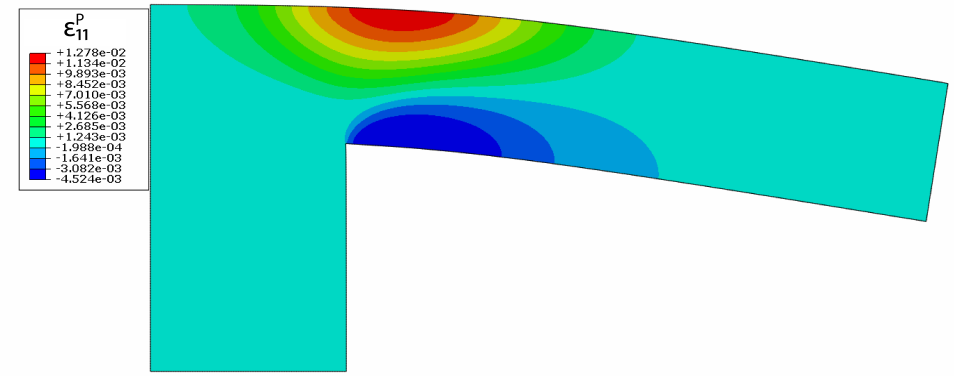


(a)

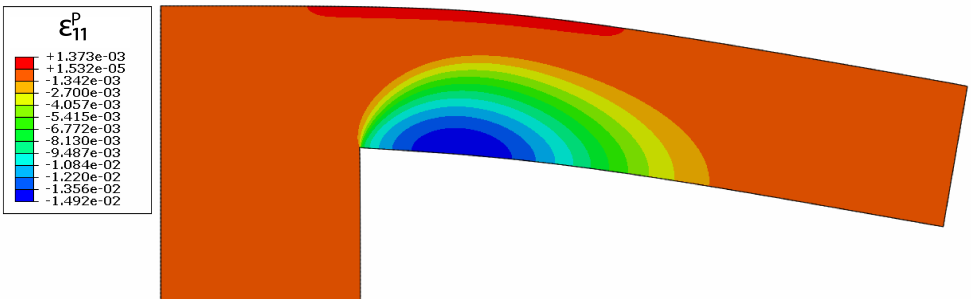


(b)

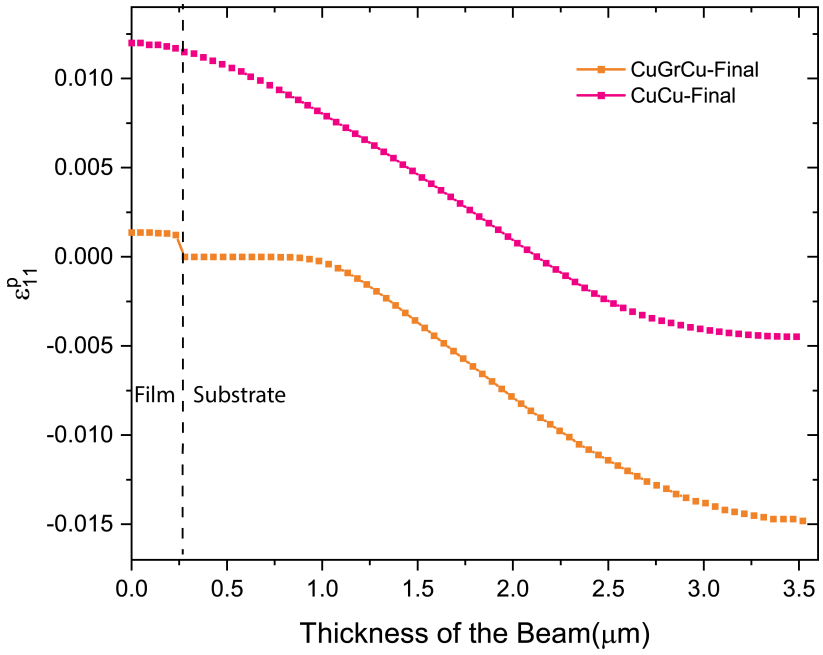


(c)

Figure 5.15: Plastic strain contour for $\varepsilon_{p_{11}}$ for (a) Cu-Cu nanolamiante,(b) Cu-Gr-Cu nanolaminate, (c) Plot comparing variation of $\varepsilon_{p_{11}}$ across beam thickness. Figures (a) and (b) have different contour limits.

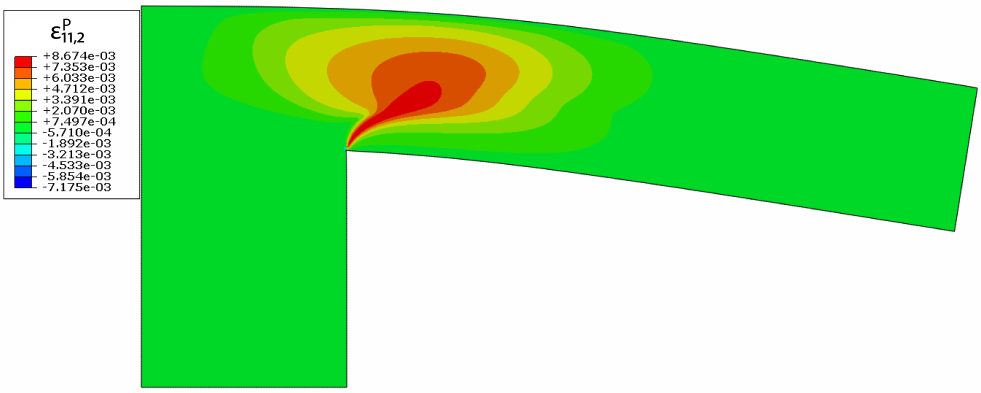


(a)

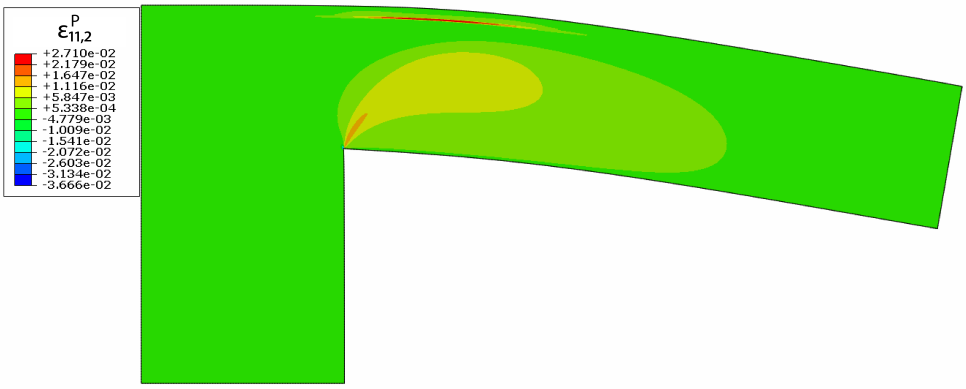


(b)

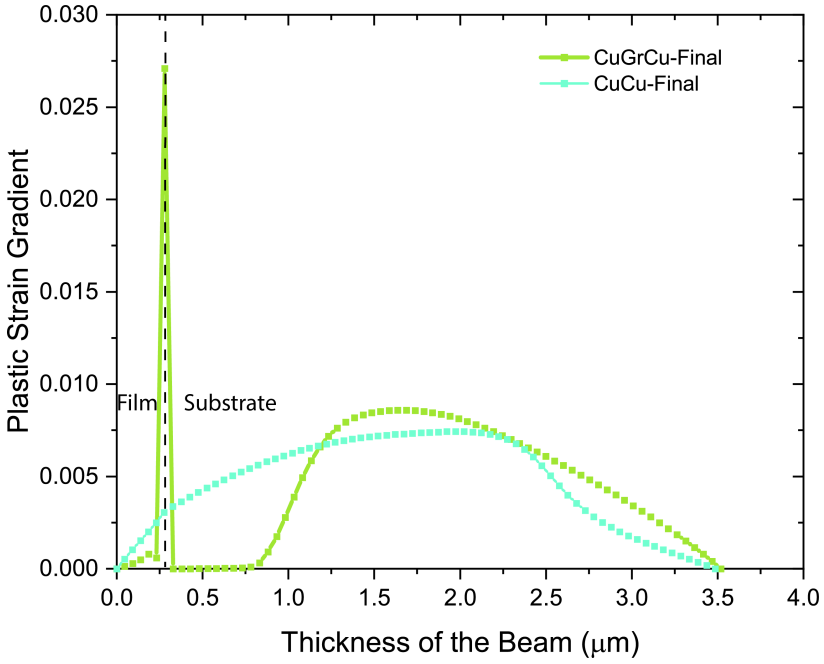


(c)

Figure 5.16: Plastic strain gradient contour in the vertical direction for (a) Cu-Cu nanolamiante, (b) Cu-Gr-Cu nanolaminate, (c) plot comparing variation of plastic strain gradient across beam thickness.

# Chapter 6: Conclusion

## 6.1 Summary of Contributions

This thesis evaluates the microstructure design of Cu-graphene nanolaminates, comprising of alternate layers of Cu and chemical vapor deposition (CVD) graphene to enhance the load-bearing capacity, strength, and frictional behavior of Cu-graphene nanocomposite. In doing so, we have utilized the key advantages of graphene – its ultra-high-strength, modulus, and 2D geometry. In addition, by choosing a nanolaminate structure, we have allowed for uniform and controlled placement of graphene within the metal matrix. Previous studies focused on synthesizing simple mixtures of graphene flakes in a metal matrix, leading to insufficient, non-uniform dispersion of graphene flakes within the metal matrix. By incorporating graphene in the Cu-metal nanolayered system, we have designed a composite with a strength that is a factor of two to three higher than the rule-of-mixtures estimate.

In this thesis, we have used various micromechanical testing methods to understand the mechanical properties of Cu-Gr-Cu nanolaminates. The findings of this thesis are summarized below:

- ***Fabrication of Cu-Gr-Cu nanocomposite***: We employed an industrially scalable and transfer free process to synthesize Cu-Gr-Cu nanolaminate. A continuous monolayer of high-quality graphene was grown on an electropolished high purity Cu substrate. A layer of Cu film was then deposited via physical vapor deposition on the grown graphene to synthesize the Cu-Gr-Cu nanolaminate.

- ***Increased load bearing capacity of Cu-Gr-Cu nanolaminate***: We measured the mechanical properties of Cu-Gr-Cu nanolaminate using nanoindentation. The addition of single-layer graphene significantly enhanced the effective Young's modulus and the effective flow

strength of the Cu-Gr-Cu nanolaminate by 20% and 47% respectively when compared to Cu-Cu nanolaminate. The remarkable increase in the strength of the composite is consistent with graphene's ability to constraint dislocation propagation across the Cu-graphene interface, thus limiting plastic deformation to the Cu film. Our FEA simulations confirmed the effectiveness of graphene as a barrier to plastic deformation. These simulations revealed an increase in plastic energy dissipated in Cu film due to the presence of graphene in Cu-Gr-Cu nanolaminates. Moreover, a significant reduction in plastic deformation is observed in the Cu substrate just below graphene. The flow strength calculated in our nanoindentation experiments are consistent with results from the literature [24]. Fig. 6.1 compares the strength of Cu/Gr nanolaminate from nanopillar compression test to the reported strengths of nanolaminates with similar metal layer spacing. The strength of Cu/Gr nanolaminate is higher than the reported strength of most Cu based nanolaminates in the literature. Cu-Cr nanolaminate has slightly higher strength compared to Cu-Gr nanolaminates. Chromium is a very hard but is also brittle, hence at very large loads can fail at catastrophically. Graphene on the other hand has very high strength and can withstand high loads thus behaving like a strength enhancer even at large strains.

- ***Enhanced Strength of Cu-Gr-Cu nanolaminate***: Bending tests of Cu-Gr-Cu nanolaminate cantilever beams revealed that a single atomic layer of graphene enhances the strength of the Cu nanolaminate. We found that the inclusion of graphene increased the flow strength of Cu-Gr-Cu nanolaminate compared to Cu-Cu nanolaminate. In addition, an increased degree of strain hardening was observed in Cu-Gr-Cu nanolaminates. These findings suggest that graphene's high intrinsic mechanical strength provided an effective barrier against dislocation motion. The strain gradient plasticity (SGP) computational model is employed to replicate the load-displacement behavior of the nanolaminates. The computational model assumed that the plastic flow is completely suppressed at the Cu/Gr interface. The identified material properties captured the increase in flow strength and strain hardening observed in our experiments. The SGP simulation for Cu-Gr-Cu nanolaminate confirmed the presence

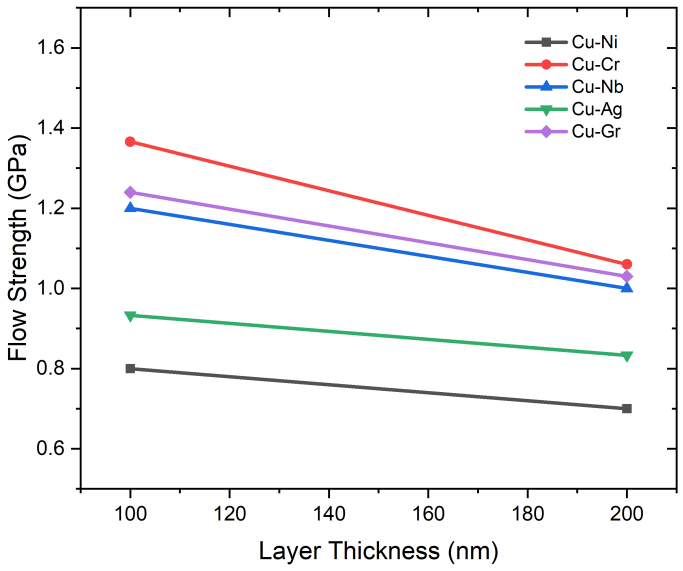


Figure 6.1: Comparing the strength of Cu/Gr nanolaminate with other Cu-X multi-layer composites [22]. Here X is Ni, Cr, Nb, Ag.

of a boundary layer with large plastic strain gradients near the Cu/Gr interface (Fig. 5.16). This boundary layer was absent in Cu-Cu nanolaminate and formed naturally in Cu-Gr-Cu nanolaminate as graphene prevented dislocations from propagating across the interface leading to a dislocation pile up at the Cu/Gr interface.

- ***Improvement in Frictional Properties of Cu-Gr-Cu nanocomposite***: We performed a series of scratch tests on the nanolaminate microstructure design of Cu-Gr-Cu. The presence of single-layer graphene reduced the measured frictional force and the coefficient of friction (CoF) of the composite by 33%. The decrease in CoF of the composite was due to graphene's ability to constrain dislocation propagation across the Cu/Gr interface. In addition, our FEA study showed that the plastic strain/deformation was significantly lower in Cu-Gr-Cu nanolaminate than in Cu-Cu nanolaminate. However, our current model was not able to capture the influence of graphene on CoF.

## 6.2 Future Work

The work presented in this thesis has given us insight into the strengthening and frictional properties of graphene in Cu-Gr-Cu nanolaminates. It has laid the foundation for us to explore the influence of graphene on other mechanical properties such as shear strength and fracture toughness of Cu-Gr-Cu nanolaminate.

- ***Mechanical Behavior of Cu-Gr-Cu Under Shear Loading***

  The influence of graphene when the Cu-Gr-Cu nanolaminate is subjected to shear loading can be characterized using a microscale double notch geometry shown in Fig. 6.2. First, the double notch shear pillars are fabricated using a dual-beam SEM-FIB. A flat punch indenter is then used to compress the double notched pillar causing the longitudinal plane between the notches to be in pure shear. The displacement can be applied either perpendicular to nanolaminate layers or parallel to the nanolaminate layers. The shear stress vs. shear strain curves will give an insight into the shear strength of Cu-Gr-Cu nanolaminate.

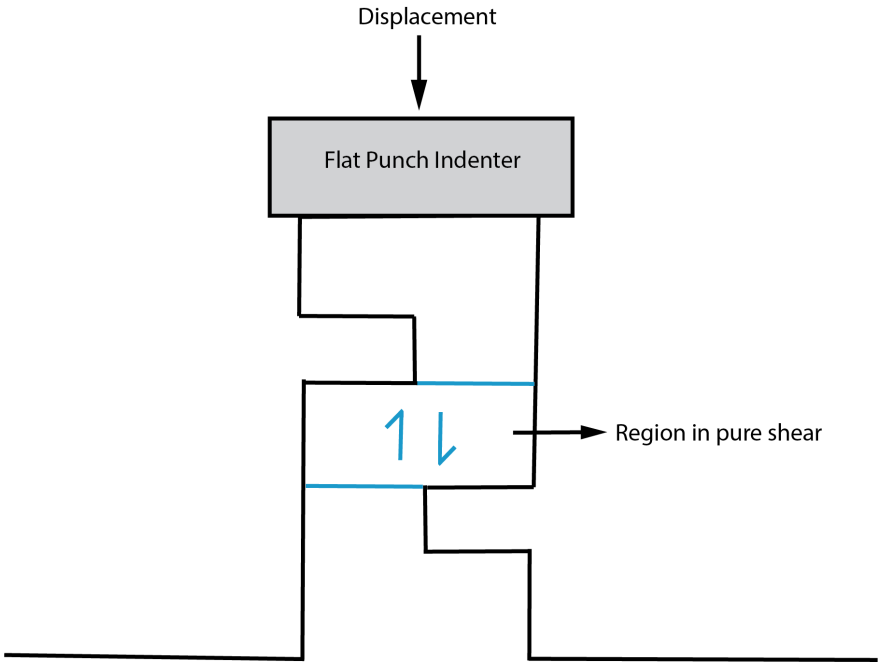


Figure 6.2: Schematic of double notch geometry.

- ***Micropillar Compression Test with Graphene at Different Orientation***

  The orientation of nanolaminate layers with respect to the loading axis impacts the mechanical behavior of nanolaminates. The anisotropy in mechanical behavior is characterized by using a micropillar compression test. Three orientations, with the loading axis forming 45°, 30°, and 15°with respect to the loading axis, are chosen to characterize the anisotropy in the mechanical behavior of Cu-Gr-Cu nanolaminate using pillar compression. Images of the micropillars after compression test combined with FEA numerical analysis can give us insight into the deformation behavior/mechanism of Cu-Gr-Cu nanolaminates.

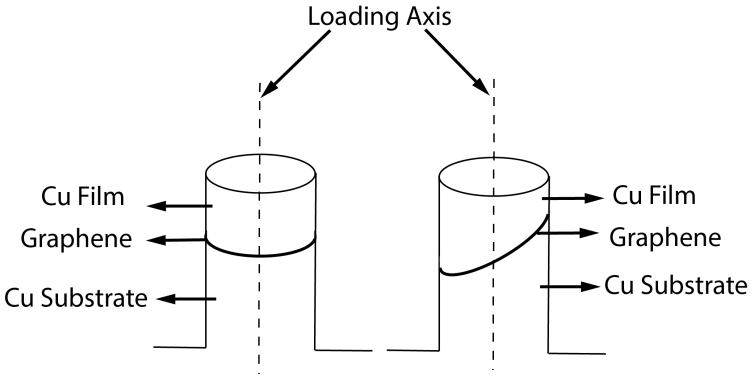


Figure 6.3: Schematic of micropillar compression test.

- ***Fracture Toughness of Cu-Gr-Cu nanolaminate***

  The fracture toughness of Cu-Gr-Cu nanolaminates is characterized using micro-cantilever beams. The cantilever beams are fabricated using a dual-beam FIB/SEM. Line milling is used to cut the notches (Fig. 6.4). The cantilever beam is deflected at a constant displacement rate using a Berkovich tip until the beam fractures. We can define *fracture* as a significant jump in displacement between data points. An FEA model can be used to replicate the experiment load-displacement curve and calculate the fracture toughness of Cu-Gr-Cu.

- ***Fabricating Multiple Layer Cu/Gr nanolaminate***

  In chapter 2 we demonstrated a transfer-free process to synthesize Cu-Gr-Cu nanolaminate. An attempt was made to apply the transfer-free design to synthesize multiple layers of Cu-

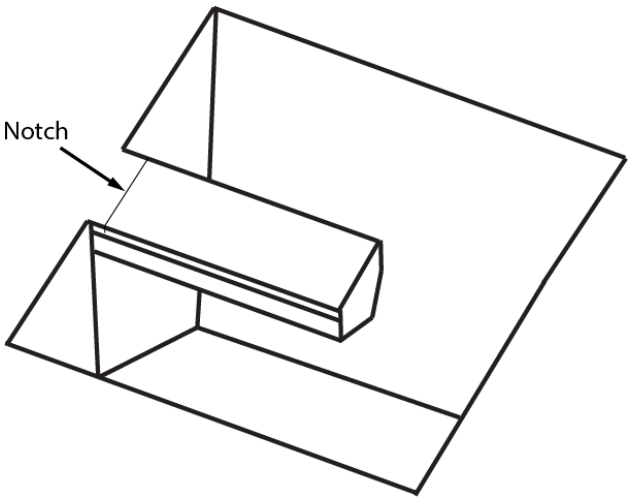


Figure 6.4: Schematic of Cantilever Beam with notch.

Gr nanolaminates using an atmospheric pressure CVD system. We chose to grow graphene at atmospheric pressure to minimize the sublimation of Cu films at 1000°C. The first layer of graphene was grown on the Cu substrate at atmospheric pressure, and 1000°C. Cu film of 700 nm was deposited on the grown graphene. The Cu-Gr-Cu nanolaminate was then placed in an atmospheric pressure CVD furnace to grow the second layer of graphene on the Cu film. However, graphene was not stable at 1000°C, hence the first layer of graphene (sandwiched between the Cu substrate and Cu film) disappeared while growing the second layer of graphene on the Cu film.

Now, with the lab equipped with the ability to grow high-quality graphene in ultra-high purity low-pressure CVD system at 840°C in 5 min, we can synthesize Cu/Gr nanolaminate with multiple layers of Cu and graphene. The strength, frictional behavior, and fracture toughness can be characterized with respect to the number of layers, Cu film thickness, and laminate layer orientation.

- ***Push towards Industrially Scalable Systhesis***

  The physical vapor deposition technique is not conducive to producing Cu/Gr nanolaminates at an industrial scale. Electroless deposition is a more viable alternative to deposit Cu films onto graphene. Initial attempts to deposit Cu film onto graphene via electroless deposition

have shown promising results. The quality of graphene did not deteriorate as it was immersed into various chemical solutions before being immersed into the final Cu bath. Preliminary nanoindentation results have confirmed the strengthening effect of graphene in Cu-Gr-Cu nanolaminates synthesized via electroless deposition.

# BIBLIOGRAPHY


(1) K. S. Kim, Y. Zhao, H. Jang, S. Y. Lee, J. M. Kim, K. S. Kim, J.-H. Ahn, P. Kim, J.-Y. Choi and B. H. Hong, *Nature*, 2009, **457**, 706–710.

(2) Y. D. Kim, H. Kim, Y. Cho, J. H. Ryoo, C. H. Park, P. Kim, Y. S. Kim, S. Lee, Y. Li, S. N. Park, Y. Shim Yoo, D. Yoon, V. E. Dorgan, E. Pop, T. F. Heinz, J. Hone, S. H. Chun, H. Cheong, S. W. Lee, M. H. Bae and Y. D. Park, *Nat. Nanotechnology*, 2015, **10**, 676–681.

(3) N. Wang, M. K. Samani, H. Li, L. Dong, Z. Zhang, P. Su, S. Chen, J. Chen, S. Huang, G. Yuan, X. Xu, B. Li, K. Leifer, L. Ye and J. Liu, *Small*, 2018, **14**, 1–8.

(4) C. Lee, X. Wei, J. W. Kysar and J. Hone, *Science (80-. ).*, 2008, **321**, 385–388.

(5) X. Wei and J. W. Kysar, *Int. J. Solids Struct.*, 2012, **49**, 3201–3209.

(6) G.-h. Lee, R. C. Cooper, S. J. An, S. Lee, A. V. Der, N. Petrone, A. G. Hammerberg, C. Lee, B. Crawford, W. Oliver, J. W. Kysar, J. Hone, N. Petrone, A. G. Hammerberg, C. Lee and B. Crawford, 2013, **340**.

(7) P. Blake, P. D. Brimicombe, R. R. Nair, T. J. Booth, D. Jiang, F. Schedin, L. A. Ponomarenko, S. V. Morozov, H. F. Gleeson, E. W. Hill, A. K. Geim and K. S. Novoselov, *Nano Lett.*, 2008, **8**, 1704–1708.

(8) S. GF, K. SW, C. VE, P. G, Z. HW, V. LM and D. C, *Nano Lett.*, 2010, **10**, 3163–3167.

(9) A. Kapito, R. J. Mostert, W. E. Stumpf and C. W. Siyasiya, *IOP Conf. Ser. Mater. Sci. Eng.*, 2019, **655**.

(10) W. D. Callister Jr. and D. G. Rethwisch, Material Science and Engineering - An Introduction, 8th, 2009.

(11) A. A. Griffits, *Philos. Trans. R. Soc. london. Ser. A, Contain. Pap. a Math. or Phys. character,* 1921, **221**, 163–198.

(12) X. Wei, B. Fragneaud, C. A. Marianetti and J. W. Kysar, *Phys. Rev. B - Condens. Matter Mater. Phys.*, 2009, **80**, 1–8.

(13) R. Grantab, V. B. Shenoy and R. S. Ruoff, 2017, **330**, 946–948.

(14) A. Zandiatashbar, G. H. Lee, S. J. An, S. Lee, N. Mathew, M. Terrones, T. Hayashi, C. R. Picu, J. Hone and N. Koratkar, *Nat. Commun.*, 2014, **5**, 1–9.

(15) B. M. Clemens, H. Kung and S. A. Barnett, *MRS Bull.*, 1999, **24**, 20–26.

(16) G. S. Was and T. Foecke, *Thin Solid Films*, 1996, **286**, 1–31.

(17) A. Misra, J. P. Hirth and H. Kunc, *Philos. Mag. A Phys. Condens. Matter, Struct. Defects Mech. Prop.*, 2002, **82**, 2935–2951.

(18) A. Misra and H. Kung, *Adv. Eng. Mater.*, 2001, **3**, 217–222.

(19) N. A. Mara, D. Bhattacharyya, P. Dickerson, R. G. Hoagland and A. Misra, *Appl. Phys. Lett.*, 2008, **92**.

(20) R. Oberle and R. Cammarata, *Saipta Metall. Mater.*, 1995, **32**, 583–588.

(21) J.S.Koehler, *Phys. Rev. B*, 1970, **2**.

(22) A. MISRA, *Nanostructure Control Mater.*, 2006, 146–176.

(23) L. Nicola, Y. Xiang, J. J. Vlassak, E. Van der Giessen and A. Needleman, *J. Mech. Phys. Solids*, 2006, **54**, 2089–2110.

(24) Y. Kim, J. Lee, M. S. Yeom, J. W. Shin, H. Kim, Y. Cui, J. W. Kysar, J. Hone, Y. Jung, S. Jeon and S. M. Han, *Nat. Commun.*, 2013, **4**, 1–7.

(25) B. Hwang, W. Kim, J. Kim, S. Lee, S. Lim, S. Kim, S. H. Oh, S. Ryu and S. M. Han, *Nano Lett.*, 2017, **17**, 4740–4745.

(26) N. A. Fleck, G. M. Muller, M. F. Ashby and J. W. Hutchinson, 1994, **42**, 475–487.

(27) N. A. Stelmashenko, M. G. Walls, L. M. Brown and Y. V. Milman, *Acta Metall. Mater.*, 1993, **41**, 2855–2865.

(28) Q. Ma and D. R. Clarke, *J. Mater. Res.*, 1995, **10**, 853–863.

(29) J. W. Hutchinson, *Int. J. Solids Struct.*, 2000, **37**, 225–238.

(30) M. Ashby, *Philosophical Magazine*, 1970, **21**, 475–487.

(31) Y. Xiang and J. J. Vlassak, *Acta Mater.*, 2006, **54**, 5449–5460.

(32) G. Eda and M. Chhowalla, *Nano Lett.*, 2009, **9**, 814–818.

(33) J. D. Fowler, M. J. Allen, V. C. Tung, Y. Yang, R. B. Kaner and B. H. Weiller, *ACS Nano*, 2009, **3**, 301–306.

(34) H. Chi, K. Murali, T. Li and S. Thomas, *Prog. Nat. Sci. Mater. Int.*, 2019, **29**, 603–611.

(35) W. Chen, T. Yang, L. Dong, A. Elmasry, J. Song, N. Deng, A. Elmarakbi, T. Liu, H. B. Lv and Y. Q. Fu, *Nanotechnol. Precis. Eng.*, 2020, **3**, 189–210.

(36) M. Wall, *Thermo Sci.*, 2011, 5.

(37) K. J. Kurzydeowski and J. J. Bucki, *Acta Metall. Mater.*, 1993, **41**, 3141–3146.

(38) S. Berbenni, V. Favier and M. Berveiller, *International Journal of Plasticity*, 2007, **23**, 114–142.

(39) M. Tschopp and D. McDowell, *Scripta Materialia*, 2008, **58**, 299–302.

(40) R. Yuan, I. Beyerlein and C. Zhou, *Sci Rep*, 2016, **6**, 26254.

(41) E. F. Rauch and L. Dupuy, *Arch. Metall. Mater.*, 2005, **50**, 87–99.

(42) W. C. Oliver and G. M. Pharr, *J. Mater. Res.*, 1992, **7**, 1564.

(43) W. Oliver and G. Pharr, *J. Mater. Res.*, 2004, **19**, 3–20.

(44) C. A. Tweedie, V. Vliet and K. J., *J. Mater. Res.*, 2006, **21**, 1576–1589.

(45) A. A. Volinsky, J. B. Vella and W. W. Gerberich, *Thin Solid Films*, 2003, **429**, 201–210.

(46) J. J. Vlassak and W. Nix, *J. Mech. Phys. Solids*, 1994, **42**, 1223–1245.

(47) J. G. Swadener and G. M. Pharr, *Philos. Mag. A*, 2001, **81**, 447–466.

(48) A. Misra, J. P. Hirth and R. G. Hoagland, *Acta Mater.*, 2005, **53**, 4817–4824.

(49) P. M. Anderson and C. Li, *Nanostructured Mater.*, 1995, **5**, 349–362.

(50) A. F. Bower, Applied Mechanics of Solids.

(51) SIMULIA, *ABAQUS 6.7 User's Manual, 6.7-1 ed. ABAQUS Inc., Pawtucket, RI*, 2009.

(52) A. Bolshakov and G. M. Pharr, *J. Mater. Res.*, 1998, **13**, 1049–1058.

(53) R. Al-Jishi and G. Dresselhaus, *Phys. Rev. B*, 1982, **26**, 4514–4522.

(54) C. Lee, Q. Li, W. Kalb, X. Z. Liu, H. Berger, R. W. Carpick and J. Hone, *Science (80-. ).*, 2010, **328**, 76–80.

(55) C. Lee, X. Wei, Q. Li, R. Carpick, J. W. Kysar and J. Hone, *Phys. Status Solidi Basic Res.*, 2009, **246**, 2562–2567.

(56) Q. Li, C. Lee, R. W. Carpick and J. Hone, *Phys. Status Solidi Basic Res.*, 2010, **247**, 2909–2914.

(57) K. S. Kim, H. J. Lee, C. Lee, S. K. Lee, H. Jang, J. H. Ahn, J. H. Kim and H. J. Lee, *ACS Nano*, 2011, **5**, 5107–5114.

(58) D. Berman, S. A. Deshmukh, S. K. Sankaranarayanan, A. Erdemir and A. V. Sumant, *Adv. Funct. Mater.*, 2014, **24**, 6640–6646.

(59) W. Zhai, X. Shi, M. Wang, Z. Xu, J. Yao, S. Song and Y. Wang, *Wear*, 2014, **310**, 33–40.

(60) S. Bellemare, M. Dao and S. Suresh, *Int. J. Solids Struct.*, 2007, **44**, 1970–1989.

(61) Fredrik Wredenberg; Per-Lennart Larsson, 2011, **6**.

(62) Y. Gao and H. M. Urbassek, *Appl. Surf. Sci.*, 2016, **389**, 688–695.

(63) Y. Huang, *Mech Rep. 178*, 1991, 1–47.

(64) P. Gudmundson, *J. Mech. Phys. Solids*, 2004, **52**, 1379–1406.

(65) E. Martínez-Pañeda, V. S. Deshpande, C. F. Niordson and N. A. Fleck, *J. Mech. Phys. Solids*, 2019, **126**, 136–150.

(66) C. F. Niordson and B. N. Legarth, *J. Mech. Phys. Solids*, 2010, **58**, 542–557.

(67) N. A. Fleck and J. R. Willis, *J. Mech. Phys. Solids*, 2009, **57**, 1045–1057.

(68) A. Panteghini and L. Bardella, *Comput. Methods Appl. Mech. Eng.*, 2016, **310**, 840–865.

(69) E. Demir, F. Roters and D. Raabe, *J. Mech. Phys. Solids*, 2010, **58**, 1599–1612.

(70) A. Arsenlis and D. M. Parks, *Acta Mater.*, 1999, **47**, 1597–1611.

(71) L. Nicola, E. Van der Giessen and A. Needleman, *J. Appl. Phys.*, 2003, **93**, 5920–5928.

(72) J. P.Hirth and J. Lothe, Theory of Dislocations 2nd edn (Malabar,Fl:KriegerPublishingCompany), 1992.

# Appendix A: Calculating Dislocation Density in Cu Substrate below the Cu/Gr interface

The presence of a lattice defect in the specimen causes the planes to bend close to the defect. The bending of the lattice planes causes a change in diffraction conditions and, therefore, a change in the contrast of the image. To understand why contrast is seen from dislocations, consider the specimen shown in Fig. A.1. The specimen contains an edge dislocation, and the diffracting lattice planes near the dislocations are bent. The specimen is set up such that it is slightly tilted away from the Bragg condition. Hence, the distortion due to the dislocation will then bend the near-diffracting planes back into the Bragg diffracting condition. Regions far from the dislocation are tilted well away from the Bragg condition, while the regions or either side of the dislocation core are at the Bragg condition for $\pm\mathbf{g_{hkl}}$.

Weak-beam dark-field technique, under certain diffraction conditions, allows the dislocations to be imaged as narrow lines (approximately 1.5 nm wide). The steps involved in imaging dislocations using weak beam dark field is summarized here again :

- Orient the sample with respect to electron beam while watching the diffraction pattern such that the Bragg condition is only met for one point in the reciprocal lattice or one diffraction vector $\mathbf{g_{220}}$ and no other reflections are excited.

- The weak beam image is then formed by tilting the beam using the DF beam deflecting coils such that the reflection $\mathbf{g_{220}}$ is brought to the optic axis, thus achieving the required $\mathbf{g_{220}}(\mathbf{3g_{220}})$ condition. By doing so, we make $\mathbf{s}_{\mathbf{g_{220}}}$ (excitation error: it is the distance measured in reciprocal space that determines how far the diffraction spot is from satisfying Bragg's condition) large, and if a defect is present, the diffracting planes are bent locally back into the Bragg-diffracting orientation to give more intensity in the DF image.

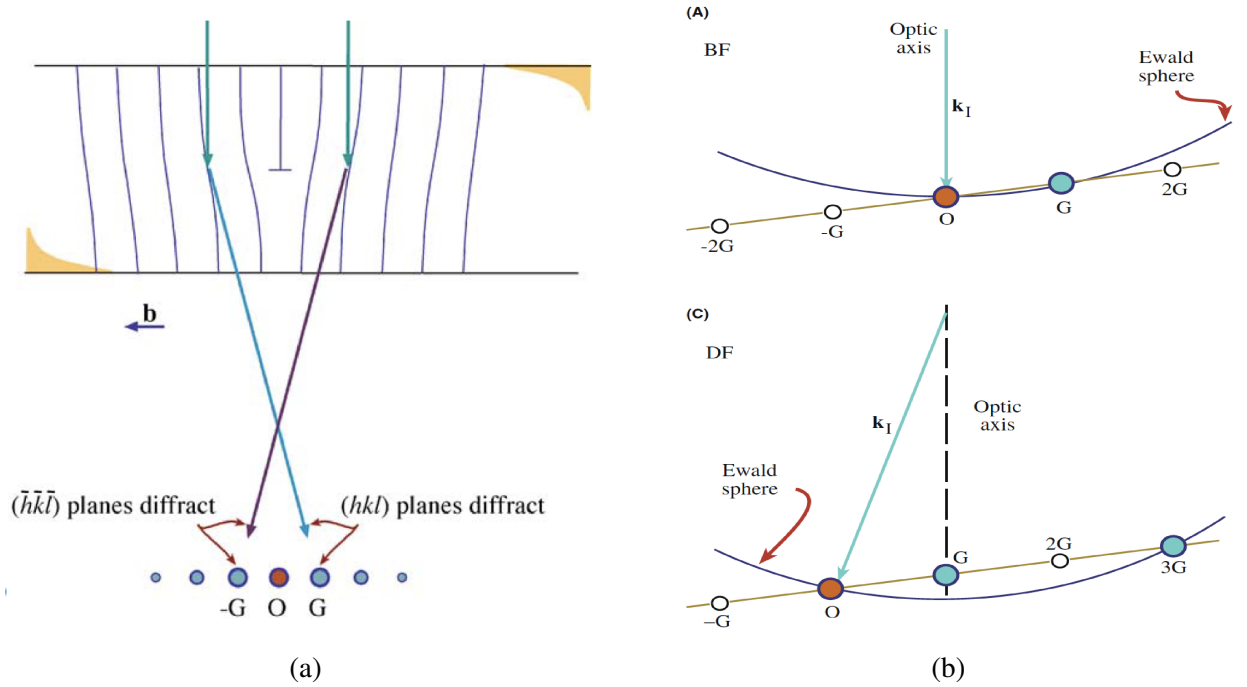


(a) (b)

Figure A.1: (a) The specimen is tilted slightly away from the Bragg condition. The distorted planes close to the edge dislocation are bent back into the Bragg-diffracting condition, diffracting into G and –G as shown (b) Schematic illustrating the WB imaging steps. Adapted from Williams, David.B. and Carter, C.Barry, Transmission Electron Microscopy: A Textbook for Materials Science, Springer.

The setup of the weak beam condition is illustrated in Fig. A.1. Hence, the dislocations will be imaged as black lines on a bright background in a BF image and as white lines on a dark background in a DF image.

Dislocation density can then be calculated using:

$$\rho = \frac{4\Lambda}{At\pi}. \tag{A.1}$$

Here, $\Lambda$ is the total projected length of dislocations imaged on area A and t is the thickness of the sample calculated using CBED. In our experiment, the area of interest $A = 2\,877\,980.529\,\text{nm}^2$ and the total projected length of dislocations are $\Gamma = 7386.916\,\text{nm}$ Dislocation density can then be calculated using:

$$\rho = \frac{4\Lambda}{At\pi}. \tag{A.2}$$

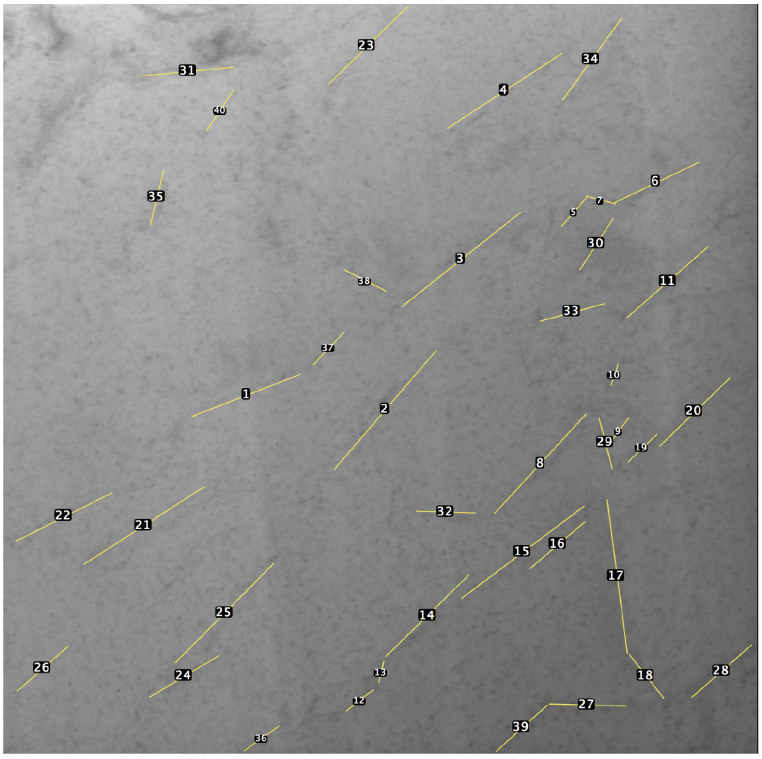


Figure A.2: Weak Beam DF TEM image of the Cu Substrate under the Cu/Gr interface.

Here, $\Lambda$ is is the total projected length of dislocations imaged on area A and t is the thickness of the sample calculated using CBED. In our experiment, the area of interest $A = 2\,877\,980.529\,\text{nm}^2$ and the total projected length of dislocations are $\Gamma = 7386.916\,\text{nm}$ (Fig. A.2).

## A.1 Thickness Calculations

The thickness of the TEM sample is calculated using the Convergent Beam Electron Diffraction (CBED) technique. The specimen is tilted to a two-beam condition such that only a direct beam and one strongly excited hkl reflection are seen in the diffraction pattern. On achieving the two-beam condition, the CBED disk contains parallel intensity oscillations as shown in Fig. A.3(a). The fringe spacing corresponds to angles $\delta\theta_i$, and from these spacings, one can obtain a deviation $s_i$ for the $i^{th}$ fringe (where i is an integer) from the equation

$$s_i = \frac{\lambda\delta\theta_i}{2\theta B d^2} \tag{A.3}$$

where $\theta B$ is the Bragg angle for the diffracting hkl plane, d is the hkl inter planar spacing. The angle $2\theta B$ in the CBED pattern is the separation of the 000 and hkl disks. $\lambda$ is the wavelength of the electron. One can determine the sample thickness by using the following equation:

$$\frac{s_i^2}{n_k^2} + \frac{1}{\xi_g^2 n_k^2} = \frac{1}{t^2}. \tag{A.4}$$

Even though we do not know $\xi_g$, we can use the graphical method explained below to calculate the thickness t:

- Arbitrarily assign the integer n=1 to the first fringe, which corresponds to an excitation error $s_i$.
- Then assign n = 2 to the second fringe, $s_2$, etc
- Plot $(s_i/n_k)^2$ versus $(1/n_k)^2$. If the result is a straight line, the arbitrary assignment was good.
- If the plot is a curve, repeat the procedure by re-assigning n = 2 to the first fringe.
- Continue to iterate until a straight line is obtained.

The $\frac{s_i^2}{n_i^2}$ is summarized in table. A.1. The intercept of $\frac{s_i^2}{n_i^2}$ vs. $\frac{1}{n_i^2}$ is $\frac{1}{t^2}$. Hence from the plot shown in

| $s_i\ (nm^{-1})$ | $n_i$ | $\frac{s_i^2}{n_i^2} \times 10^{-5} (nm^{-2})$ |
|---|---|---|
| 0.0064126 | 2 | 1.028 |
| 0.0180200 | 3 | 3.608 |
| 0.0298748 | 4 | 5.578 |

Table A.1: CBED Data for Thickness Determination.

Fig. A.3(b), the thickness of the TEM sample is 113 nm.

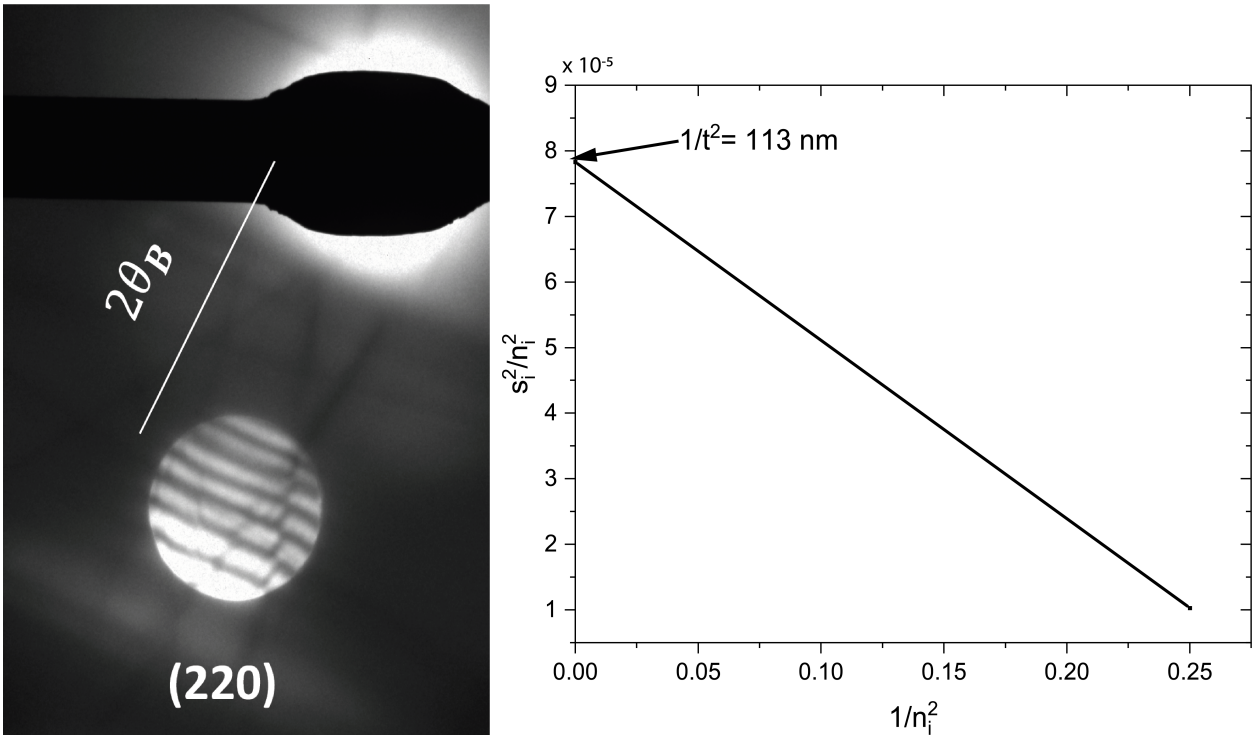


(a) (b)

Figure A.3: (a) Parallel Kossel-Mollenstedt fringes in a ZOLZ CBED pattern under two-beam conditions with (220) strongly excited, (b) Intercept of $\frac{s_i^2}{n_i^2}$ vs. $\frac{1}{n_i^2}$ gives us the thickness of the TEM sample as 113 nm.

## Appendix B: Calculating the Nanolaminate's Effective Flexural Rigidity

Composite beams are designed to increase either strength or stiffness of a structure. To check if our nanolaminate composite exhibits higher stiffness due to the presence of graphene, we calculated the flexural rigidity of Cu-Cu and Cu-Gr-Cu nanolaminates using beam theory. Flexural rigidity or bending stiffness of a beam determines the resistance of a member against bending deformation. It can be analytically calculated from the deflection of the beam and the applied force (B.1).

$$K = \frac{P}{D}. \tag{B.1}$$

Here, $P$ is the load and $D$ is the deflection of the beam.

According to beam theory, when a slender composite beam is subjected to a moment, no deformation occurs due to shear across the cross-section, i.e., a planar cross-section remains planar during bending. This means that the strain distribution across the beam cross-section is continuous and linear. However, the stress distribution becomes discontinuous when the material in the beam cross-section changes. The bending stress distribution can be determined from Eq. B.2. Here, $y$ is the distance from the neutral axis (N.A), and the $I$ is the moment of inertia about the N.A. Hence, the first step towards calculating the flexural rigidity of the nanolaminates is to determine the position of the N.A.

$$\sigma_{bending} = -\frac{My}{I}. \tag{B.2}$$

For non-composite beams, the N.A is the location where the bending stress is zero. In a composite beam, the location of the neutral axis (N.A) depends on the relative stiffness and the size of each material section. As shown in Fig. B.1, the position of the N.A is determined relative to the bottom of the beam. The distance h can be determined by recalling that the stresses through the

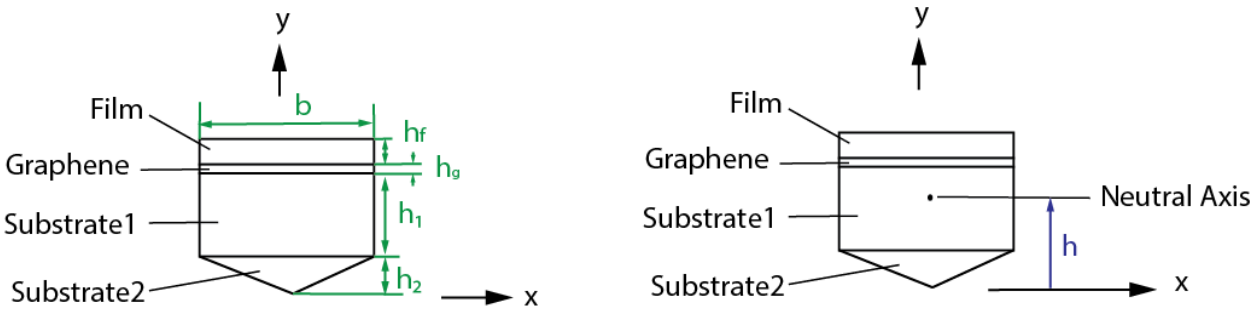


Figure B.1: Composite cross-section to calculate the N.A and the flexural rigidity of the nanolaminate composites

cross-section must be in equilibrium. On summing the forces in the x-direction we get,

$$E_f \int_{A_f} y_f dA_f + E_g \int_{A_g} y_g dA_g + E_2 \int_{A_2} y_{S_2} dA_{S_2} + E_1 \int_{A_1} y_{S_1} dA_{S_1} = 0. \tag{B.3}$$

In the above equation, $y_f$, $y_g$, $y_2$, $y_1$ are the vertical distances from the neutral axis to centroid of the film, graphene, Substrate2 and Substrate1 respectively. Writing the vertical distances in terms of dimensions shown in Fig. B.1, we get :

$$E_f(h_1+h_2+h_g+\frac{1}{2}h_f-h)bh_f+E_g(h_1+h_2+\frac{1}{2}h_g-h)bh_g+E_2(h_1+\frac{1}{2}h_2-h)bh_2+E_1(\frac{2}{3}h_1-h)\frac{1}{2}bh_1 = 0. \tag{B.4}$$

Solving for h,

$$h = \frac{E_f(h_1 + h_2 + h_g + \frac{1}{2}h_f)h_f + E_g(h_1 + h_2 + \frac{1}{2}h_g)h_g + E_2(h_1 + \frac{1}{2}h_2)h_2 + E_1(\frac{2}{3}h_1)\frac{h_1}{2}}{E_f h_f + E_g h_g + E_2 h_2 + E_1 h_1}. \tag{B.5}$$

The N.A for Cu-Cu and Cu-Gr-Cu cantilever is at 2.19 µm and 2.195 µm from the top beam surface, respectively. The composite's effective flexural rigidity can then be calculated using the equation below:

$$EI_{eff} = E_s I_s + E_f I_f + E_g I_g. \tag{B.6}$$

The subscript $s$, $f$, and $g$ correspond to Cu-substrate, Cu film, and graphene. The calcu-

lated effective flexural rigidity for Cu-Cu and Cu-Gr-Cu nanolaminates are 840.14 mNμm$^2$ and 842.29 mNμm$^2$ respectively. All the above calculations are performed assuming the thickness of graphene to be $h$ = 0.335 nm. A two-sample T-test was performed on the calculated effective EI for Cu-Cu and Cu-Gr-Cu nanolaminates. A p-value of 0.2181 was observed irrespective of the assumption of equal or unequal variance. Since the p-value is higher than the significance level of 0.05, the difference between the two calculated effective EI is not statistically significant. Thus, adding a single layer of graphene to the composite does not enhance the bending stiffness of the beam.

# Appendix C: Determining the Compliance of the Elastic Support in Cantilever Beam Bending Experiments

It is essential to estimate the flexibility added by the elastic support/bulk nanolaminate attached to the cantilever beam while analyzing the mechanical behavior of our nanolaminate composites. We ensured that the numerical analysis is closest to the experiments by modeling the Cu substrate using a user-material subroutine that incorporates single-crystal plasticity constitutive relations to account for the kinematics of finite deformation and lattice rotation associated with single-crystal plasticity [63]. Furthermore, the Berkovich tip was modeled as a rigid analytical surface shaped like a cone so that the ratio of cross-sectional area to depth is the same as the Berkovich indenter [43, 52]. The following section details the FEA model.

## C.1 3D Finite Element Modelling

Numerical simulations were performed using the commercial finite element code: ABAQUS [51]. The Berkovich tip was modeled as an analytical rigid surface shaped like a cone with a half apex angle of 70.3° and a tip radius of 50 nm so that the ratio of cross-sectional area to depth is the same as the Berkovich indenter [43, 52]. The indenter deflected the nanolaminate cantilever beam to a downward vertical displacement of 700 nm at a constant rate followed by a withdrawal of the indenter.

The numerical study of cantilever beam bending was considered adiabatic, and the material was not subjected to body force. The simplified domain in Fig C.1(a) presents a conical rigid indenter displacing the end of the nanolaminate cantilever beam. Given the symmetries of both geometry and loading conditions, the domain is divided in half along the z-axis to reduce computational time. Symmetry conditions are applied to the left surface. An elastic support was attached to

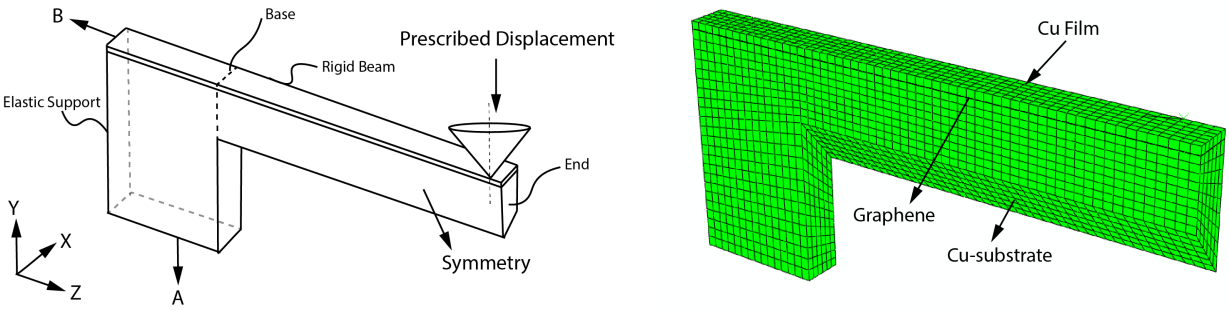


(a) (b)

Figure C.1: 3D finite element simulations of cantilever bending experiments (a) Schematic of the bending test of Cu-Gr-Cu nanolaminate, (b) overall mesh with rigid indenter.

the base of the cantilever beam to model elastic deformations. The displacement in all directions was restricted at the bottom (marked A), and end (marked B) surfaces as shown in Fig. C.1(a). The Coulomb friction law is assumed to hold between the contacting surfaces, and the friction coefficient was taken to be 1. Nonlinear kinematics were used during the loading and unloading step to accommodate large displacements during bending tests.

The Cu film and the Cu substrate are meshed using twenty-node quadratic brick elements (C3D20RH) with reduced integration and hybrid with linear pressure (Fig C.1(b)). C3D20RH elements were chosen to avoid shear locking. Graphene is modeled with four-node quadrilateral membrane elements (M3D4R) with thickness $h = 0.335$ nm. To model the interfacial interactions of graphene and copper, the nodes at the bottom of the film surface are tied to the graphene nodes, which in turn are then tied to nodes at the top substrate surface.

The single crystal Cu-substrate was modeled using a user-material subroutine that incorporates single-crystal elasticity and plasticity constitutive relations to account for the kinematics of finite deformation and lattice rotation associated with single-crystal plasticity [63]. The elastic moduli used for the Cu-substrate were $C_{11} = 169.1\,\text{GPa}$, $C_{12} = 122.2\,\text{GPa}$, and $C_{44} = 75.42\,\text{GPa}$ [72]. The Young's modulus of the Cu substrate calculated from the elastic constants is 66.7 GPa. The plastic slip systems used was $\{1\,1\,1\}\ \langle 1\,1\,0\rangle$ [72]. Since the Cu substrate was annealed during the graphene growth, hardening is not expected to be present. Consequently, the initial hardening modulus was set to zero.

| Material Property | Rigid Beam | | Elastic Support | |
|---|---|---|---|---|
| | Cu Film | Cu Substrate | Cu Film | Cu Substrate |
| Young's modulus (GPa) | 107800 | 66700 | 107.8 | 66.7 |
| Yield Stress (GPa) | 5000 | 5000 | N/A | 6000 |
| Saturation Stress (GPa) | N/A | 5000 | N/A | 6100 |
| Hardening | N/A | 0 | N/A | 0 |

Table C.1: Summary of Material Properties Used to Determine the Elastic Contribution of the Support.

To single out the elastic contributions of the support, the cantilever beam is modeled as a rigid beam. Hence, the yield stress and the saturation stress for the Cu film and Cu substrate (that are part of the cantilever beam) are assigned large numbers. The rectangular support exhibits linear elastic behavior. The details of the material properties assigned to the cantilever beam and the rectangular support are shown in Table.C.1.

The slope of the normalized displacement-load curve is the compliance of the elastic support, $C_s$.

# Appendix D: Calculating Resolved Shear Stress in Single Crystal Cu Substrate

In chapter 5, the SGP simulations model assumed isotropic plasticity. However, the Cu substrate in our nanolaminate cantilever beam is a single crystal such that the beam is oriented along the [1 0 0] direction (Fig D.1). Plasticity in a single crystal is anisotropic. Hence, additional constraints to the plastic strains were required to accurately model plastic flow in the Cu substrate. When a single crystal beam is subjected to a load, the plastic flow initially consists of shearing parallel to one member of a family crystallographic planes in the crystal, in the direction of a vector $s$ lying in that plane illustrated in the picture above. The crystallographic plane on which shear occurs is called a slip plane.

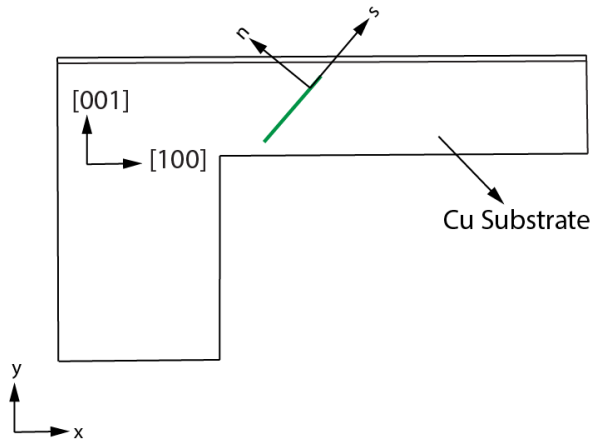


Figure D.1: Schematic representing the crystal orientation of the single crystal Cu Substrate in our nanolaminate. The green line represents the slip plane.

In an FCC crystal, 12 possible slip system exists: $\{1\,1\,1\}\ \langle 1\,1\,0\rangle$. On applying a load to a single crystal, shearing occurs on the slip system and the resolved shear stress acting on $k^{th}$ slip system

| Slip System | Slip Plane | Slip Direction |
|---|---|---|
| 1 | $(1\,1\,1)$ | $[1\,\bar{1}\,0]$ |
| 2 | $(1\,1\,1)$ | $[0\,1\,\bar{1}]$ |
| 3 | $(1\,1\,1)$ | $[\bar{1}\,0\,1]$ |
| 4 | $(1\,\bar{1}\,1)$ | $[\bar{1}\,0\,1]$ |
| 5 | $(1\,\bar{1}\,1)$ | $[0\,\bar{1}\,\bar{1}]$ |
| 6 | $(1\,\bar{1}\,1)$ | $[1\,1\,0]$ |
| 7 | $(1\,\bar{1}\,\bar{1})$ | $[1\,1\,0]$ |
| 8 | $(1\,\bar{1}\,\bar{1})$ | $[0\,\bar{1}\,1]$ |
| 9 | $(1\,\bar{1}\,\bar{1})$ | $[\bar{1}\,0\,\bar{1}]$ |
| 10 | $(1\,1\,\bar{1})$ | $[\bar{1}\,0\,\bar{1}]$ |
| 11 | $(1\,1\,\bar{1})$ | $[0\,1\,1]$ |
| 12 | $(1\,1\,\bar{1})$ | $[1\,\bar{1}\,0]$ |

Table D.1: The 12 Slip Systems Present in an FCC Crystal.

and can be computed from the Cauchy stress $\sigma_{ij}$,

$$\tau^{(k)} = \mu_{ij}^{(k)} \sigma_{ij}. \tag{D.1}$$

Here, $\tau^{(k)}$ is the resolved shear stress acting on $k^{th}$ slip system and $\mu_{ij}^{(k)}$ is Schmid orientation tensor given by:

$$\mu_{ij}^{(k)} = \frac{1}{2}(s_i^{(k)} n_j^{(k)} + s_j^{(k)} n_i^{(k)}) \tag{D.2}$$

where $n^{(k)}$ and $s^{(k)}$ are the slip plane normal and slip direction respectively. Similarly, the plastic strain acting on slip planes $k$ are give by:

$$\varepsilon_{ij}^{p} = \sum_{k=1}^{N} \mu_{ij}^{(k)} \gamma^{(k)} \tag{D.3}$$

| Slip System | Resolved Shear Stress | Plastic Slip |
|---|---|---|
| $(1\,1\,1)[1\,\bar{1}\,0]$ | $\frac{\sigma_{11}-\sigma_{22}}{\sqrt{6}}$ | $\gamma_1$ |
| $(1\,1\,1)[0\,1\,\bar{1}]$ | $\frac{\sigma_{12}+\sigma_{22}-\sigma_{33}}{\sqrt{6}}$ | $\gamma_2$ |
| $(1\,1\,1)[\bar{1}\,0\,1]$ | $-\frac{\sigma_{11}+\sigma_{12}-\sigma_{33}}{\sqrt{6}}$ | $-\gamma_3$ |
| $(1\,\bar{1}\,1)[\bar{1}\,0\,1]$ | $\frac{\sigma_{12}-\sigma_{11}+\sigma_{33}}{\sqrt{6}}$ | $\gamma_4$ |
| $(1\,\bar{1}\,1)[0\,\bar{1}\,\bar{1}]$ | $-\frac{\sigma_{12}-\sigma_{22}+\sigma_{33}}{\sqrt{6}}$ | $-\gamma_5$ |
| $(1\,\bar{1}\,1)[1\,1\,0]$ | $\frac{\sigma_{11}-\sigma_{22}}{\sqrt{6}}$ | $\gamma_6$ |
| $(1\,\bar{1}\,\bar{1})[1\,1\,0]$ | $\frac{\sigma_{11}-\sigma_{22}}{\sqrt{6}}$ | $\gamma_6$ |
| $(1\,\bar{1}\,\bar{1})[0\,\bar{1}\,1]$ | $-\frac{\sigma_{12}-\sigma_{22}+\sigma_{33}}{\sqrt{6}}$ | $-\gamma_5$ |
| $(1\,\bar{1}\,\bar{1})[\bar{1}\,0\,\bar{1}]$ | $\frac{\sigma_{12}-\sigma_{11}+\sigma_{33}}{\sqrt{6}}$ | $\gamma_4$ |
| $(1\,1\,\bar{1})[\bar{1}\,0\,\bar{1}]$ | $-\frac{\sigma_{11}+\sigma_{12}-\sigma_{33}}{\sqrt{6}}$ | $-\gamma_3$ |
| $(1\,1\,\bar{1})[0\,1\,1]$ | $\frac{\sigma_{12}+\sigma_{22}-\sigma_{33}}{\sqrt{6}}$ | $\gamma_2$ |
| $(1\,1\,\bar{1})[1\,\bar{1}\,0]$ | $\frac{\sigma_{11}-\sigma_{22}}{\sqrt{6}}$ | $\gamma_1$ |

Table D.2: The Resolved Shear Stress calculated for all 12 Slip Systems in a Single-Crystal Cu beam Oriented along $[1\,0\,0]$.

where $\gamma^{(k)}$ is the plastic slip.

Slip on the critical system initiates when the resolved shear stress exceeds the strength of the slip system. The single-crystal Cu substrate cantilever beam has the longitudinal axis oriented along the $[1\,0\,0]$ direction and the top surface corresponding to $(0\,0\,1)$ plane. Table. D.2 presents the the 12 slip systems along with the corresponding resolved shear stress and plastic slip $\gamma$. The sign of the plastic slip is the same as the sign of resolved shear stress.

The simulation model assumes plane strain plastic deformation. One can also calculate plastic strain acting on slip planes $k$ using Eqn. D.3.

$$\varepsilon_{ij}^{p} = \begin{bmatrix} \frac{\sqrt{2}}{\sqrt{3}}(\gamma_1 - \gamma_3 - \gamma_4 + \gamma_6) & \frac{\sqrt{2}}{2\sqrt{3}}(\gamma_2 - \gamma_3 + \gamma_4 - \gamma_5) & 0 \\ \frac{\sqrt{2}}{2\sqrt{3}}(\gamma_2 - \gamma_3 + \gamma_4 - \gamma_5) & -\frac{\sqrt{2}}{\sqrt{3}}(\gamma_1 - \gamma_2 - \gamma_5 + \gamma_6) & 0 \\ 0 & 0 & -\frac{\sqrt{2}}{\sqrt{3}}(\gamma_2 - \gamma_3 - \gamma_4 + \gamma_5) \end{bmatrix}. \tag{D.4}$$

$\varepsilon_{13}^{p}$ and $\varepsilon_{23}^{p}$ are already equal to zero, on setting $\varepsilon_{33}^{p} = 0$, we get:

$$\varepsilon_{33}^{p} = \gamma_2 - \gamma_3 - \gamma_4 + \gamma_5 = 0. \tag{D.5}$$

Hence, to satisfy the above equation,$\gamma_2, \gamma_3, \gamma_4, \gamma_5$ should be equal to zero. The plastic strain acting on the slip system simplifies to:

$$\varepsilon_{ij}^{p} = \begin{bmatrix} \frac{\sqrt{2}}{\sqrt{3}}(\gamma_1 + \gamma_6) & 0 & 0 \\ 0 & -\frac{\sqrt{2}}{\sqrt{3}}(\gamma_1 + \gamma_6) & 0 \\ 0 & 0 & 0 \end{bmatrix}. \tag{D.6}$$

Thus, only 4 slip systems with equal slip (i.e. $\gamma_1 = \gamma_6$) are activated: $(1\,1\,1)$ $[1\,\bar{1}\,0]$, $(1\,\bar{1}\,1)$ $[1\,1\,0]$, $(1\,\bar{1}\,\bar{1})$ $[1\,1\,0]$, $(1\,1\,\bar{1})$ $[1\,\bar{1}\,0]$. The corresponding resolved shear stress on the 4 activated slip planes is:

$$\tau^{(k)} = \frac{\sigma_{11} - \sigma_{22}}{\sqrt{6}}. \tag{D.7}$$

The slip systems act at ±45° to the bottom edge of the cantilever beam ( or $[1\,0\,0]$ direction). It is interesting to note that slip systems $(1\,1\,1)$ $[1\,\bar{1}\,0]$ and $(1\,1\,\bar{1})$ $[1\,\bar{1}\,0]$ have the same resolved shear stress and slip direction. Similarly, slip systems $(1\,\bar{1}\,1)$ $[1\,1\,0]$ and $(1\,\bar{1}\,\bar{1})$ $[1\,1\,0]$ also have the same resolved shear stress and slip direction. This introduces plane strain deformation in the cantilever beam.

# Appendix E: The Effective Rectangular Cross-section of the Cantilever Beam for SGP simulations

Strain gradient plasticity study of beam bending is a 2D analysis. The cantilever beam in the numerical study has an effective rectangular cross-section instead of the pentagonal cross-section fabricated in our experiments. The effective thickness of the beam is calculated such that the neutral axis is the same distance below graphene as in the experiments.

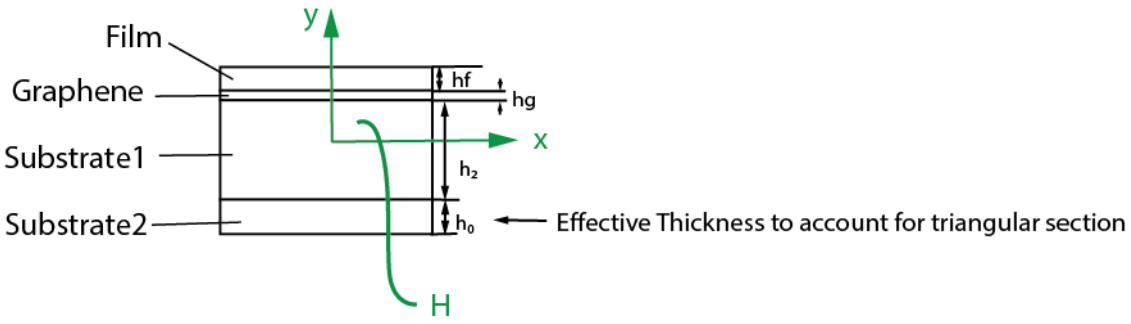


Figure E.1: Effective rectangular cross-section for 2D strain gradient plasticity simulations.

The stresses through the beam cross-section must be in equilibrium. Hence, on summing the forces in the x-direction we get,

$$E_f \int_{A_f} y_f dA_f + E_g \int_{A_g} y_g dA_g + E_2 \int_{A_2} y_{S_2} dA_{S_2} + E_1 \int_{A_1} y_{S_1} dA_{S_1} = 0. \qquad \text{(E.1)}$$

In the above equation, $y_f$, $y_g$, $y_2$, $y_1$ are the vertical distances from the neutral axis to centroid of the film, graphene, Substrate2 and Substrate1 respectively. Writing the vertical distances in terms of dimensions shown in Fig. E.1, we get :

$$E_f(H+h_g+\frac{1}{2}h_f)bh_f + E_g(H+\frac{1}{2}h_g)bh_g + E_2(H-\frac{1}{2}h_2)bh_2 + E_1(H-h_2-\frac{1}{2}h_0)\frac{1}{2}bh_0 = 0. \quad \text{(E.2)}$$

In the above equation, $h_f, h_g, h_1$ are thickness of the film, graphene and Substrate1 respectively and $H$ is the distance of the neutral axis from graphene. By substituting $E_f = 107.8\,\text{GPa}$, $E_g = 1$ TPa and $E_1 = E_2 = 66.7\,\text{GPa}$ in Eqn. E.2, we solved for $h_0$. The effective rectangular height for Substrate2 is $h_0 = 0.917\,\mu\text{m}$ while the total thickness of the rectangular cross section as $t = 3.497\,\mu\text{m}$. Hence, the N.A for Cu-Cu and Cu-Gr-Cu cantilever is at $2.19\,\mu\text{m}$ and $2.195\,\mu\text{m}$ from the top beam surface, respectively. The composite's effective flexural rigidity can then be calculated using the equation below:

$$EI_{eff} = E_s I_s + E_f I_f + E_g I_g. \tag{E.3}$$

The subscript s, f, and g correspond to Cu-substrate, Cu film, and graphene. The calculated effective flexural rigidity for Cu-Cu and Cu-Gr-Cu nanolaminates are $798.62\,\text{mN}\mu\text{m}^2$ and $800.6\,\text{mN}\mu\text{m}^2$ respectively. All the above calculations are performed assuming the thickness of graphene to be $h = 0.335$ nm.